Study of redshifted HI from the Epoch of Reionization era

A Thesis submitted to

Jawaharlal Nehru University, New Delhi

for the Degree of

Doctor of Philosophy

by

Sourabh Paul

Raman Research Institute, Bangalore, India

2016

Declaration

I hereby declare that the work reported in this thesis entitled "**Study of redshifted HI from the Epoch of Reionization era**" has been independently carried out by me at the Raman Research Institute, Bangalore, under the supervision of Prof. Shiv K. Sethi. The subject matter presented in this thesis has not previously formed the basis of the award of any degree, diploma, associateship, fellowship or any other similar title.

Prof. Shiv K. Sethi	Sourabh Paul
(Thesis Supervisor)	(Candidate)

Dept. of Astronomy & Astrophysics,
Raman Research Institute,
C. V. Raman Avenue,
Bangalore 560080, India.

Certificate

This is to certify that the thesis entitled "**Study of redshifted HI from the Epoch of Reionization era**", submitted by **Sourabh Paul** for the award of the degree of Doctor of Philosophy of Jawaharlal Nehru University, is his original work. This has not been published or submitted to any other University for any other degree or diploma.

Prof. Ravi Subrahmanyan	Prof. Shiv K. Sethi
(Director)	(Thesis Supervisor)

Dept. of Astronomy & Astrophysics,
Raman Research Institute,
C. V. Raman Avenue,
Bangalore 560080, India.

Acknowledgements

Firstly I would like to express my sincere gratitude to my supervisor Prof. Shiv K. Sethi for the continuous support of my Ph.D study and related research, for his patience, motivation, and immense knowledge. I am also equally grateful to Prof. Dwarakanath K. S., Prof. Udayashankar N. and Prof. Ravi Subrahmanyan. They have always spent substantial time whenever I've needed them for any academic discussions. I'm thankful for their inspirations and ideas to make my PhD experience productive and stimulating.

I would also like to thank all the respected faculty members at Raman Research Institute for all the fruitful discussions and critical comments in various occasions throughout my PhD career. A special mention goes to all the scientists who taught us in the first year course work of the PhD program. My sincere thanks also goes to all collaboration members of the MWA community.

Similar profound gratitude goes to all the administrative staffs of RRI. Special thanks to Vidya at RRI Astro-floor for helping me out in anything and everything regarding any administrative issues. I'm also hugely appreciative for all the discussions and comments I have received from all my fellow PhD students and post-docs at RRI astrophysics group.

Finally, but by no means least, thanks go to my mother, father, mom-in-law, dad-in-law for their immense support. Special credit goes to my wife and fellow researcher Arpita Roy, and my sister Swagata Paul, who have supported me in every occasion throughout my PhD days.

Thesis Synopsis

The dark age of the universe ends with the formation of the first generation of galaxies. Ultraviolet radiation from these galaxies starts ionizing surrounding regions and eventually the ionized bubbles grow up in size and merge together until the hydrogen becomes fully ionized. This epoch marks a major phase transition of the universe and is known as 'Epoch of Reionization' ($z = 6 \sim 11$). EoR signal being extremely weak (30 mK), detection through direct imaging is extremely difficult with present radio telescopes. The only way of detection is through statistical analysis which requires a stable instrument and large amount of data to reduce thermal noise, measure and subtract the foreground effects. The Murchison Widefield Array (MWA) is a low frequency radio telescope operating between $80 \sim 300$ MHZ located in Western Australia. One of the key science project of this array is to detect fluctuations in the brightness temperature of the diffuse redshifted 21 cm line of neutral hydrogen from the epoch of reionization (EoR). In this thesis work we explore various modes of observations with MWA theoretically to maximize the signal to noise ratio.

We have successfully developed a unique methodology to extract power spectra from radio interferometric tracking data. It has been suggested that the foregrounds can be isolated from the HI signal, yielding clean regions dominated by the HI signal. In this work, we propose a method to extract HI power spectra based on delay spectrum approach. This method is based on modeling the HI signal taking into account the impact of the 'w term' and the change in intensity pattern during a tracking run. The information of the decorrelation of the HI signal due to 'w term' variation is used as weights to cross-correlate the measured visibilities. Our method is applicable to radio interferometers with redundant baselines (e.g. PAPER) and non-redundant baselines (e.g MWA). We demonstrate our method by

analysing 3 hours of MWA tracking data on the EoR1 field. We present both 2-dimensional and 1-dimensional (k) power spectra from the analysis and compare them with noise and point source simulation. The foreground free region (EoR window) is comparable to the expected thermal noise.

Detection of the EoR in the redshifted 21 cm line is a challenging task. Here, we formulate the detection of the EoR signal using the drift scan strategy. In drift scan mode the pointing center is fixed at zenith and we observe a time dependent patch of sky.This method potentially has better instrumental stability compared to the case where a single patch of sky is tracked. In this work, we describe a methodology based on drift scans which exploits the correlation between visibilities measured at different times to estimate the EoR signal. In particular, our aim is to infer the efficacy of such a method for a wide field-of-view instrument such as MWA. We demonstrate that the correlation time between measured visibilities could extend up to 1 hr for an interferometer array such as the MWA, which has a wide primary beam. We estimate the EoR power based on a cross-correlation of visibilities over time and show that the drift scan strategy is capable of detecting the EoR signal with a signal to noise that is comparable/ better compared to the tracking case.We also estimate the visibility correlation for a set of bright point sources and argue that the statistical inhomogeneity of bright point sources might allow their separation from the EoR signal.

Contents

List of Figures

Chapter 1

Introduction

Over the past few decades the study of Cosmology has advanced to a great extent. As a whole Cosmology is a particular wing of physics and astrophysics, that study the large scale properties of the universe. In particular this endeavour is a combination of theoretical predictions and astronomical observations to study the origin, evolution and ultimate destiny of the universe. Our understanding of the modern Cosmology has progressed with a series of major breakthroughs in observational Cosmology in the past three decades.

The near-blackbody nature of the Cosmic Microwave Background (CMB) radiation by COBE-FIRAS put the Big Bang model on firm footing (Mather et al. (1990); Fixsen et al. (1996)). The subsequent detection of CMB temperature anisotropy (Smoot (1992)) by COBE-DMR and polarization anisotropy by WMAP (Spergel et al. (2007)) and Planck (Lamarre et al. (2003)) satellites furnished proof of initial fluctuations in the early Universe which resulted in the formation of complex structures in present day Universe. This paradigm has got further support and validation by the study of Galaxy clustering carried out by many galaxy surveys (e.g. APM survey, Dalton et al. (1997) and SDSS survey, York et al. (2000)). The discovery of accelerating Universe using Type Ia supernovae (Perlmutter et al. (1999); Riess et al. (1998)) provided yet another another milestone in observational cosmology.

The CMBR polarization anisotropy measurements suggest that Universe has made a transition from being full neutral to ionized state at $z \simeq 10$. The most sought after exploration in modern Cosmology and yet to be discovered is the detection of redshifted HI

from the 'Epoch of Reionization' when the transition from neutral to ionized Universe was taking place. This has been a major science goal for many low frequency radio interferometers worldwide from last decade as this is expected to provide answers of many unsolved mysteries on the evolution of Universe.

1.1 The Epoch of Reionization

In Big Bang cosmology, the Epoch of Reionization (EoR) refers to a major phase change from dark age to present day universe. Approximately until 380 thousand years after the Big Bang, the universe was made up of tightly coupled plasma consisting of ionized gas. After the Big Bang the universe expanded at a rapid rate and cooled to a point when the atomic hydrogen formation rate (by recombination of electrons and protons) was higher than the reionization rate. This marks the first major phase change of the universe: Epoch of Recombination which occurred at redshift $z \sim 1000$. Also at this stage the universe was not dense enough to hold the photons coupled to the matter. The decoupled photons at that stage is called the relic thermal radiation: Cosmic Microwave Background.

After decoupling of photons from matter universe entered into an age of darkness as there were no conventional light sources (e.g. stars, galaxies, etc) other than gradually diminishing CMB. Electrons and protons combined to form neutral Hydrogen which was the most abundant material and the universe became transparent throughout most of the spectrum. The second phase change of the universe began when first sources of light were born roughly at redshift $z \sim 30$. These were results of tiny fluctuation seeded in the matter density field during inflationary period. The formation of first objects were primarily due to gravitational instability, although other processes like gas physics, cooling, heating, radiation processes and feedback effects started affecting the formation of first galaxies (Peebles (1993); Mo et al. (2010)). These were primarily galaxies made of zero metallicity Population III stars, second generation Population II stars and black hole driven sources (Bromm et al. (2002); Bromm & Larson (2004)). The photons emitted from these sources started ionizing the surrounding neutral hydrogen in the intergalactic medium. The rate of ionization increased as more number of sources were born in the universe. As a result ionized bubbles started to

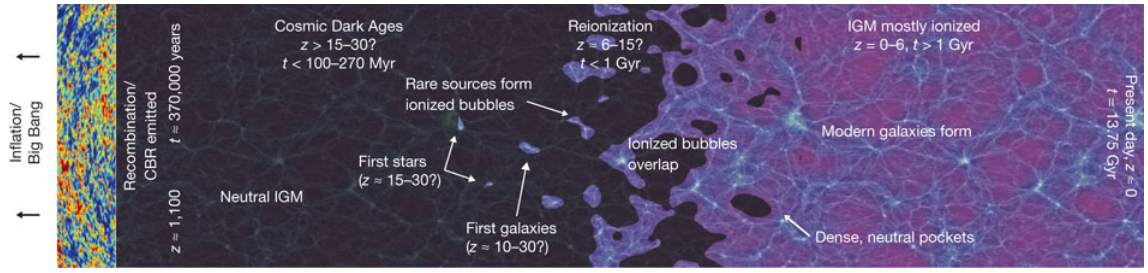

Figure 1.1: A schematic of the evolution of the Universe with time (credit: Robertson et al. (2010))

grow in size surrounding each of these sources, and with time they merged with each other making the universe ionized again except few dense neutral hydrogen clouds (Barkana & Loeb (2001); Bromm & Larson (2004); Ciardi & Ferrara (2005); Sethi (2005); Choudhury & Ferrara (2006); Furlanetto et al. (2006); Morales & Wyithe (2010)). Present observational constraints suggest the redshift range $6 \lesssim z \lesssim 12$ to be the reionization epoch. A schematic of evolution of the Universe with time is shown in Fig. 1.1.

The most crucial observational evidence of the occurrence of EoR comes from the quasar spectra at high redshifts and optical depth measurements from CMB temperature and polarization anisotropy maps. In next two sections we discuss them in detail.

1.2 Quasars and Gunn-Peterson trough

Quasars are one of the most brightest astronomical objects. Powered by accretion of material into supermassive black holes in the nuclei of distant galaxies, these objects release an enormous amount of energy (typical luminosity $\sim 10^{40}$ watt). Most of the quasars were formed at an early stage of the universe, hence some of them can be detected during the reionization epoch. Thus the quasar spectra can be studied as an useful tool to study the Intergalactic medium (IGM) during EoR.

For a neutral hydrogen atom, the Lyman alpha line corresponds to an electron transition between the ground state ($n = 1$) and first excited state ($n = 2$). Now consider a bright quasar along the line of sight and if there are a number of neutral hydrogen clouds between the quasar and observer, the clouds can absorb photons of wavelength corresponding to the

Lyman alpha line (122nm). As the absorbing clouds have smaller redshifts compared to the quasar, the signatures of these absorptions would be reflected in shorter wavelength side of the quasar's Lyman alpha emission line (Fig. 1.2). This feature is also called 'Lyman alpha forest'.

If the IGM is full of neutral hydrogen, the spectra from a quasar will have a special feature called Gunn-Peterson trough (Gunn & Peterson (1965)). The trough (presence of continuous absorption lines) is a result of the suppression of the electromagnetic emission in the quasar spectra at wavelengths shorter than the quasar's Lyman alpha emission line. Although predicted by Gunn and Peterson in 1965, it was first discovered in 2001 (Becker et al. (2001)) with the discovery of a quasar at $z = 6.28$ using the Sloan Digital Sky Survey (SDSS) data. Further discoveries of other quasars (Fan et al. (2006)) at $z > 6$ also depicts this feature (Fig. 1.3). The Gunn Peterson optical depth can be calculated as:

$$\tau_{\rm GP} = 6.6 \times 10^3 h^{-1} \left(\frac{\Omega_{\rm b} h^2}{0.019}\right) \frac{n_{\rm HI}}{\bar{n}_{\rm H}} (1+z)^{3/2} \tag{1.1}$$

where $\frac{n_{\rm HI}}{\bar{n}_{\rm H}}$ is the neutral hydrogen fraction, $\Omega_{\rm b}$ is the baryon density in units of the critical density in standard cosmology. A small amount of neutral HI result in large optical depth $\tau_{\rm GP}$. This provides the possibility to probe both spatial and temporal variation of reionization at high z.

The presence of this trough for quasars at $z > 6$ and the absence of it (although Lyman alpha forest can be present) for quasars at $z < 6$ implies that the universe was somewhat more neutral in these redshifts ($z > 6$). The corresponding increase in optical depth provides strong evidence of reionization and implies that the universe was approaching the end of neutral era at $z \sim 6$.

1.3 CMB Temperature and Polarization anisotropy

As mentioned above CMB provides an useful tool to probe EoR. The anisotropy of the microwave background present at different angular scales can be used to study the reionization. In presence of free electrons, photons experience scattering which is also known as the Thompson scattering. However as the Universe expands, the density of free electrons reduces and the rate of scattering would decrease. During the period of reionization and

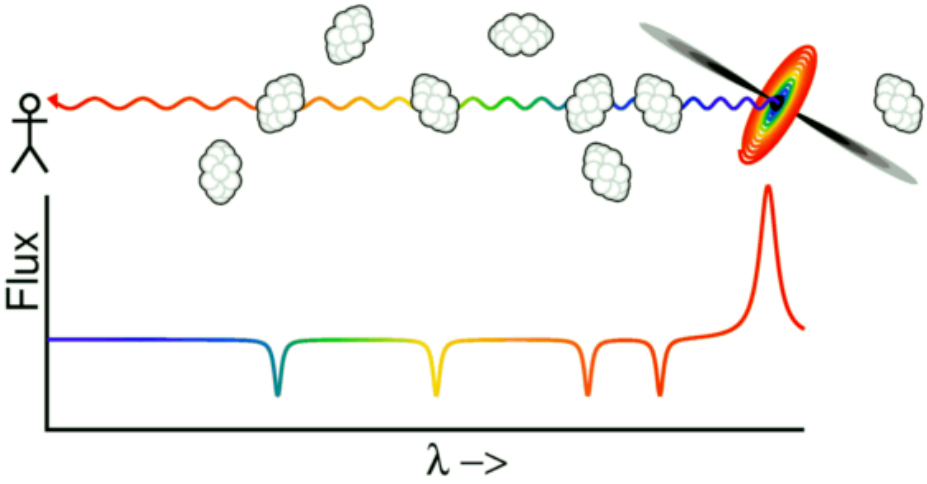

(a)

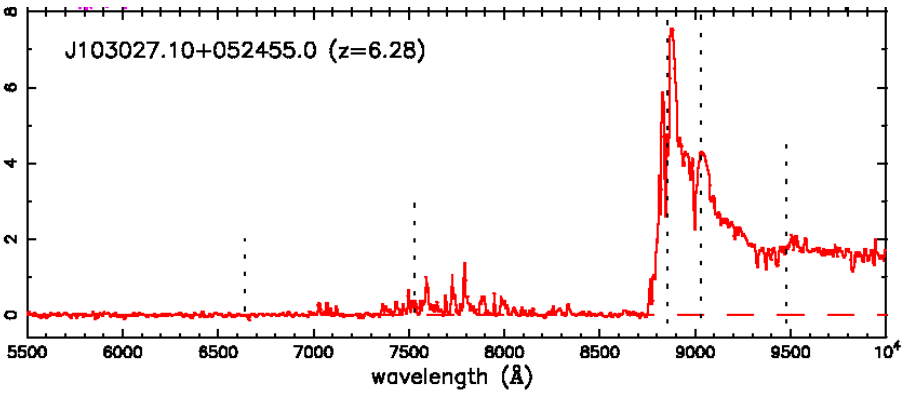

(b)

Figure 1.2: (a) Schematic of 'Lyman alpha forest' (credit: http://www.astro.ucla.edu/ wright/Lyman-alpha-forest.html); (b) Spectra of a quasar at $z = 6.28$ (Becker et al. (2001)).

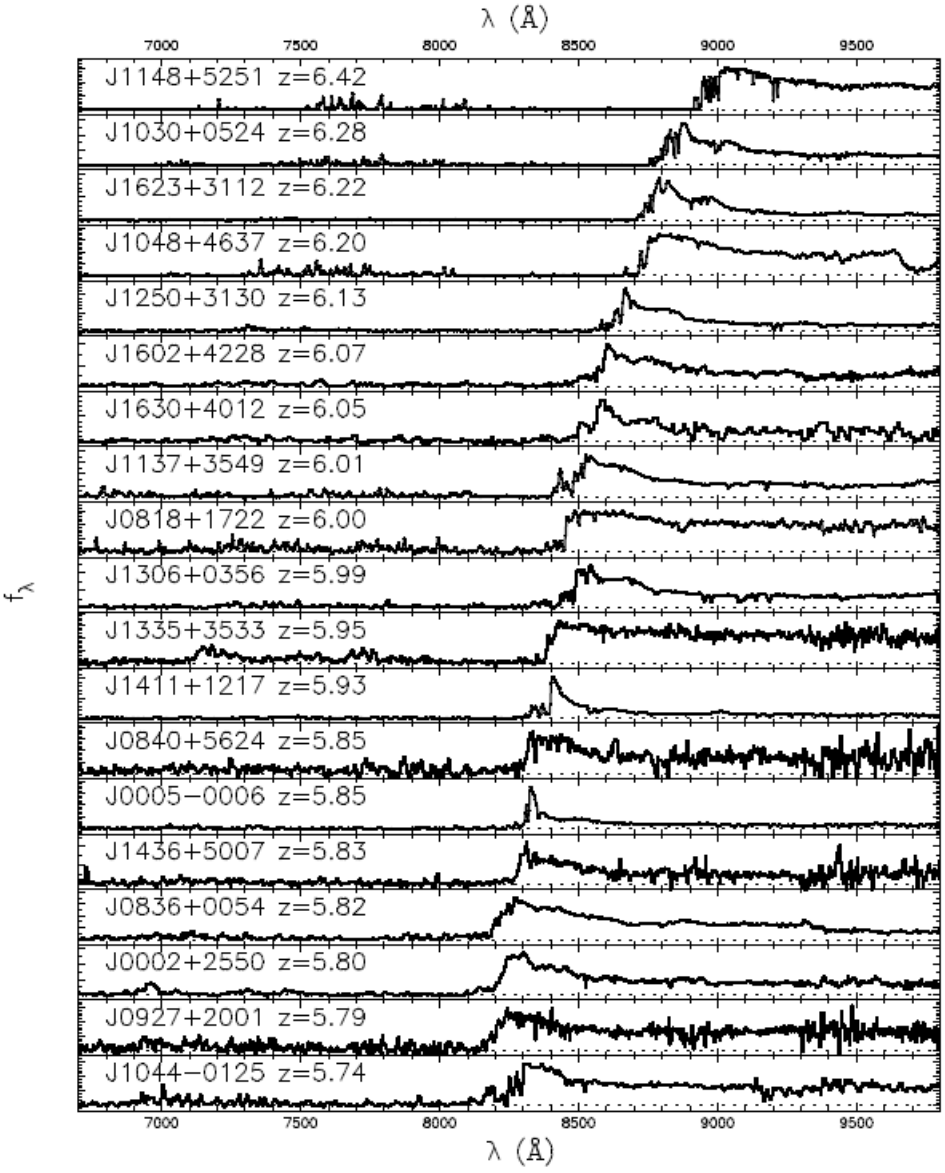

Figure 1.3: Spectra of high redshift SDSS quasars (Fan et al. (2006)). The Gunn Peterson trough is prominent in quasars at $z > 6$.

after its occurrence, free electrons would be produced in the process. Assuming the Universe did not expand significantly to sufficiently lower the free electron density, the photons would undergo Thompson scattering during this epoch. The signature of this scattering would be imprinted on the CMB anisotropy map as secondary anisotropies (anisotropy introduced after recombination). As a result of scattering, the anisotropies at smaller scales are obliterated. By observing the CMB anisotropies and comparing with the case if the reonization had not taken place, information on electron density during reionization can be obtained. With this significant knowledge on the reionization epoch can be achieved. More detailed review on this topic can be found in Peebles & Yu (1970); Bond & Efstathiou (1984); Hu & White (1997).

In absence of reionization, the properties of CMB would be very much different in terms of optical depth. Although Thompson scattering of the CMB photons with the free electrons contaminates the primary anisotropies, the resulting change in optical depth deliver important information on reionization. Similarly the CMB polarization signal would be negligible at large angular scales if the universe had remained neutral. The presence of free electrons during reionization and resulting scattering with CMB enhances the polarization signal significantly (Zaldarriaga & Seljak (1997); Haiman & Knox (1999)). There exists a subtle difference between the Gunn-Peterson and CMB anisotropy probes; the former is sensitive to the end phase of reionization whereas the latter is to the initial phase when the free electrons start to appear.

To estimate the effect of reionization on CMB photons, a function has been defined in literature called visibility function (Zaroubi (2013)):

$$g(\eta) = -\frac{d\tau}{d\eta} e^{-\tau(\eta)} \tag{1.2}$$

where τ is optical depth and η is the conformal time. This function is a measure of probability density that a CMB photon has been Thompson scattered due to free electrons originated from reionization along the line of sight between η and $\eta + d\eta$. Fig. 1.4 shows the variation of visibility function with redshift for both presence and absence of reionization. In presence of reionization, excess free electron density increase the value of visibility function compared to the case of absence of reionization.

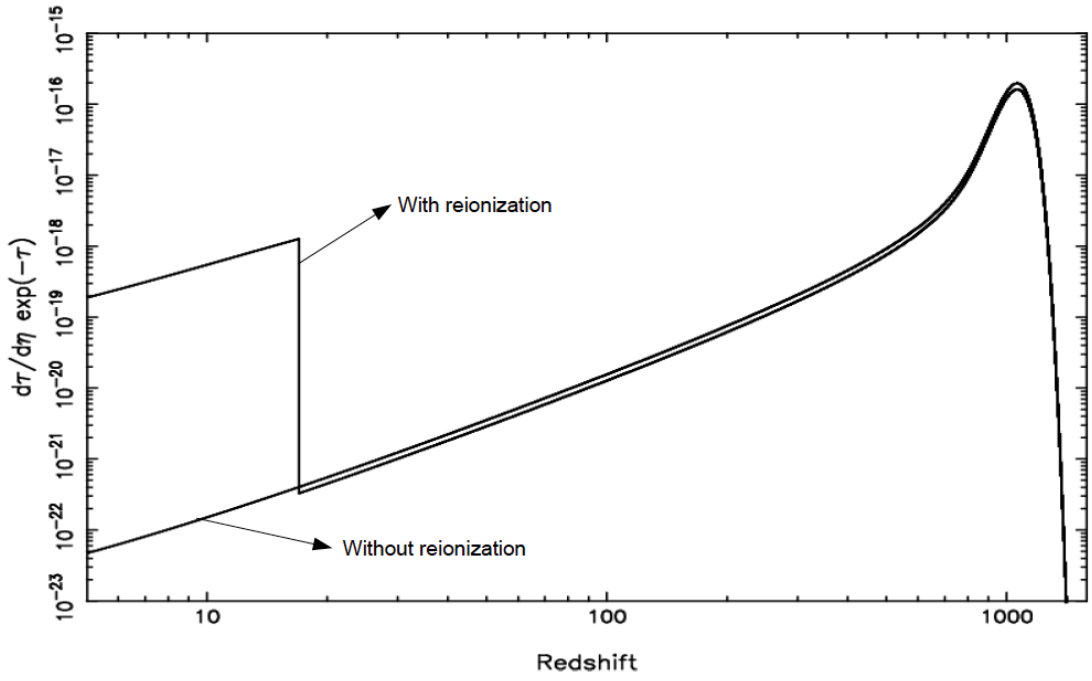

Figure 1.4: Variation of visibility function for presence and absence of reionization. Reionization produces free electrons which cause Thompson scattering of CMB photons which in turn increase the value of visibility function at reionization epoch. This plot has been simulated assuming the reionization epoch to be $z \approx 17$.

As discussed before, reionization enhances the polarization signal to a great extent. The polarization of CMB originates due to the initial fluctuation in early universe through gravitational instability. This polarization signal should drop at large angular scales in absence of reionization. However excess power is seen from WMAP observations (Page et al. (2007)) of polarization power and cross power spectra at low l in Fig. 1.5, which provides strong evidence of reionization.

1.4 21cm Cosmology

The neutral hydrogen being the most abundant and ubiquitous material, the famous 21 cm line (rest frame frequency 1420 MHz) becomes the obvious tracer to study the various properties of the gas. This line arises due to the hyperfine splitting of the hydrogen ground state due to the magnetic interaction between quantized electron & proton spins. The excited (triplet) state correspond to the parallel spins, whereas spins are anti-parallel in the ground (singlet) state. The probability of this transition is extremely low, the value of Einstein A coefficient being $A_{10} = 2.85 \times 10^{-15} s^{-1}$ which corresponds to a lifetime of the triplet state as 1.1×10^7 years for spontaneous emission. Despite such a low transition probability, this line is the most important tracer due to vast amount of neutral hydrogen during reionization epoch (Barkana & Loeb (2001); Sethi (2005); Choudhury & Ferrara (2006); Furlanetto et al. (2006); Morales & Wyithe (2010); Zaroubi (2013)). Due to expansion of the universe, the wavelength of this line gets elongated by a factor $(1 + z)$ in observer's frame.

The intensity of the 21 cm line depend on the radiative transfer through a medium along the line of sight. The radiative transfer equation for the specific intensity I_ν (Rybicki & Lightman (1986)) is expressed as:

$$\frac{dI_\nu}{d\tau_\nu} = -I_\nu + B_\nu(\tau) \tag{1.3}$$

where τ is the optical depth for absorption by gas along the line of sight, and B_ν is the Planck function.

In radio astronomy, the specific intensity I_ν can be approximated as the brightness temperature $T_b(\nu)$ owing to the Rayleigh-Jeans formula: $I_\nu = 2k_B T_b(\nu)\nu^2/c^2$, where c is the

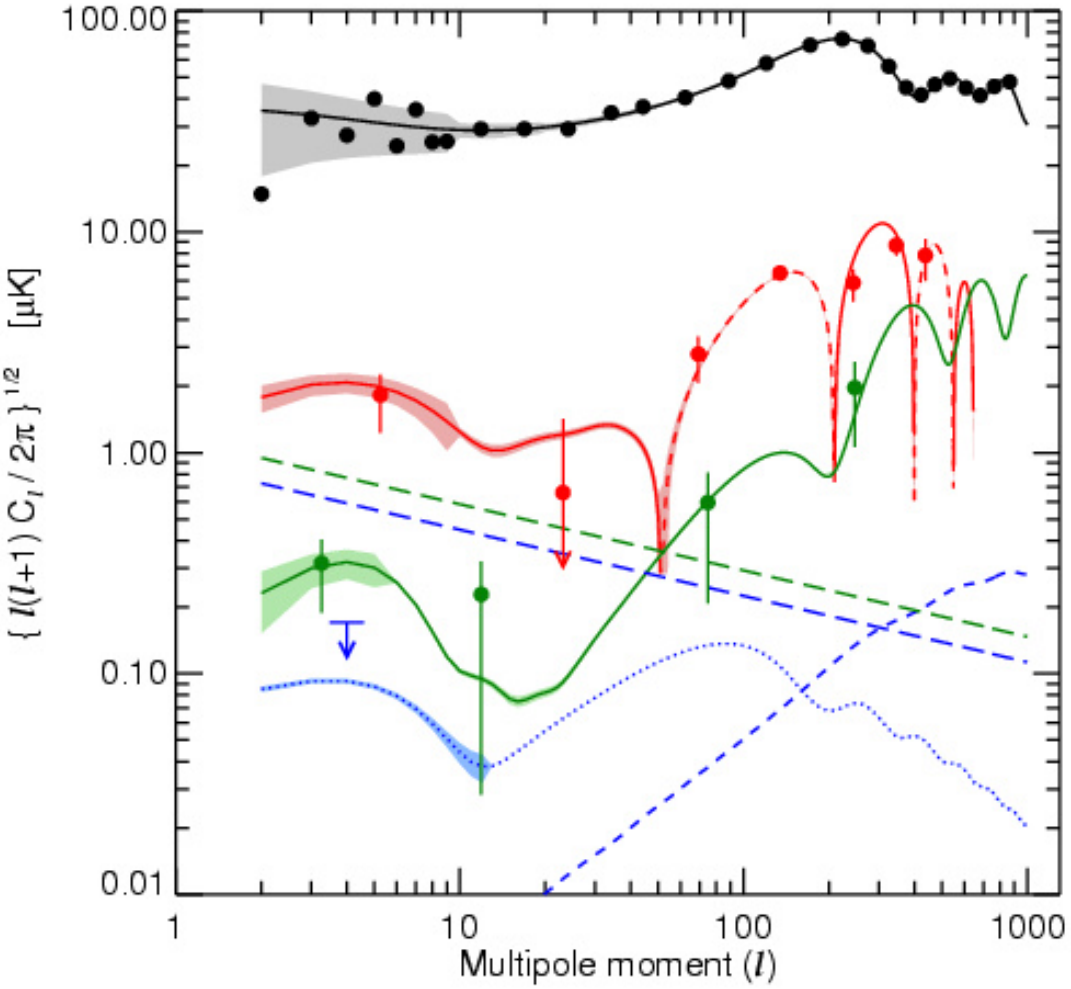

Figure 1.5: WMAP results (Page et al. (2007)) of temperature and E-mode polarization power and cross power spectra; TT (black), TE (red), and EE (green) for the best model case. Dashed line for TE shows anticorrelation regions. The presence of surplus power at low l in TE and EE power spectra provides proof of reionization.

speed of light and k_B is the universal Boltzmann constant. Substituting this in Eq. (1.3), the radiative transfer equation takes a simpler form:

$$\frac{dT_b}{d\tau_\nu} = -T_b + T_{\rm CMB} \tag{1.4}$$

Here $T_{\rm CMB}$ is the background CMB temperature, which is equivalent to the background brightness temperature in the context of 21 cm Cosmology. Solution of the Eq. (1.4) denote the observed temperature at frequency ν:

$$T_b(\nu) = T_{\rm spin}(1 - e^{-\tau_\nu}) + T_{\rm CMB}(\nu)e^{-\tau_\nu} \tag{1.5}$$

Here $T_{\rm spin}$ is the excitation temperature of the 21 cm line defined by:

$$\frac{n_1}{n_0} = \frac{g_1}{g_0}\exp(-\frac{T_*}{T_{\rm spin}}) \tag{1.6}$$

where n_1 and n_0 are the number densities of the hyperfine excited and ground state respectively; $(g_1/g_0) = 3$, which is the statistical degeneracy ratio of the two energy states and $T_* = 0.068K$.

In Eq. (1.5) the first term on the RHS gives the emission probability of 21 cm photons from the intermediate clouds, whereas the second term describes the transmission probability of the background CMB radiation. Hence, the spin temperature $T_{\rm spin}$ & the optical depth τ_ν are the two most important quantities which decide the brightness temperature in Eq. (1.5). The optical depth, which is associated with the hydrogen cloud along the line of sight, can be written as:

$$\tau_\nu = \int ds \left[1 - \exp\left(-\frac{E_{10}}{k_B T_{\rm spin}}\right)\right] \sigma_\nu n_0 \tag{1.7}$$

Here ds is a line element along the cloud; $n_0 = N_{\rm HI}/4$ with $N_{\rm HI}$ being the hydrogen density; $\sigma_\nu = \sigma_0\phi_\nu$ represents the 21cm line absorption cross-section with ϕ_ν being the line profile which is normalized such that, $\int \phi(\nu)d\nu = 1$. ϕ_ν is a resultant effect of many physical processes: natural, thermal, turbulent & velocity broadening. In our scale of interest, velocity broadening due to the Hubble expansion plays the dominant role. Substituting all the relevant terms using cosmological variables, the solution of Eq. (1.7) takes the following form:

$$\tau_\nu \approx 0.0092(1+\delta)(1+z)^{3/2}\frac{X_{\rm HI}}{T_{\rm spin}}\left[\frac{H(z)/(1+z)}{dv_\parallel/dr_\parallel}\right] \tag{1.8}$$

In above expression, $(1+\delta)$ represents the fractional overdensity of baryons; $dv_{\parallel}/dr_{\parallel}$ consists of both Hubble expansion & peculiar velocity (Kaiser (1987)), and denote the gradient of proper velocity along the line of sight; z denote the redshift and H(z) as the corresponding Hubble parameter.

The other quantity of interest is the spin temperature T_{spin} which is primarily determined by three physical processes: (i) absorption or emission of 21 cm photons with respect to the CMB; (ii) collisions with other hydrogen atoms, electrons and protons; (iii) Lyα resonant scattering which can cause a spin flip transition via an intermediate level (also known as the Wouthuysen - Field effect). Together with all these effects, the spin temperature can be expressed as (Wouthuysen (1952); Field (1958, 1959)):

$$T_{\rm spin}^{-1} = \frac{T_{\rm CMB}^{-1} + x_c T_K^{-1} + x_\alpha T_c^{-1}}{1 + x_c + x_\alpha} \tag{1.9}$$

where x_c and x_α are the coupling coefficients for collisions and Lyα scattering respectively; T_K is the gas kinetic temperature (Furlanetto et al. (2006)).

It is important to note from Eq. (1.5) that if $T_{\rm spin} = T_{\rm CMB}$, the observed brightness temperature is simply the CMB temperature $T_{\rm CMB}$. Hence any useful information of the Intergalactic medium (IGM) can be obtained through the observed brightness temperature only if $T_{\rm spin} \neq T_{\rm CMB}$. Thus, the quantity of interest is the differential brightness temperature $\delta T_b = T_b - T_{\rm CMB}$, which is rich in information concerning the IGM. This quantity can be written as (Field (1958, 1959); Madau et al. (1997); Ciardi & Madau (2003)):

$$\delta T_b = 28{\rm mK}(1+\delta) x_{HI} \left(1 - \frac{T_{CMB}}{T_{spin}}\right) \left(\frac{\Omega_b h^2}{0.0223}\right) \sqrt{\left(\frac{1+z}{10}\right)\left(\frac{0.24}{\Omega_m}\right)} \left[\frac{H(z)/(1+z)}{dv_{\parallel}/dr_{\parallel}}\right] \tag{1.10}$$

where H is the Hubble constant in units of 100 kms^{-1}Mpc^{-1}; δ denotes the density contrast; $x_{\rm HI}$ represents the neutral hydrogen fraction; and Ω_m, Ω_b are the mass, baryon densities in units of the critical density in standard cosmology.

The above equation describes a complex interplay of various astrophysical phenomenas and cosmological effects. Depending on the epochs, the contributions of the physical processes vary and affect differently on the brightness temperature. For instance, at high redshift when the universe is mostly neutral, $x_{\rm HI} \equiv 1$, δT_b follows the density fluctuation, and

hence a perfect probe of Cosmology. However, at lower redshifts when astrophysical sources dominate and the universe is significantly ionized, δT_b depends on the distinct distributions of neutral and ionized regions (Thomas et al. (2009)).

1.4.1 Global 21cm signature

As discussed above, the differential brightness temperature is dependent on a number of parameters, and its detectability varies on the epochs being studied. This variation is imprinted on the global 21cm signature (Fig. 1.6), which is defined to be the mean signal averaged over the entire sky as a function of frequency.

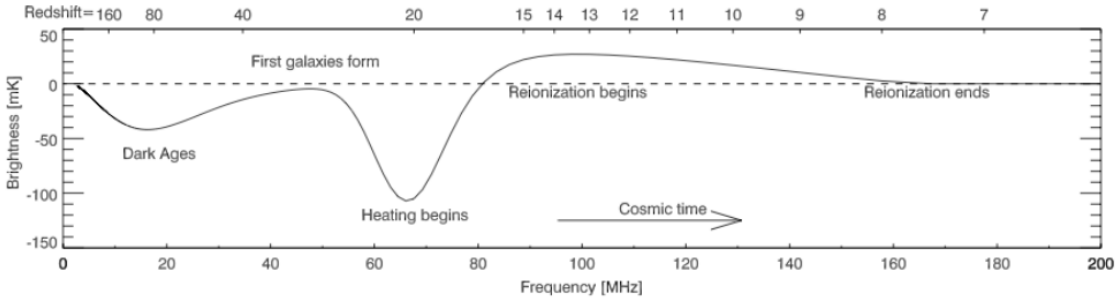

Figure 1.6: Evolution of global 21cm signal (Pritchard & Loeb (2010); Liu et al. (2013))

Next the various phases of the universe and their possible impact on the global signal is elaborated. After decoupling of CMB, the gas maintains a thermal equilibrium with the residual free electrons through Compton scattering, resulting in $T_K = T_{\rm CMB}$. Furthermore, high density of gas causes collisional coupling and effectively sets $T_{\rm spin} = T_{\rm CMB}$. This results in $\delta T_b = 0$ and no effective detectable 21cm signal. At redshift $z \leq 200$, the gas temperature drops down adiabatically as $T_K \propto (1+z)^2$. The collisional coupling further results in $T_{\rm spin} < T_{\rm CMB}$ which makes the δT_b to be nonzero for the first time, and an early absorption signal. With further expansion, the collisional coupling gets ineffective with decreasing gas density, and radiative coupling causes $T_{\rm spin} = T_{\rm CMB}$ for $z \leq 40$. This results in no detectable HI signal till first astrophysical sources are born in the universe. At a later stage, the first sources starts to form due to gravitational instability, which emit both Lyα and X-ray photons. Initially, the heating is significantly less and the spin temperature is coupled to the cold gas temperature: $T_{\rm spin} \equiv T_K < T_{\rm CMB}$, which causes an absorption signal. With

more sources coming up and increasing star formation, the Lyα coupling becomes saturated. Gradually, the heating due to X-ray becomes significantly large, thus the gas temperature makes a transition from being $T_K < T_{\rm CMB}$ to $T_K > T_{\rm CMB}$. This results the observed signal being seen in emission from absorption (Pritchard & Loeb (2010); Sethi (2005); Santos et al. (2008); Zaroubi (2013)). Once the universe is fully ionized, no 21 cm signal is seen except few isolated hydrogen clouds (damped Lyα systems).

Many ground based experiments are underway to detect this mean signal, which includes Cosmological Reionization Experiment (CoRE, Chippendale et al. (2005)), the Experiment to Detect the Global Epoch of Reionization Signal (EDGES, Bowman et al. (2008)), the SCI-HI experiment (Tabitha et al. (2014)), the Large Aperture Experiment to Detect the Dark Ages (LEDA, Greenhill & Bernardi (2012)), SARAS (Patra et al. (2015)). Although the single dish measurements can reach the required sensitivity; the ionospheric interference from our atmosphere, and the strong synchrotron emission from our galaxy makes these attempts extremely difficult.

1.4.2 21cm fluctuations and Power spectrum

The global 21cm signal contains many detailed information on the mean evolution of the universe. One must also note that each component in Eq. (1.10) also can fluctuate. The resulting fluctuation in the 21 cm signal from its mean can be denoted as $\delta_{\rm HI}$. Like the global signal, this fluctuation also contain various information on the IGM. In linear order, this fluctuation can be expanded as:

$$\delta_{\rm HI}(\mathbf{x}) = \beta_b\delta_b + \beta_x\delta_x + \beta_\alpha\delta_\alpha + \beta_T\delta_T - \delta_{\partial v} \tag{1.11}$$

Each quantity in the above equation corresponds to the fractional variation of a particular physical quantity: δ_b refers to fluctuation in baryonic density, δ_α for the Lyα coupling coefficient x_α, δ_x for the neutral fraction, δ_T for T_K, and $\delta_{\partial v}$ for the line of sight peculiar velocity gradient. β factors denote the expansion coefficients of the corresponding quantity (Furlanetto et al. (2006); Zaldarriaga et al. (2004)). The quantity of interest is the Fourier transform, $\delta_{\rm HI}(\mathbf{k})$. The power spectrum $P_{\rm HI}$ can be defined as:

$$\langle\delta^*_{\rm HI}(\mathbf{k})\delta_{\rm HI}(\mathbf{k'})\rangle = (2\pi)^3\delta^3(\mathbf{k}-\mathbf{k'})P_{\rm HI}(k) \tag{1.12}$$

where $\delta^3(x)$ is the Dirac delta function and the angular brackets denote an ensemble average. Statistical homogeneity and isotropy of the Universe suggest that the fluctuation in 21 cm signal should be spherically symmetric in the Fourier domain. This implies that the constructed power spectrum $P_{\rm HI}(k)$ from this fluctuation should only depend on the magnitude of the wave vector $|\mathbf{k}|$ (Pritchard & Loeb (2010)). Although redshift space distortions (Shaw & Lewis (2008); Mao et al. (2012)) due to peculiar velocities along line of sight break this spherical symmetry and only cylindrical symmetry is retained. Foregrounds in general do not follow any such symmetry, and this particular feature provide an important tool to separate foregrounds from HI signal in Fourier space (Morales & Hewitt (2004)). On large scales, the Fourier transform of fractional perturbation in the radial peculiar velocity gradient is proportional to that of the density field $\delta_{\partial v} = -\mu^2\beta\delta$. In general the fluctuation in Fourier space can be written as (Barkana & Loeb (2005); Furlanetto (2016)):

$$\delta_{\rm HI} = \mu^2\beta\delta + \delta_{\rm iso} \tag{1.13}$$

where $\delta_{\rm iso}$ consists of all statistically isotropic terms in Eq. (1.11), $\mu = \hat{k}\cdot\hat{x}$ i.e. the cosine value of the angle between the wave vector $\hat{k}$ and line of sight $\hat{x}$, β is the bias parameter which corrects for a possible bias between the tracers and the growth rate of dark matter perturbations. The power spectrum can be calculated by taking autocorrelation of above equation and setting $\beta = 1$:

$$P_{\rm HI}(k) = \mu^4 P_{\delta\delta} + 2\mu^2 P_{\delta_{\rm iso}\delta} + P_{\delta_{\rm iso}\delta_{\rm iso}} \tag{1.14}$$

where 'second order' terms are neglected. We can infer from above equation that by measuring power for 3 or more values of μ, one can determine $P_{\delta\delta}$, $P_{\delta_{\rm iso}\delta}$ and $P_{\delta_{\rm iso}\delta_{\rm iso}}$. So, in principle the contribution from density fluctuation $P_{\delta\delta}$ can be isolated (Furlanetto et al. (2006)). The other two components contain various different power spectrum including density, neutral fraction and spin temperature, along with their cross power spectrum.

The study of this statistical fluctuation in 21 cm signal or its variant, the power spectrum, has been a major aim of many radio interferometers operating in frequency range $80 < \nu < 300\,$MHz. For example, Low Frequency Array (LOFAR, Van Haarlem et al. (2013)), 21 Centimeter Array (21CMA, Zheng et al. (2016)), Giant Meterwave Radio Telescope

(GMRT, Paciga et al. (2013)), Donald C. Backer Precision Array for Probing the Epoch of Reionization (PAPER, Parsons et al. (2014)), Murchison Widefield Array (MWA, Tingay et al. (2013); Lonsdale et al. (2009); Bowman et al. (2009)). In addition to these ongoing efforts, larger futuristic experiments are planned which include Hydrogen Epoch of Reionization Array (HERA, DeBoer et al. (2016)) and Square Kilometer Array (SKA[1]).

1.5 Challenges in EoR study

There are mainly two types of experiments to study the reionization epoch. One tries to detect the global signal through single dish measurements, the other type has the power spectrum detection approach as discussed in previous section. In this thesis work we focus on the latter one. Even though the detection of redshifted HI line from the EoR remains the most direct approach to study this epoch, one of the most challenging parts is to extract the Cosmological signal from the observed data and decipher it correctly. There are also following issues which constraint the detectability of 21 cm signal from this epoch.

- Unlike CMBR anisotropies, the theoretical modeling of the HI signal from the EoR is considerably harder principally owing to uncertainty in the nature of ionizing sources and the details of their formation and evolution.

- The signal is expected to be weak with brightness temperature $T_{\rm B} \simeq 10\,{\rm mK}$. Many hundred hours of observation is needed to detect such a signal with current interferometers, with the attendant complication of maintaining instrumental stability for such long periods.

- The frequency range required ($80{\rm MHz} \leq \nu \leq 300{\rm MHz}$) to probe the relevant redshifts are widely used by many communication instruments (FM radio band, satellite and aircraft communication channels). This causes enormous radio frequency interference (RFI) which is many order of magnitude higher than the 21 cm signal. To escape from RFI, the observatories are often placed isolated from the contaminating sources.

[1] https://www.skatelescope.org/

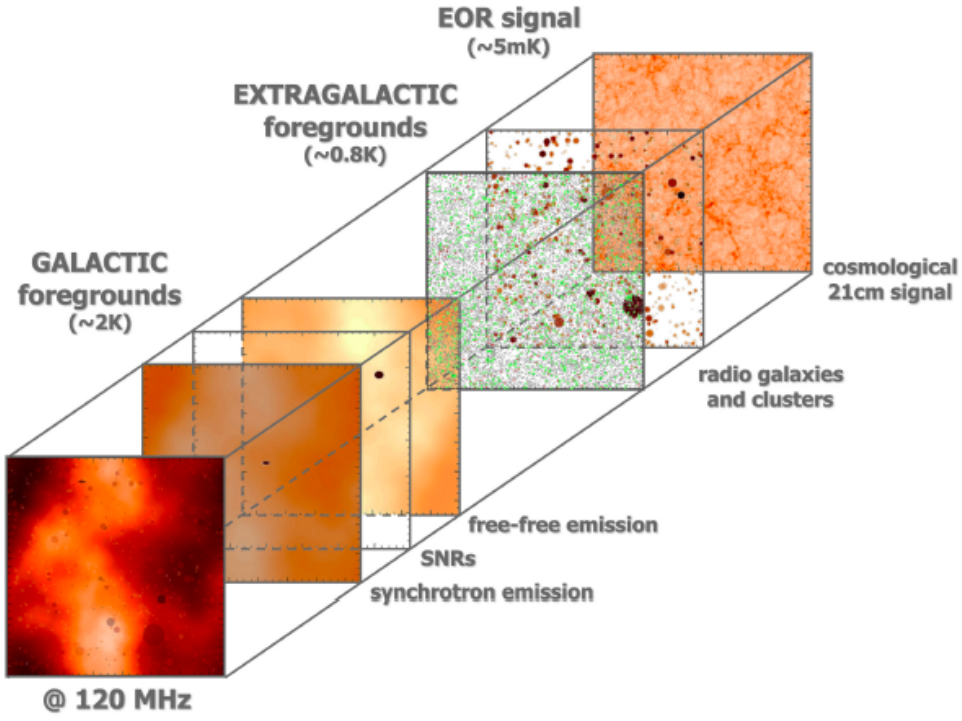

Figure 1.7: Foregrounds at 120 MHz (credit: Zaroubi (2013))

- The ionosphere poses a big challenge in all EoR endeavours. In the required frequency band, the ionosphere is refractive and gets opaque at lower frequency. The refraction phenomenon causes apparent movement of sources in the sky as ionospheric patches move across the telescope beam. The ionosphere being more active during daytime and large brightness of the Sun in this frequency band, observations are restricted only during the night.

- The foreground are expected to be many orders of magnitude larger than the signal. The most outstanding is the synchrotron emission from our galaxy which constitute approximately 75% of the total foregrounds. Radio galaxies, galaxy clusters, resolved supernovae remnants and free-free emission, together aggregate the remaining 25% of the foreground contribution. Fig. 1.7 shows these various foreground contribution compared to the expected EoR signal at 120 MHz (Zaroubi (2013)).

1.6 The Murchison Widefield Array

The Murchison Widefield Array (MWA, Tingay et al. (2013); Lonsdale et al. (2009); Bowman et al. (2009)), one of the precursor of the Square Kilometer Array (SKA), is a low frequency radio interferometer array located in Western Australia, a site with lower levels of radio frequency interference. It consists of 128 antenna tiles with each tile comprising of 16 crossed dipole antennas over a metal ground screen in 4 x 4 grid (with spacing of 1.1 m). The total collecting area of MWA is 2752 m^2 at 150 MHz. The majority of the tiles (112) are put within 1.5 km of core region, which makes it a high quality imaging array with resolution of few arcminutes. MWA bandwidth is 30.72 MHz, divided into 24 coarse channels of width 1.28 MHz each. This low frequency array operates in the frequency range 80 $\sim$ 300 MHz. The total bandwidth is divided into 768 fine channels. With the use of an analog beamformer appropriate phase delays are introduced in each individual dipole antenna to track the pointing center of the beam across the sky. This array has a unique $1/r^2$ type distribution of tiles with a dense core of antennas of short spacings (Bowman et al. (2009)). The short spacing antennas are useful for EoR power spectrum estimation, while the antennas with large separations are appropriate for calibration and imaging purpose. The wide field of view of the array is also useful to achieve sensitivity of EoR. These features make MWA an excellent EoR instrument. Other than EoR, other science goals of MWA include Galactic science, Time domain astrophysics and Space weather.

Fig. 1.8 shows individual tiles consisting of 16 dipoles. The locations of all 128 tiles are shown in Fig. 1.9.

1.7 Motivations and plan of the thesis

The probe of the Epoch of Reionization (EoR) remains one of the challenging aims of modern cosmology. In the past decade, many interesting details have emerged about this epoch from a host of cosmological observables. Gunn-Peterson (GP) tests on spectra of quasi-stellar objects (QSOs) ((Fan et al. (2000)) in the redshift range $5.7 < z < 6.3$ suggest that the universe was making a transition to full reionization during this period. On the other hand, Cosmic microwave background radiation (CMBR) temperature and polarization

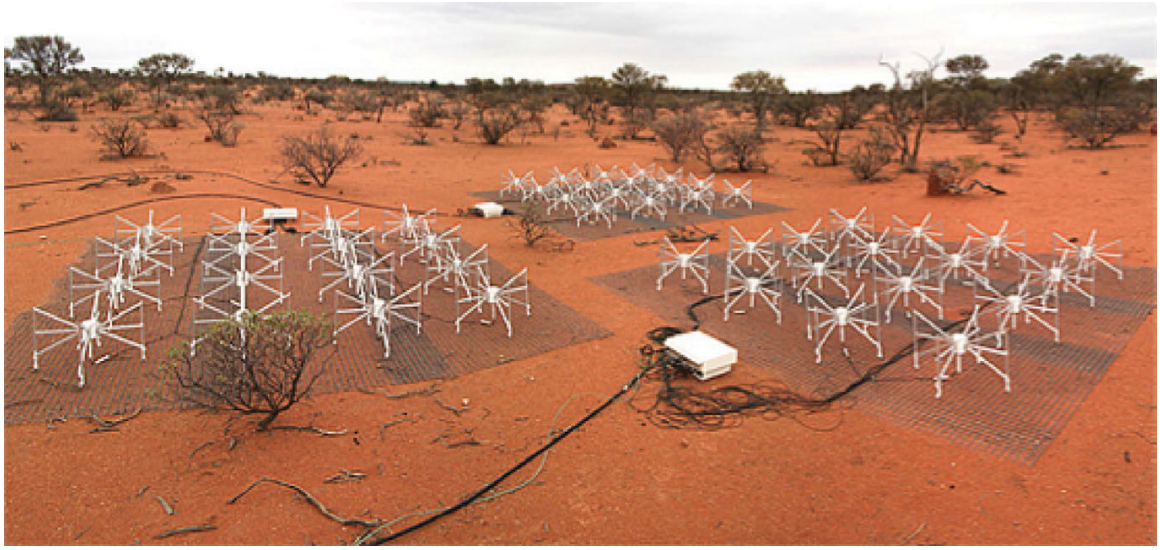

Figure 1.8: MWA tile with analog beamformer (credit: Tingay et al. (2013))

anisotropy measurements (Komatsu et al. (2010), Planck 2015 results. XIII. (2015)) suggest that the universe might have been fully ionized in a redshift range $8 < z < 10$ (Planck 2016 results. XLVII. (2016)).

Major experimental efforts are currently being undertaken to study the EoR in redshifted 21-cm line emission from the epoch. In particular, many radio interferometers in frequency range $80 < \nu < 300\,\mathrm{MHz}$ are currently operational that specifically aim to detect the EoR, for example LOFAR, 21CMA, GMRT, PAPER, MWA. In near future the Square Kilometer Array (SKA) is expected to have promising potential to reach the required sensitivity to detect EoR. With all these experiments going on, it's extremely important to work on the various algorithms and methods to extract various information from the observed data.

In this thesis work we have worked on methodologies to extract the EoR from observed data. We have developed an independent pipeline to calculate the power spectra in delay space from radio interferometric tracking data. This pipeline is applicable to imaging arrays like MWA and LOFAR. We also discuss the prospects of an alternate 'Drift scan' strategy which may be a viable and potentially superior approach to detect EoR.

In Chapter 2, we discuss the EoR measurement science where we explain the connections between the radio interferometric observation and EoR parameters.

In Chapter 3, we describe the pipeline which estimate the delay power spectra from

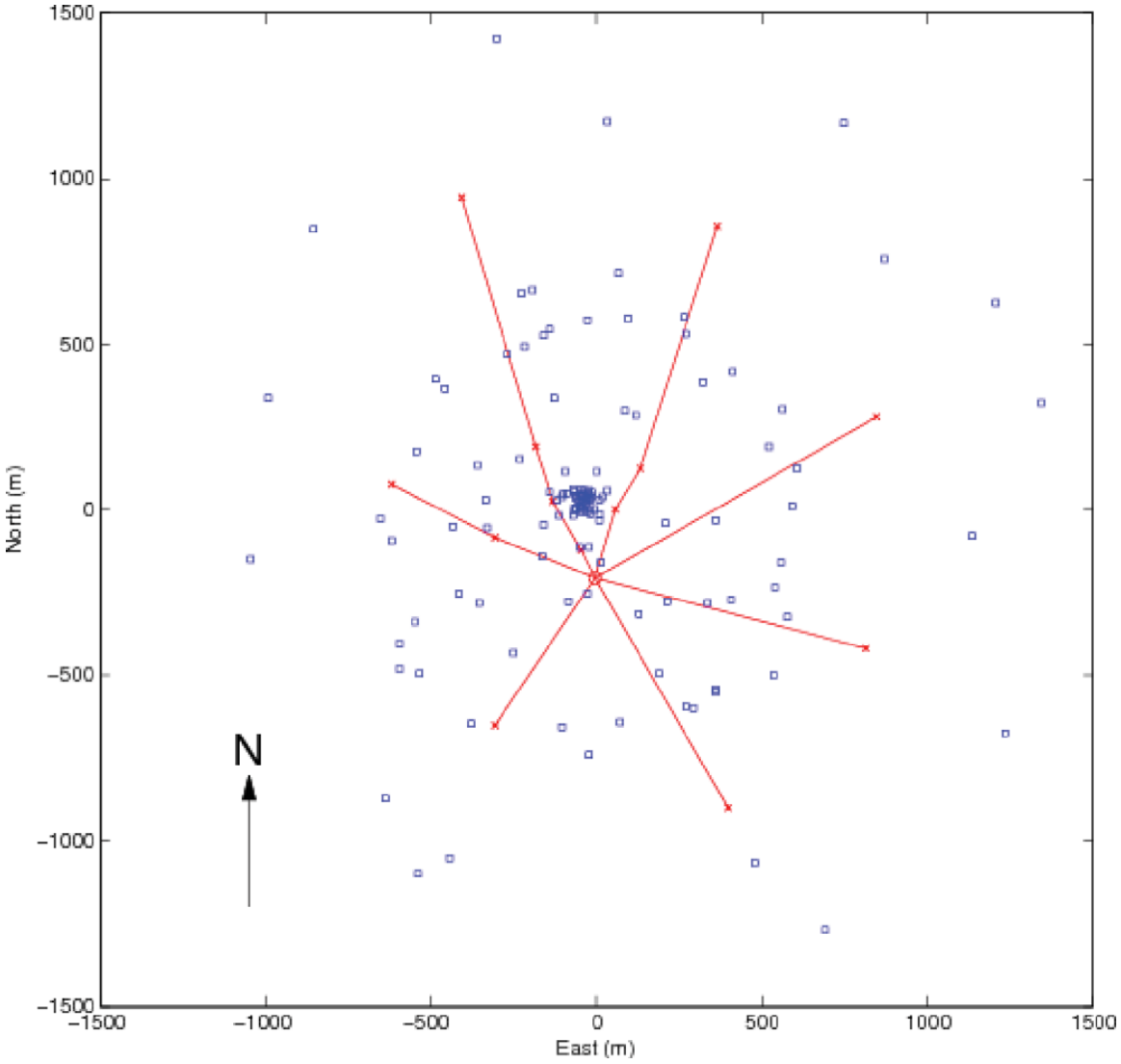

Figure 1.9: MWA tile locations (credit: Tingay et al. (2013))

tracking observation. We present analysis of 3 hours of real MWA tracking data and estimate both 2-dimensional $(k_{\parallel}, k_{\perp})$ and 1-dimensional (k) power spectra.

Chapter 4 explains the prospects of the alternate 'Drift scan' strategy towards EoR detection by comparing various observing modes.

In Chapter 5, we conclude the thesis work and discuss few future projects that can be carried out as extension of this work.

Throughout this thesis, we have used the Planck+WP best fit values of cosmological parameters: $\Omega_{\rm m0} = 0.3183$, $\Omega_{\Lambda 0} = 0.6817$, $\Omega_{\rm b0}\, h^2 = 0.02203$, $h = 0.6704$, $\sigma_8 = 0.8347$, and $n_{\rm s} = 0.9619$ Planck 2015 results. XIII. (2015); Planck 2013 results. XVI. (2013).

Chapter 2

EoR measurement Science

In this chapter we discuss the connection between radio interferometric observations and EoR observables. The basic aim of a radio interferometer is to calculate the spatial correlation of the electric fields from a distant source in the sky. The simplest radio interferometer consists of two antennas A_1 and A_2 separated by a distance $\mathbf{B}$. The schematic of such system is shown in Fig. 2.1. The system points towards a direction at sky, denoted by unit vector $\mathbf{s}$. The signal from the each radio antennas pass through an amplifier, and then they are correlated and averaged. The output of the correlator is called 'visibility', and can be written as

$$V_\nu(\tau_g) = \langle E_1(\nu, t) E_2^*(\nu, t + \tau_g) \rangle \tag{2.1}$$

where E_1 and E_2 represents the input waveforms to the correlator, and angular brackets denote time averaging. τ_g is called the 'geometric delay' (as shown in Fig. 2.1) and is given by:

$$\tau_g = \frac{\mathbf{B} \cdot \mathbf{s}}{c} = ul + vm + w\sqrt{1 - l^2 - m^2} \tag{2.2}$$

where c is the speed of light. The baseline vector is related to the physical separation between the two antennas such as: $\frac{\mathbf{B}}{\lambda} = (u, v, w)$; u points in the local east direction while v points north, w is along the direction of interest (Fig. 2.2); for a given baseline $\mathbf{B}$, $w = \mathbf{B} \cdot \mathbf{s}_0 \frac{\nu}{c}$ where $\mathbf{s}_0$ is the phase center. The measured 'visibility' for a sky pattern $I_\nu(l, m)$ can be shown to be (Thompson et al. (1986)):

$$V_\nu(u, v, w) = \int A_\nu(l, m) I_\nu(l, m) e^{-i2\pi\left[(ul+vm+w(\sqrt{1-l^2-m^2}-1)\right]} \frac{dldm}{\sqrt{1 - l^2 - m^2}} \tag{2.3}$$

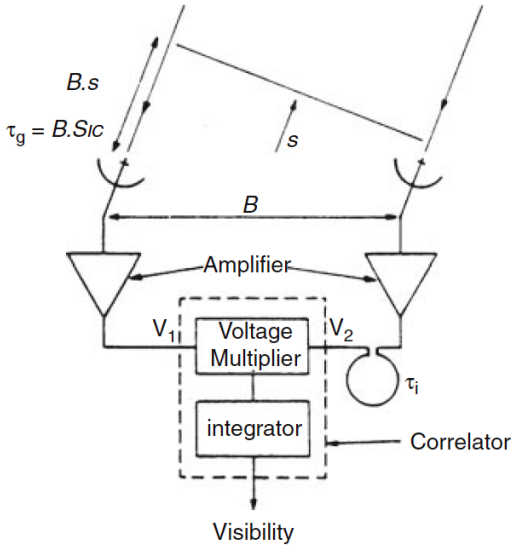

Figure 2.1: A schematic of two element interferometer. (credit: Wilson et al. (2009))

where (u, v, w) denotes the baseline vector joining a pair of antennas, measured in units of wavelength, projected onto a plane perpendicular to the direction of observation and (l ,m) refers to the position on the sky. $A_\nu(l, m)$ and $I_\nu(l, m)$ are the primary beam pattern and observed sky intensity at frequency ν respectively. The measured visibility receives contributions from the redshifted HI line, the foregrounds and thermal noise. We discuss them in detail in next sections.

2.1 HI signal

In the case of high-redshift HI emission, the specific intensity from any direction $\vec{\theta}$ at the redshifted frequency $\nu = 1420/(1 + z)$ MHz, can be decomposed into two parts:

$$I_\nu(\vec{\theta}) = \bar{I}_\nu + \Delta I_\nu(\vec{\theta}) \tag{2.4}$$

where $\bar{I}_\nu$ and $\Delta I_\nu(\vec{\theta})$ are the isotropic and fluctuating components of the specific intensity; $\vec{\theta}(l, m)$ denote the position on the sky.

This allows us to express the visibility arising from HI emission as:

$$V_\nu(\mathbf{u}) = \int A(\vec{\theta}) \Delta I_\nu(\vec{\theta}) e^{-i2\pi \mathbf{u}\cdot\vec{\theta}} d^2\theta \tag{2.5}$$

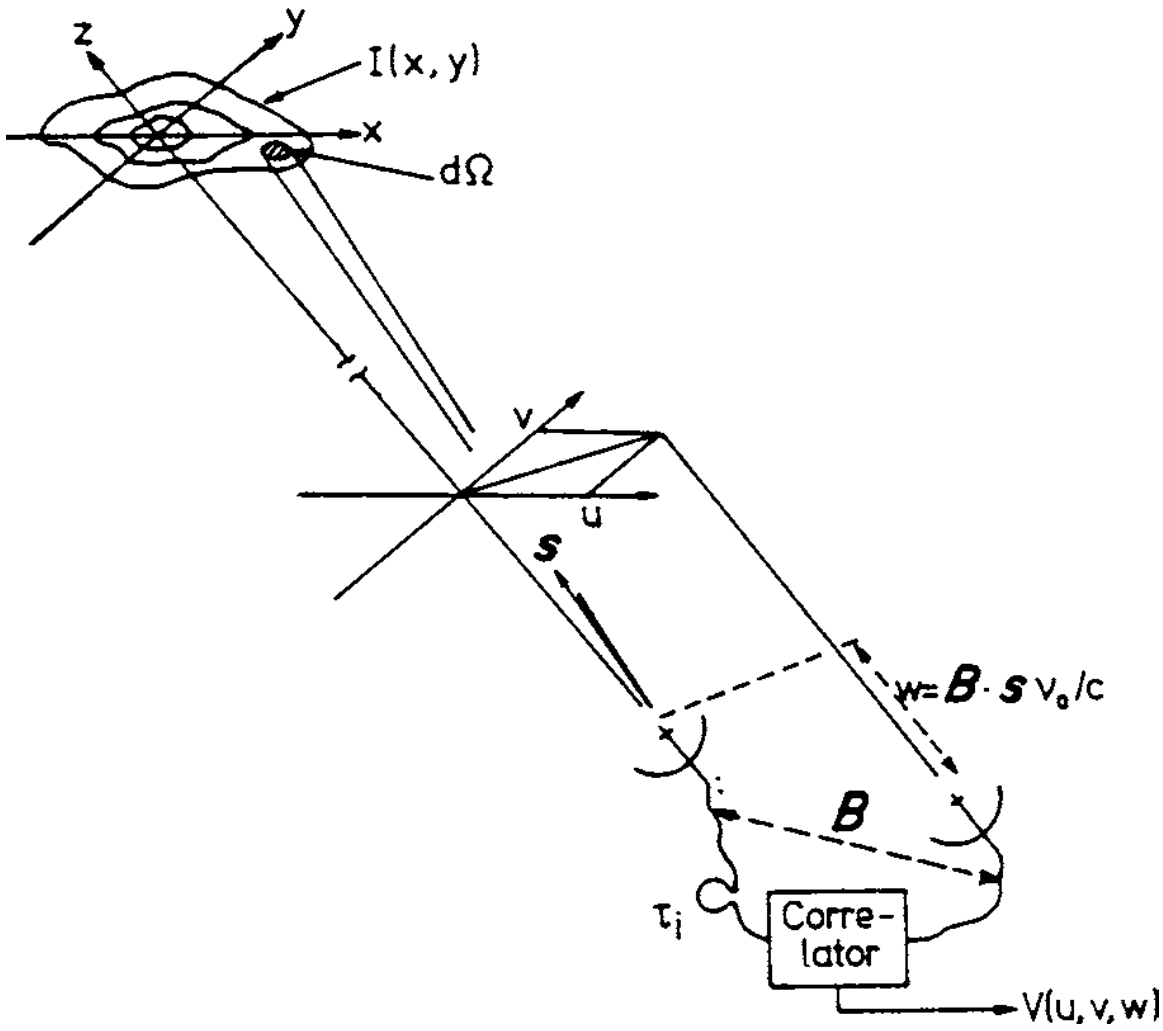

Figure 2.2: Schematic diagram describing the u, v, w coordinates. (Thompson et al. (1986))

where $\mathbf{u}(u, v)$ denotes the baseline vector. Here only the fluctuating component appears since the isotropic component does not contribute to the visibility[1]. We show in next chapter that inclusion of w-term causes an effective shrinking of primary beam for HI signal, which further results in decorrelation in the desired signal. In real interferometer baseline distribution, w component of baseline vector is never zero. Thus for practical consideration we need to calculate the decorrelation factor of the HI signal due to non-zero w contribution compared to $w = 0$ case. Therefore we begin with the case where $w = 0$ and drop the w-term in writing the relation between the visibility and specific intensity in Eq. (2.5). We compute the contribution of non-zero w in next chapter.

The fluctuating component of HI emission can be expressed in terms of $\delta_{\rm HI}(\mathbf{k})$, the Fourier transform of the fluctuation of HI signal $\delta_{\rm HI}(\mathbf{x})$ in Eq. (1.11): (Bharadwaj & Sethi (2001); Morales & Hewitt (2004)):

$$\Delta I_\nu(\vec{\theta}) = \bar{I}_\nu \int \frac{d^3k}{(2\pi)^3} \delta_{\rm HI}(\mathbf{k}) e^{ir_\nu(k_\parallel + \mathbf{k}_\perp . \vec{\theta})} \tag{2.6}$$

Here $k_\parallel$ and $\mathbf{k}_\perp$ refer to the components of comoving wave vector $\mathbf{k}$ along line of sight and in the plane of the sky respectively and r_ν is the comoving distance. With these definitions we can expand the phase term $\mathbf{k}.\mathbf{r}$, as shown in Eq. (2.6). The 3D Fourier transform can be understood as performing 1D Fourier transform along the line of sight followed by a 2D fourier transform on the sky plane, or $d^3k = dk_\parallel d^2k_\perp$. Eq. (2.5) can thus be expressed as:

$$V_\nu(\mathbf{u}) = \bar{I}_\nu \int \frac{d^3k}{(2\pi)^3} \delta_{\rm HI}(\mathbf{k}) e^{ir_\nu k_\parallel} \int d^2\theta A(\vec{\theta}) \exp\left[-2\pi i \left(\mathbf{u} - \frac{\mathbf{k}_\perp r_\nu}{2\pi}\right).\vec{\theta}\right] \tag{2.7}$$

The second integral over the primary beam $A(\vec{\theta})$ can be denoted as:

$$a\left(\mathbf{u} - \frac{\mathbf{k}_\perp r_\nu}{2\pi}\right) \equiv \int d^2\theta A(\vec{\theta}) \exp\left[-2\pi i \left(\mathbf{u} - \frac{\mathbf{k}_\perp r_\nu}{2\pi}\right).\vec{\theta}\right] \tag{2.8}$$

Thus, finally Eq. (2.7) takes the form:

$$V_\nu(\mathbf{u}) = \bar{I}_\nu \int \frac{d^3k}{(2\pi)^3} \delta_{\rm HI}(\mathbf{k}) e^{ir_\nu k_\parallel} a\left(\mathbf{u} - \frac{\mathbf{k}_\perp r_\nu}{2\pi}\right) \tag{2.9}$$

Eq. (2.9) carries the signature of HI fluctuations to the measured visibility. As discussed in Eq. (1.12), the power spectrum $P_{\rm HI}(k)$ can be constructed from the fluctuation of HI

[1]However some methods have been discussed in recent literatures to extract monopole signal from interferometric measurements (Presley et al. (2015); Singh et al. (2015))

signal in Fourier space $\delta_{\rm HI}(k)$. This implies that the HI power spectrum can be estimated from the correlation of the observed visibilities. Having defined the visibility for HI signal in Eq. (2.9), the visibility correlation function can be expressed as:

$$\langle V_\nu(\mathbf{u}) V^*_{\nu+\Delta\nu}(\mathbf{u}')\rangle = \bar{I_\nu}^2 \int \frac{d^3k}{(2\pi)^3} P_{\rm HI}(k) e^{ik_\parallel \Delta r_\nu} a\left(\mathbf{u} - \frac{\mathbf{k}_\perp r_\nu}{2\pi}\right) a\left(\mathbf{u}' - \frac{\mathbf{k}_\perp r_{\nu+\Delta\nu}}{2\pi}\right) \quad (2.10)$$

Here assuming that the frequency coverage is far smaller than the central frequency: $\Delta\nu << \nu$, one can write: $|r_{\nu+\Delta\nu} - r_\nu| \equiv \Delta r_\nu = r'_\nu |\nu' - \nu|$; here $r'_\nu \equiv |dr_\nu/d\nu|$. We note that the volume element in k-space: $d^3k = dk_\parallel dk_{\perp 1} dk_{\perp 2}$; $k_{\perp 1}$ and $k_{\perp 2}$ are mutually perpendicular axes on the sky plane, while $k_\parallel$ is along the line of sight.

The isotropic part of the emission can be calculated as (Bharadwaj & Sethi (2001)):

$$\bar{I_\nu} = \frac{A_{21} h_P c \bar{n}_{\rm HI}(z)}{4\pi H(z)} \quad (2.11)$$

Here A_{21} is the Einstein coefficient of the 21 cm HI transition, $\bar{n}_{\rm HI}(z)$ denotes the mean comoving number density of HI atoms in the excited state at a redshift z; h_P, c are the Planck constant and speed of light respectively. $H(z)$ is the Hubble parameter defined as:

$$H(z) = H_0 \left[\Omega_{m0}(1+z)^3 + \Omega_{\Lambda 0}\right]^{1/2} \quad (2.12)$$

2.1.1 Delay power spectrum

A special variant among the visibility based power spectrum estimators is 'delay spectrum' (Pober et al. (2013); Parsons et al. (2012b, 2014)), which directly Fourier transforms each calibrated visibility along its frequency channels. In this section we describe the construction of HI power spectrum using visibility correlations in delay space. In delay space, spectrally smooth foregrounds lend themselves to ready interpretation. It can be shown that visibilities computed in delay space allow isolation of such foregrounds from the regions dominated by the HI signal and noise (e.g. see Datta et al. (2010); Vedantham et al. (2012); Parsons et al. (2012b); Liu et al. (2014); Dillon et al. (2014); Thyagarajan et al. (2013, 2015a)). However, the properties of HI signal can only be inferred after visibilities are correlated. The Fourier conjugate variable (τ) of the channel axis for each baseline effectively captures signal delay between the antenna pairs. However in the context spatial HI power spectrum, the quantity sought after is η which is the Fourier conjugate variable of spatial frequency,

a measure of cosmological distance along line of sight. The mathematical correspondence between these two can be found in Parsons et al. (2012b); Liu et al. (2014). The 'delay spectrum' constructed from 'delay space' approach is closely related to cosmological spatial HI power spectrum with added advantage of dealing with 'visibilities' which are primary data measurements by radio interferometers.

If ν is the frequency of observation, the visibility in delay space can be computed as:

$$V_\tau(\mathbf{u}) = \int \exp(i2\pi\tau\nu) V_\nu(\mathbf{u}_\nu) d\nu \tag{2.13}$$

Here τ, the conjugate variable of ν, defines the relevant variable in delay space; $\mathbf{u}_\nu = (u_\nu, v_\nu)$ is the baseline vector in units of wavelength. Hereafter, the frequency dependence of baseline vector is kept intact. The autocorrelation of $V_\tau(\mathbf{u})$ can be written as:

$$\begin{aligned}
\langle V_\tau(\mathbf{u}) V_\tau^*(\mathbf{u}')\rangle = & \int\int d\nu d\nu' \bar{I_\nu} \bar{I_{\nu'}} \int \frac{d^3k}{(2\pi)^3} P_{\rm HI}(k) \exp\left(i2\pi\tau(\nu'-\nu) + i(k_\parallel(r_{\nu'} - r_\nu)\right) \\
\times & \int d^2\theta \exp\left(i2\pi\vec{\theta}.\left(\mathbf{u}_\nu - \frac{\mathbf{k}_\perp r_\nu}{2\pi}\right)\right) A_\nu(\vec{\theta}) \\
\times & \int d^2\theta' \exp\left(-i2\pi\vec{\theta'}.\left(\mathbf{u'}_{\nu'} - \frac{\mathbf{k}_\perp r_{\nu'}}{2\pi}\right)\right) A_{\nu'}(\vec{\theta'})
\end{aligned} \tag{2.14}$$

To make further progress, frequency dependent quantities are Taylor expanded. For baselines, this is a straightforward re-expression of the baseline vector as the vector is linear in frequency: $\mathbf{u'}_{\nu'} = \mathbf{u'}_\nu + \Delta\nu d\mathbf{u'}_\nu/d\nu$ where $\Delta\nu = \nu' - \nu$. It should be noted that $d\mathbf{u'}_\nu/d\nu$ is the physical baseline length measured in units of time.

After the Taylor expansion of relevant quantities, r_ν and $\mathbf{u}_\nu$, we obtain:

$$\begin{aligned}
\langle V_\tau(\mathbf{u}) V_\tau^*(\mathbf{u}')\rangle = & \int\int d\nu d\nu' \bar{I_\nu} \bar{I_{\nu'}} \int \frac{d^3k}{(2\pi)^3} P_{\rm HI}(k) \int d^2\theta \exp\left(i2\pi\vec{\theta}.\left(\mathbf{u}_\nu - \frac{\mathbf{k}_\perp r_\nu}{2\pi}\right)\right) A_\nu(\vec{\theta}) \\
\times & \int d^2\theta' \exp\left(-i2\pi\vec{\theta'}.\left(\mathbf{u'}_\nu - \frac{\mathbf{k}_\perp r_\nu}{2\pi}\right)\right) A_{\nu'}(\vec{\theta'}) \\
\times & \exp\left[i\Delta\nu\left(2\pi\tau + k_\parallel dr_\nu/d\nu + d\mathbf{u'}_\nu/d\nu.\vec{\theta'} + dr_\nu/d\nu\mathbf{k}_\perp.\vec{\theta'}/(2\pi)\right)\right]
\end{aligned} \tag{2.15}$$

Here $\Delta\nu = \nu' - \nu$; all the quantities in Eq. (2.15) have been written as explicit functions of ν and $\Delta\nu$. This allows us to simplify the integral further by making the coordinate transform $y = (\nu + \nu')/2$ and $x = (\nu' - \nu)/2$; the Jacobian of this transformation is unity. We can make further simplification by using $y \simeq \nu$. This is justified for our case as we assume the

bandwidth to be $\simeq 10\,\mathrm{MHz}$ around a central frequency of $\simeq 150$ MHz. All the frequency dependent variables change by less than 10% for this case. This reduces Eq. (2.15) to:

$$\begin{aligned}\langle V_\tau(\mathbf{u})V_\tau^*(\mathbf{u}')\rangle &= \int\int d\nu dx \bar{I_\nu}^2 \int \frac{d^3k}{(2\pi)^3} P_{\mathrm{HI}}(k) \int d^2\theta \exp\left(i2\pi\vec{\theta}.\left(\mathbf{u}_\nu - \frac{\mathbf{k}_\perp r_\nu}{2\pi}\right)\right) A_\nu(\vec{\theta}) \\ \times &\int d^2\theta' \exp\left(-i2\pi\vec{\theta'}.\left(\mathbf{u'}_\nu - \frac{\mathbf{k}_\perp r_\nu}{2\pi}\right)\right) A_\nu(\vec{\theta'}) \\ \times &\exp\left[i2x\left(2\pi\tau + k_\parallel dr_\nu/d\nu + d\mathbf{u'}_\nu/d\nu.\vec{\theta'} + dr_\nu/d\nu\mathbf{k}_\perp.\vec{\theta'}/(2\pi)\right)\right] \end{aligned} \tag{2.16}$$

Given the HI power spectrum $P_{\mathrm{HI}}(k)$ this integral could be computed numerically. However, it is possible to determine the correlation scales in both the transverse and line of sight directions by carefully examining Eq. (2.16). The integral over angles shows that the dominant contribution comes from wavenumbers such that $\mathbf{k}_\perp \simeq 2\pi\mathbf{u}_\nu/r_\nu$. This relation allows us to simplify the integrals over θ, θ' and x. In particular, different terms in the exponent containing τ can be estimated. Using $d\mathbf{u}_\nu/d\nu = \mathbf{u}_\nu/\nu$, the last two terms in the exponents are on the order of $\mathbf{k}_\perp.\vec{\theta'}r_\nu/(2\pi\nu)$ (the term containing $dr_\nu/d\nu$ is slightly smaller because $\nu/r_\nu dr_\nu/d\nu \simeq 0.3$). For MWA primary beam, $\theta_0 \simeq 0.3$, and for MWA baseline distribution, the term $k_\parallel dr_\nu/\nu$ generally dominates over these terms, especially in the regions dominated by EoR. For all our calculations we use parameters specific to MWA, in particular, the primary beam of MWA. However, the formulation presented here is general enough to be applicable to other arrays.

By dropping the last two terms, which are subdominant, in the exponent containing τ, we can separate the integrals over x and angles, this gives us:

$$\begin{aligned}\langle V_\tau(\mathbf{u})V_\tau^*(\mathbf{u}')\rangle &= \int d\nu \bar{I_\nu}^2 \int \frac{d^3k}{(2\pi)^3} P_{\mathrm{HI}}(k) \int d^2\theta \exp\left(i2\pi\vec{\theta}.\left(\mathbf{u}_\nu - \frac{\mathbf{k}_\perp r_\nu}{2\pi}\right)\right) A_\nu(\vec{\theta}) \\ \times &\int d^2\theta' \exp\left(-i2\pi\vec{\theta'}.\left(\mathbf{u'}_\nu - \frac{\mathbf{k}_\perp r_\nu}{2\pi}\right)\right) A_\nu(\vec{\theta'}) \int dx \exp\left[i2x\left(2\pi\tau + k_\parallel dr_\nu/d\nu\right)\right] \end{aligned} \tag{2.17}$$

The integral over x can readily be carried out now. The dominant contribution to the integral comes from $\tau \simeq k_\parallel/(2\pi)dr_\nu/d\nu$, which establishes the correlation scale in the direction along the line of sight. The variation of frequency dependence of integrals over θ and θ' is expected to be small for the bandwidth of MWA and therefore these integrals can be computed at some frequency that lies within the bandwidth. We assume these values to be fixed at the central frequency $\nu = 154\,\mathrm{MHz}$ and use them to compute the relations in Eq (2.18). If the

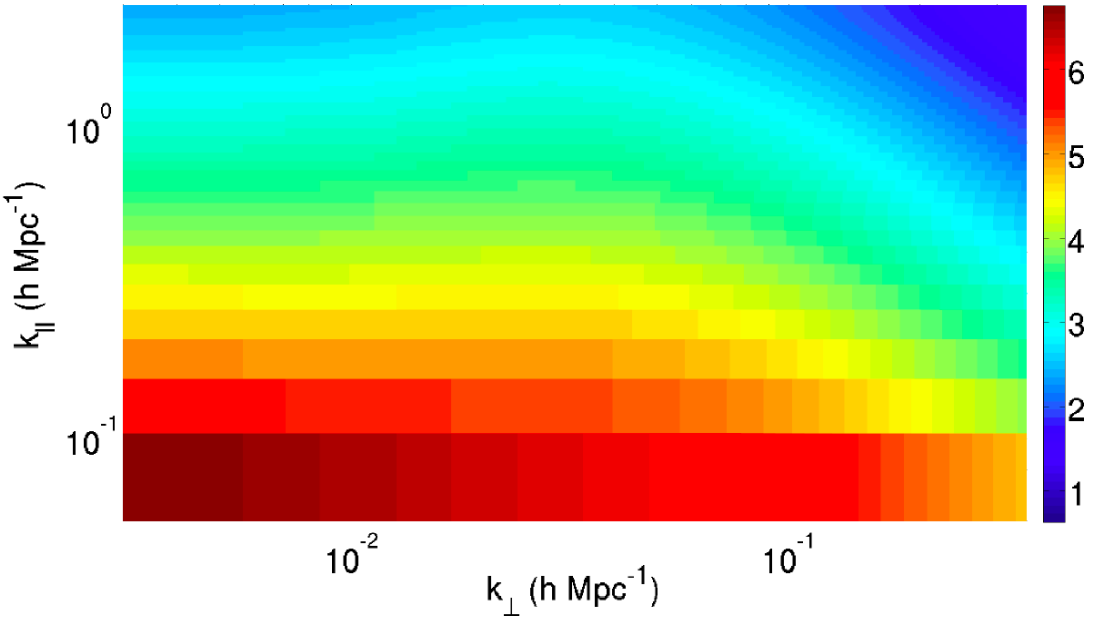

Figure 2.3: Power spectra of the expected Cosmological HI signal. The power is plotted as $log_{10}P$ where P is in units $mK^2(Mpc/h)^3$.

frequency dependence of the primary beam and the background intensity are neglected, the integral over ν in trivial. As noted above, this is a good approximation for MWA. The power spectrum of the HI signal, based on Eq. (2.17), is shown in Figure 2.3. In this calculation, we use the HI power spectrum $P_{\rm HI}(k)$ given by the simulation of Furlanetto et al. (2006).

Eqs. (2.17) and (2.10) can be used to infer many important properties of the HI signal:

1. There exists a near one-to-one relation between $\mathbf{u}$, τ and the Fourier components of the HI power spectrum (Parsons et al. (2012a,b); Paul & Sethi et al. (2014); Morales & Hewitt (2004)):

$$u_\nu = \frac{k_{\perp 1} r_\nu}{2\pi}, \quad v_\nu = \frac{k_{\perp 2} r_\nu}{2\pi}, \quad \tau = \frac{k_\parallel c(1+z)^2}{2\pi H_0 \nu_{21} E(z)} \tag{2.18}$$

where ν_{21} is the rest frame frequency of the 21 cm line, r_ν is the transverse comoving distance, $E(z) = \sqrt{\Omega_M(1+z)^3 + \Omega_k(1+z)^2 + \Omega_\Lambda}$ and z is the redshift corresponding to the observed frequency ν. The relation between $k_\parallel$ and τ follows from the relation: $2\pi\tau = k_\parallel dr_\nu/d\nu$ (Eq. (2.17)). As noted above, all the frequency dependent quantities in Eq. (2.18) are computed as a fixed frequency $\nu_0 = 154\,\mathrm{MHz}$.

2. The correlations in the sky plane and along the line of sight are nearly separable. This allows us to compute weights in the plane of the sky owing to w-term and the distortion of intensity pattern in a tracking run (the next two subsections) without the additional complication owing to frequency dependence of these quantities.

3. Eqs. (2.17) and (2.18) allow us to simplify the relation between visibility correlation and the HI power spectrum. Eq. (2.17) can be solved in the limit defined by Eq. (2.18) to give (e.g. Thyagarajan et al. (2015a); Pen et al. (2009); Morales (2005); McQuinn et al. (2006)):

$$\langle V_\tau(\mathbf{u}) V_\tau^*(\mathbf{u}) \rangle = \frac{\bar{I_\nu}^2 \Delta\nu \theta_0^2}{r_\nu^2 dr_\nu/d\nu} P_{\rm HI}(k) \tag{2.19}$$

Here the MWA primary beam solid angle $\theta_0^2 = \lambda^2/A_{\rm eff}$. For MWA $A_{\rm eff} = 21.5\,{\rm m}^2$ at 150 MHz (Tingay et al. (2013)). $\Delta\nu = 10.2\,{\rm MHz}$ is the total band width we use in this work. The mean specific intensity $\bar{I_\nu} = 2k_B T_B/\lambda^2$. This allows us to express the HI signal as the square of the product of mean brightness temperature and the HI power spectrum $T_B^2 P_{\rm HI}(k)$ in the units $(mK)^2(Mpc/h)^3$. It should be emphasized that Eq. (2.19) provides the suitable normalization only when $\mathbf{u}' = \mathbf{u}$, $w = 0$, as has been assumed throughout this section, and the impact of sky intensity distortion while tracking a region is not considered. All these effects act to lower the RHS of Eq. (2.19), the measured visibility correlation, for a fixed signal $T_B^2 P_{\rm HI}(k)$.

2.2 Foreground effects

The primary contribution to foregrounds come from spectrally smooth point and diffuse sources. They differ from the HI signal in both spatial and spectral behaviour. However, it is the latter difference that allows us to potentially isolate foregrounds from the HI signal in the power spectrum estimation.

To understand the impact of foregrounds in the data, we model them as a set of point sources. We note that if both the point and the diffuse sources have smooth spectra across the instrumental bandwidth, their impact on the power spectra are similar and therefore point sources allow us to capture adequately our ability to isolate foregrounds from the

signal. In this section, for analytic work, we assume $w = 0$. We note without further proof that this assumption doesn't alter our main inferences.

For a set of point sources, the intensity distribution is given by:

$$I_\nu(\vec{\theta}) = \sum_i F_{i\nu}\delta_D^2(\vec{\theta} - \vec{\theta}_i) \tag{2.20}$$

Here $F_{i\nu}$ and $\vec{\theta}_i$ are the source fluxes and positions, respectively. This allows us to compute the visibility for a given baseline $\mathbf{u}_\nu$ and frequency ν.

One major concern here is the contamination of foreground power to the clean regions. This occurs because of the rectangular bandpass window, whose sidelobes in Fourier space cause leakage of power. This leakage can be minimized by choosing an appropriate window function. For our purpose we choose a Blackman-Nuttall(BN) window (Fig. 2.4). So now the visibility expression will be:

$$V_\nu(\mathbf{u}_\nu) = \left[\sum_i F_{i\nu}\exp(i2\pi\mathbf{u}_\nu.\vec{\theta}_i)A_\nu(\vec{\theta}_i)\right] W_{\rm BN}(\nu) \tag{2.21}$$

Here A_ν is the primary beam, $W_{BN}(\nu)$ refers to the Blackman-Nuttall window (Nuttall (1981)). As discussed earlier, we also define a visibility in the conjugate space by taking the Fourier transform with respect to ν (Eq. (2.13)): $V_\tau(\mathbf{u})$. Our aim is to compute the correlation of this visibility:

$$\begin{aligned}\langle V_\tau(\mathbf{u})V^*_{\tau'}(\mathbf{u}')\rangle = \sum_i\sum_j \int d\nu \int d\nu' F_{i\nu}F_{j\nu'}W_{\rm BN}(\nu)W_{\rm BN}(\nu') \\ \times \quad \exp\left(i2\pi\left[\mathbf{u}_\nu.\vec{\theta}_i - \mathbf{u}'_{\nu'}.\vec{\theta}_j + (\tau\nu - \tau'\nu')\right]\right) A_\nu(\vec{\theta}_i)A_{\nu'}(\vec{\theta}_j)\end{aligned} \tag{2.22}$$

Both the source flux F_ν and primary beam $A_\nu(\vec{\theta})$ are functions of frequency, so it is difficult to analytically compute this expression. However, assuming smooth and small variation of both of these quantities across the bandwidth, we can make meaningful analytic estimates; we verify this assumption from detailed simulations and the analysis of the data (in next chapter). The main frequency variation in this case comes from the phase of the integral (the terms in the exponent) and in particular from the change in the baseline length as frequency changes. We note here that multiple correlations are available to us for this analysis for different pairs of $\{\tau, \tau'\}$ and $\{\mathbf{u}, \mathbf{u}'\}$. Here we assume $\tau = \tau'$.

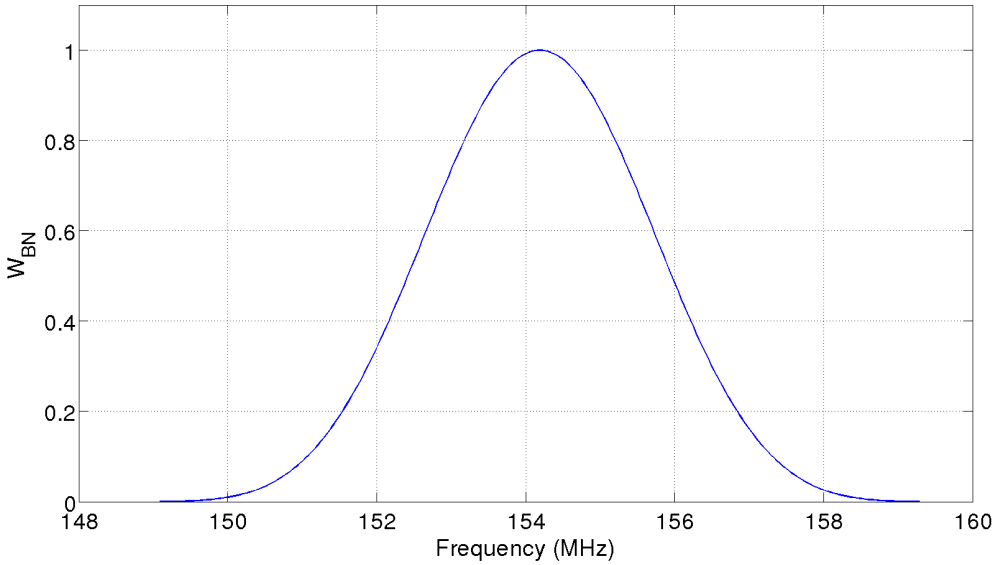

(a) Blackman-Nuttall window

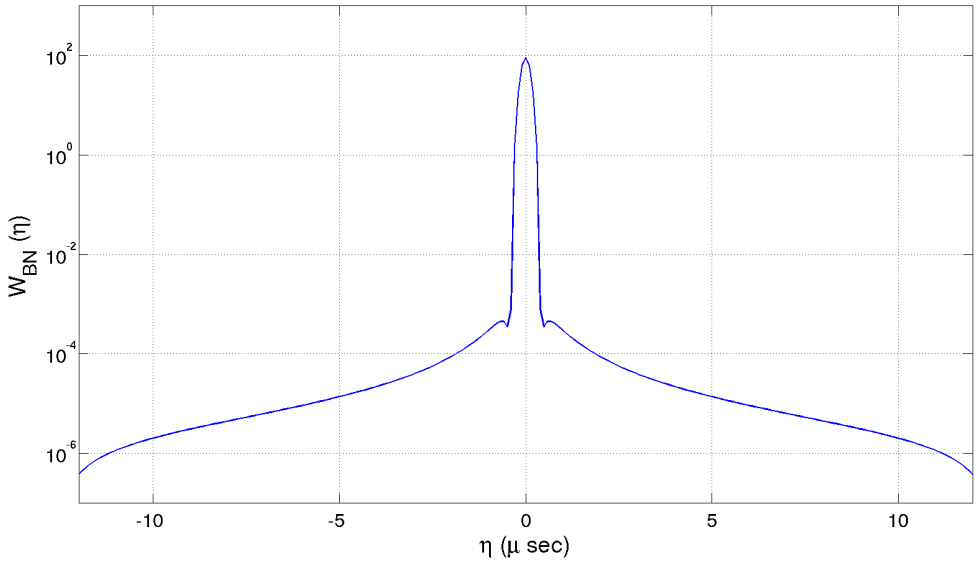

(b) Fourier transform of the window function

Figure 2.4: Blackman-Nuttall window (Nuttall (1981))

2.2.1 Delay space—foreground wedge

Here we expand the same baseline in frequency space: $\mathbf{u'}_{\nu'} = \mathbf{u}_\nu + d\mathbf{u}_\nu/d\nu(\nu' - \nu)$. In this case, $\mathbf{u}_\nu = \nu/\nu_0\mathbf{u}_{\nu_0}$, where ν_0 is some fixed frequency. Making the simplifying assumption that both point source fluxes and the primary beam are independent of frequency, Eq. (2.22) can be analytically integrated. We further make coordinate transformation: $x = (\nu' - \nu)/2$ and $y = (\nu' + \nu)/2$ and assuming $\nu' = \nu$ in all the quantities except those in the exponent containing their difference, which allows us to use $y \simeq \nu$:

$$\langle V_\tau(\mathbf{u}) V^*_{\tau'}(\mathbf{u}')\rangle \simeq \sum_i \sum_j \int dx \int dy F_{i\nu} F_{j\nu} W^2_{\rm BN}(\nu)$$
$$\times \quad \exp\left(i2\pi\left[\mathbf{u}_\nu.\vec{\theta}_i - \mathbf{u}_\nu.\vec{\theta}_j + 2(d\mathbf{u}_\nu/d\nu.\vec{\theta}_i - \tau)x\right]\right) A_\nu(\vec{\theta}_i) A_\nu(\vec{\theta}_j) \tag{2.23}$$

Integrals over x and y are now separated which gives us:

$$\langle V_\tau(\mathbf{u}) V^*_{\tau'}(\mathbf{u}')\rangle \propto \int dx \exp\left[-i2\pi(d\mathbf{u}_\nu/d\nu.\vec{\theta}_i - \tau)x\right] \tag{2.24}$$

As noted above, $d\mathbf{u}_\nu/d\nu = \mathbf{u}_{\nu_0}/\nu_0$, or it is independent of frequency. The integral in the equation is insignificant only when $\tau \simeq d\mathbf{u}/d\nu.\theta_i$. This linear relation between τ and the baseline $\mathbf{u}$ gives a region bounded by a 'wedge' in the τ–$d\mathbf{u}/d\nu.\theta_i$ space for a spatial distribution of point sources (e.g. see Datta et al. (2010); Vedantham et al. (2012); Parsons et al. (2012b); Liu et al. (2014); Dillon et al. (2014); Thyagarajan et al. (2013, 2015a)).

Another possible way to understand the nature of spectrally smooth foregrounds is to first compute the correlation in the frequency space. Using Eq. (2.21), this gives us:

$$\langle V_\nu(\mathbf{u}_\nu) V^*_{\nu'}(\mathbf{u'}_{\nu'})\rangle = \sum_i \sum_j F_{i\nu} F_{j\nu'} W_{\rm BN}(\nu) W_{\rm BN}(\nu') \exp\left(i2\pi\left[\mathbf{u}_\nu.\vec{\theta}_i - \mathbf{u'}_{\nu'}.\vec{\theta}_j\right]\right) A_\nu(\vec{\theta}_i) A_{\nu'}(\vec{\theta}_j) \tag{2.25}$$

Using $\mathbf{u'}_{\nu'} = \mathbf{u}_\nu + \Delta\nu\mathbf{u}_{\nu_0}/\nu_0$ and substituting into Eq. (2.25), and performing a single Fourier transform with respect to $\Delta\nu$, we recover the main expected feature of the foreground 'wedge' described above. Computationally, if the variation of other quantities with frequency, primary beam and source fluxes, is neglected, this method is completely equivalent to the one based on Eq. (2.23).

Even though we used a set of point sources, the main inferences of the analysis also follow for diffuse sources. In particular, the frequency space integrals used to prove our case are exactly the same.

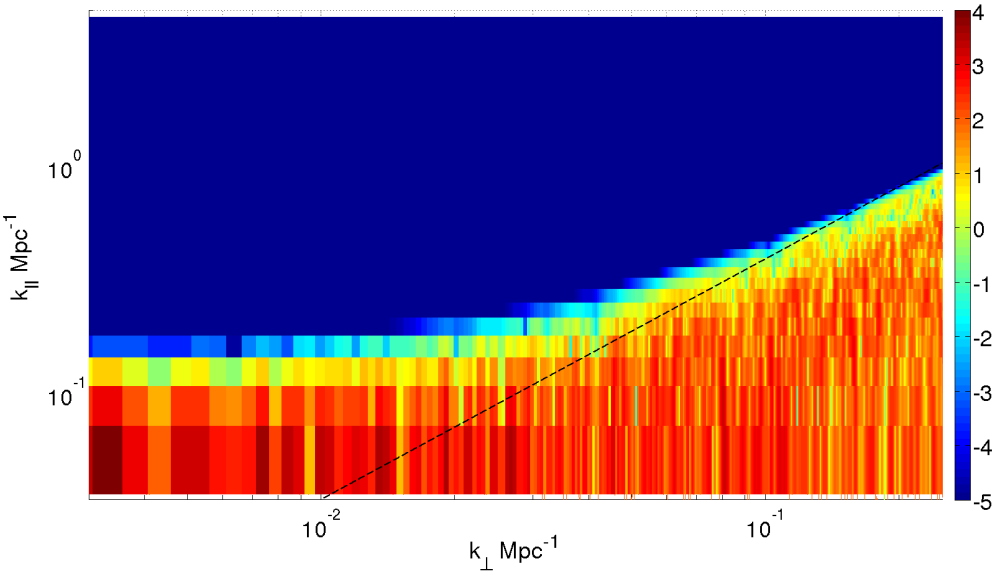

Figure 2.5: Foreground power spectrum shown in $(k_\parallel, k_\perp)$ plane. The unit of power is Jy^2. The contribution of foreground is isolated in the 'wedge' shaped region. The blue region ('EoR window') is expected to be free of foreground contamination and can be used for EoR power spectrum estimation.

For our simulations, we assume a set of point sources isotropically distributed with fluxes above 1 Jy at 150 MHz. We construct this flux distribution from radio source count at 1.4 GHz, which is given by (Hopkins et al. (2003)):

$$\log\left[\frac{dn/ds}{S^{-2.5}}\right] = \sum_{i=0}^{6} a_i \left[\log\left(\frac{S}{mJy}\right)\right]^i \tag{2.26}$$

for flux range 0.05 mJy $\leq$ S $\leq$ 1000 mJy. The constants are $a_0 = 0.859, a_1 = 0.508, a_2 = 0.376, a_3 = -0.049, a_4 = -0.121, a_5 = 0.057, a_6 = -0.008$. We simulate sources over the entire hemisphere (nearly 15000 sources) to suitably take into account the contribution from MWA primary beam sidelobes. We extrapolate the distribution to the frequencies of interest to us by assuming a spectral index $\alpha = -0.7$.

Fig. (2.5) shows the foreground power spectrum for the point source distribution discussed before. The 'wedge' shaped feature is clearly visible in the power spectrum. The space beyond the wedge is called 'EoR window' which is expected to be free of foregrounds and measurement of HI powers spectrum can be performed.

2.3 Thermal Noise and Sensitivity of HI power spectrum

At low frequency, thermal noise plays a prominent role in observed visibility. At our frequency of interest ($\nu \sim 154$ MHz), the sky itself is a dominant source of noise. At higher frequencies receiver noise starts to play a major role. Therefore total noise contribution is estimated from the system temperature: $T_{\rm sys} = T_{\rm sky} + T_{\rm receiver}$. The thermal noise component in observed visibility can be shown to be:

$$V_{\rm TN}(u,v) = \frac{T_{\rm sys}}{K\sqrt{Bt}} \tag{2.27}$$

where K is the antenna gain, B is the bandwidth and t is the integration time. Eq. (2.27) provides a relatively general estimate of interferometer sensitivity. In case of EoR experiments, interferometers probe different physical scales with a rate which depends on the antenna distribution, hence the sensitivity becomes a function of angular and frequency scales (Furlanetto et al. (2006)). McQuinn et al. (2006); Furlanetto & Lidz (2007) provide a detailed estimate of the sample variance and thermal errors on the HI power spectrum:

$$\delta P_{\rm HI}(\mathbf{k}_i) = P_{\rm HI}(\mathbf{k}_i) + \frac{T_{\rm sys}^2}{Bt}\frac{D^2\Delta D}{n(\mathbf{k}_\perp)}.\left(\frac{\lambda^2}{A_e}\right)^2 \tag{2.28}$$

where A_e is the area of a single antenna of the array, A_e/λ^2 correspond to the angular resolution in Fourier space. $\mathbf{k}_i$ is the wavenumber or mode being probed with integration time t. $\mathbf{k}_i$ can be decomposed into two components: those on the sky plane ($\mathbf{k}_\perp$) which is affected by the angular resolution of the interferometer, and those along line of sight $k_\parallel$ which depend on the frequency resolution. The factor $n(\mathbf{k}_\perp)$ consolidates the number of baselines observing the mode $\mathbf{k}_i$, normalized to the total number of baselines of the interferometer array. D denotes the comoving distance corresponding to the frequency of observation, ΔD represents the line of sight comoving depth corresponding to the bandwidth of observation.

Some important inferences can be drawn from Eq. (2.28). The error on $P_{\rm HI}(k)$ decreases with increasing integration duration t and collecting area A_e. The total collecting area can be increased by increasing number of elements in the array keeping individual A_e constant. This will increase $n(\mathbf{k}_\perp)$ although this strategy comes with cost of enhanced computing power. Another way to increase collecting area is by making each antenna larger keeping the total number fixed, which is not desirable since it reduces the total field of view. Also

by increasing bandwidth the sensitivity can be improved as enhanced bandwidth adds new modes along the line of sight.

2.4 Conclusions

In this chapter we have established the relation between the visibility measurements of interferometric arrays and EoR observables. Eq. (2.10) infers that the visibility correlation function is one manifestation of the HI power spectrum $P_{\rm HI}(k)$. In 'delay spectrum' approach there exists one to one relationship between observable parameters $(\mathbf{u}_\nu, \tau)$ and the Fourier space components of $P_{\rm HI}(k)$. The modes accessible by the interferometer can be estimated from Eq. (2.18). The lower limit of $k_\perp$ is given by the smallest baseline, whereas the maximum $k_\perp$ is estimated by the longest baseline. The lower and upper limit on $k_\parallel$ axis correspond to the total bandwidth and frequency resolution respectively. We also discussed the foreground contributions in 'delay space' approach. The foreground power can be isolated in a 'wedge' shaped region. The region beyond the 'wedge' (also called 'EoR window') can be used for $P_{\rm HI}(k)$ estimation. In next chapter we discuss the 'delay spectrum' approach in more detail with application to the real MWA tracking observation. We also discuss the impact of w-terms and 'distortions due to long tracking run' on the power spectrum estimator.

Chapter 3

Delay Spectrum wth Imaging Arrays

Different approaches have been discussed in literature to detect the HI signal in the presence of dominant foregrounds. They are all based on the expectation that foregrounds are smooth in frequency space as they arise from continuum emission, e.g. Synchrotron radiation, in both our Galaxy and extra-galactic sources. On the other hand the HI signal is expected to decorrelate strongly in the frequency space. It is conceivable that all these sources, both point and diffuse, can be subtracted from the images, leaving behind the HI signal and Gaussian noise, and LOFAR partly relies upon this technique (Chapman et al. (2012, 2013)). Another possible method is based on the isolation of foregrounds from the HI signal using power spectrum of the observed signal in conjugate space to the observed frequency (Morales & Hewitt (2004); Thyagarajan et al. (2013); Bowman et al. (2009); Parsons et al. (2012b)). Variants of this 'delay space' method are particularly relevant for interferometers such as MWA that have low angular resolution and have been used extensively for the analysis of PAPER data. PAPER relies upon redundant baseline to calibrate the interferometer but uses only East-West and near East-West baselines for power spectrum estimation (Parsons et al. (2012b), Parsons et al. (2014), Ali et al. (2015)).

Many research groups are currently developing pipelines to extract statistical information from radio interferometric data, with an aim to detect the HI signal from EoR. Jacobs et al. (2016) provide a comparison of the existing MWA EoR pipelines (Hazelton et al. (2016), Dillon et al. (2015), Trott et al. (2016)). These can be divided broadly in two categories: image based and visibility based pipelines. For foreground subtraction and imaging these

pipelines use both the following imaging algorithms: Real Time System (RTS; Mitchell et al. (2008), Ord et al. (2010)) and Fast Holographic Deconvolution (FHD, Sullivan et al. (2012)).

The image based pipelines (Jacobs et al. (2016), Hazelton et al. (2016)) use source catalog created through the deconvolution of the data which is subtracted to obtain a residual image cube. The Fourier transform of this image cube with some further processing yields the power spectra. On the other hand, the visibility based pipelines (Trott et al. (2016)) use the data in visibility domain for power spectra estimation, after the initial processing in the image domain for obtaining the foreground model. The detailed comparison of the outputs from all the methods described above is provided in Jacobs et al. (2016). Thyagarajan et al. (2015a) describe the impact of wide field of view in power spectra estimation.

In this chapter we propose a new method based on the 'delay space' approach, which is employed to isolate foregrounds, to extract the power spectrum of the HI signal in the presence of noise and foregrounds. Our method is based on modelling the HI signal taking into account the impact of the w-term and the change in intensity pattern during a tracking run. The information of the decorrelation of the HI signal is used as weights to cross-correlate the measured visibilities. The proposed method ('Delay Spectrum with Imaging Arrays (DSIA)') is a general method applicable for tracking with radio interferometers with wide primary beams and arbitrary array configuration (e.g. MWA, LOFAR) and can also be applied to interferometers with redundant baselines. We apply the proposed method to analyse 3 hours of MWA data on the EoR1 field and compare our results with noise and foreground simulations.

3.1 HI signal and w-term

From Eq. (2.16), we can gauge the impact of the w-term. This equation shows that the integral over τ and ν are either separable or trivial. The main effect of the w-term is to alter the integrals over angles which we study here.

For a given baseline $\mathbf{B}$: $w_\nu = \mathbf{B} \cdot \mathbf{s}_0 \nu / c$, where $\mathbf{s}_0$ is the phase center as any time. As a region is tracked, the w-term changes owing to the drift of the phase center. For a tracking

run, $\mathbf{u}_\nu^2 + w_\nu^2$ is left invariant at any frequency; this result simply follows from the fact the the baseline length is fixed.

After the inclusion of the w-term, the measured visibility for a given intensity distribution is given as:

$$\begin{aligned} V_\nu(\mathbf{u}_\nu, w_\nu) &= \int A_\nu(\vec{\theta}) \Delta I_\nu(\vec{\theta}) \\ \times \quad & \exp -i2\pi \left[u_\nu l + v_\nu m - w_\nu/2(l^2+m^2)\right] dl dm \end{aligned} \tag{3.1}$$

Here we have replaced $\vec{\theta}$ with its components (l, m) and also made the approximation: $\sqrt{1-l^2-m^2} - 1 \simeq -(l^2+m^2)/2$. Substituting Eq. (2.6) into Eq. (3.1) gives us,

$$\begin{aligned} V_\nu(\mathbf{u}_\nu, w_\nu) &= \bar{I}_\nu \int \frac{d^3k}{(2\pi)^3} \delta_{\rm HI}(\vec{k}) e^{ir_\nu k_\parallel} \int A_\nu(l,m) \\ &\times \exp\left[-2\pi i \left\{ \left(u_\nu - \frac{k_{\perp 1} r_\nu}{2\pi}\right) l + \left(v_\nu - \frac{k_{\perp 2} r_\nu}{2\pi}\right) m \right.\right. \\ &\left.\left. - \frac{w_\nu}{2}(l^2+m^2) \right\}\right] dl dm \end{aligned} \tag{3.2}$$

Each MWA tile being approximately a square aperture, the primary beam $A_\nu(l, m)$ can be written as:

$$A_\nu(l,m) = \frac{\sin(\pi L_x l)}{\pi L_x l} \frac{\sin(\pi L_y m)}{\pi L_y m} \tag{3.3}$$

Here L_x and L_y are dimensionless. They correspond to the ratio of the length of the tile along x- and y-axis to the wavelength. For central wavelength of the observation $L_x = L_y \simeq 2$. Eqs (3.1) and (3.3) show that integrals over l and m are separable and identical. These integrals cannot be done analytically but under certain approximations meaningful analytic expressions can be found. Let us define:

$$Q_\nu(k_{\perp 1}; u_\nu, w_\nu) = \int dl \exp\left[-2\pi i \left\{ \left(u_\nu - \frac{k_{\perp 1} r_\nu}{2\pi}\right) l - \frac{w_\nu}{2} l^2 \right\}\right] \frac{\sin(\pi L_x l)}{\pi L_x l} \tag{3.4}$$

$Q_\nu(k_{\perp 1}; u_\nu, w_\nu)$ is a function of $k_{\perp 1}$ and is parametrized by u_ν and w_ν. First we consider, $w = 0$. In this case, it can be shown that if the limits of the integral are allowed to go from minus infinity to plus infinity, we obtain,

$$\begin{aligned} Q_\nu(k_{\perp 1}; u_\nu, 0) &= \frac{1}{L_x} \text{ if } |(u_\nu - r_\nu k_{\perp 1}/(2\pi))|/L_x < 1/2 \\ &= 0 \text{ otherwise} \end{aligned} \tag{3.5}$$

We notice that the approximation used is good because the function has a compact support provided by the primary beam. As $L_x \simeq 1/\theta_0$ where θ_0 is the extent of the primary beam, this result means that, for a given u_ν, the wavenumbers that contribute to the integral are the ones that are bounded by the extent of the primary beam. This result is already implied by Eq. (2.16).

Eq. (3.4) cannot be analytically approximated so readily for non-zero w. We use the stationary phase approximation to analytically evaluate the integral. For this assumption to hold, the phase of the exponent should be much larger than the slow variation of the primary beam. This would be the case if wl^2 is large. In this approximation, we obtain:

$$\begin{aligned} Q_\nu(k_{\perp 1}; u_\nu, w_\nu) &= \sqrt{\frac{2i}{w}} \frac{\sin(\pi L_x(u_\nu - k_{\perp 1} r_\nu/(2\pi))/w_\nu)}{\pi L_x(u - k_{\perp 1} r_\nu/(2\pi))/w_\nu} \\ &\quad \times \exp\left[-i(u_\nu - k_{\perp 1} r_\nu/(2\pi))^2/(4\pi w_\nu)\right] \end{aligned} \tag{3.6}$$

The main impact of the inclusion of the w-term can be discerned from this expression. In the limit of large w, the impact of the w-term is to shrink the MWA beam and the primary beam tends to $1/\sqrt{w}$ (Cornwell et al. (2008)). [1] However, this also means that the spread of $k_{\perp 1}$ for which the integral is non-zero also increases, as seen in the terms involving the *sin* function. If the decrease of primary beam results in a loss of signal-to-noise, an increase in the correlation length $|\mathbf{u} - \mathbf{u}'|$ gains signal-to-noise. We can write visibility correlation for pairs of $\mathbf{u}, w$ and $\mathbf{u'}_\nu, w'_\nu$ as:

$$\begin{aligned} \langle V_\nu(\mathbf{u}_\nu, w_\nu) V^*_\nu(\mathbf{u'}_\nu, w'_\nu)\rangle &= \int \frac{d^3k}{2\pi^3} P_{\rm H1}(k) Q(k_{\perp 1}; u_\nu, w_\nu) \\ \times Q(k_{\perp 2}; v_\nu, w_\nu) Q(k_{\perp 1}; u'_\nu, w'_\nu) Q(k_{\perp 2}; u'_\nu, w'_\nu) & \end{aligned} \tag{3.7}$$

Eq. (3.7) can be computed numerically. In Figure 3.1, we show how the HI correlation function is affected in the presence of w-term. These expressions are also valid for diffuse foregrounds which have a different 2-dimensional power spectrum and frequency dependence. For optically thin diffuse foregrounds, the angular and frequency dependence is separable. As Eq. (3.7) can be used to compute the impact of w-term at any frequency, it can readily be generalized to study diffuse foregrounds.

[1] The impact of w-term can be more readily computed if the beam is Gaussian (e.g. Appendix B of Paul & Sethi et al. (2014)) In this case, the primary beam approaches $(1/\theta_0^2 + \pi w_\nu)^{-1/2}$ for non-zero w.

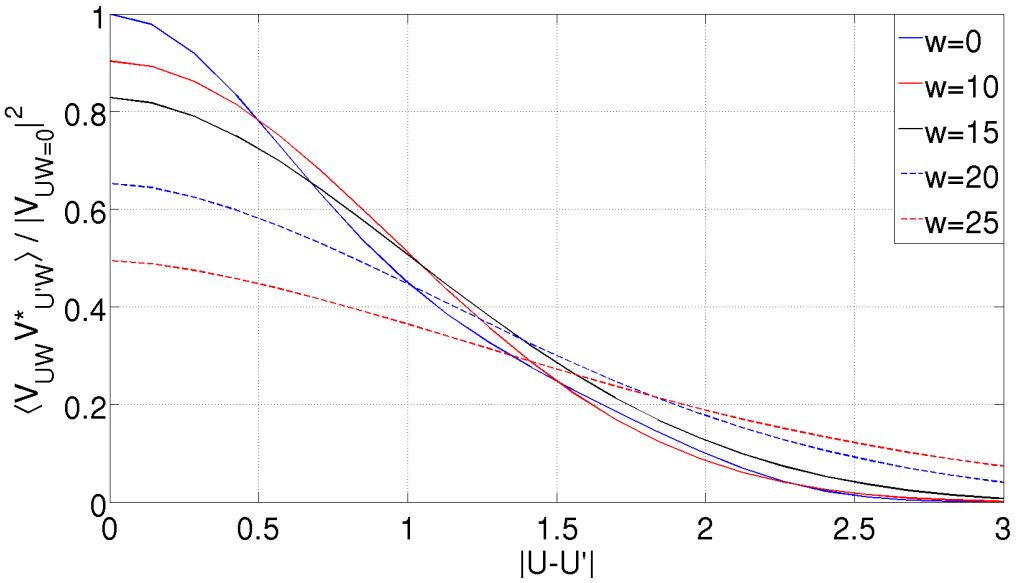

Figure 3.1: The HI signal is plotted as a function $|\mathbf{u} - \mathbf{u}'|$ for different values of w. The impact of w-term is to decrease the overall signal owing to shrinking of the primary beam and increase the correlation length $|\mathbf{u} - \mathbf{u}'|$.

3.1.1 Time dependent coordinate system and w-term

In a tracking interferometric observation, a phase center is tracked and snapshots are taken at regular intervals with short duration. Each of these snapshots can be imaged and the images added if the successive fields of view can be assumed to be coplanar. This approximation breaks down for wide field-of-view instruments such as MWA. One manifestation of the wide field-of-view is the w-term whose impact was studied in the previous sub-section. In this section we generalize the discussion of the last sub-section to take into account the time dependence of the non-coplanarity of the tracked region (Perley (1999)).

As the region is tracked, the relation between the image and astronomical coordinates changes which distorts the intensity pattern with respect to the phase center being tracked. It is best illustrated with a set of point sources. These sources appear to move with respect to the phase center (e.g. Fig. 19-9 in Perley (1999)). The distortion of the intensity pattern corresponds to non-uniform stretching and it increases for sources further away from the phase center. Thus this effect can not be corrected by a standard shift of coordinate. The

non-uniform stretching makes the situation complex, and the standard grid approach is difficult to implement in this case. For a set of point sources, the correction for this effect could be applied iteratively in the image plane (Chapter 19, Perley (1999)).

For a small field-of-view, this effect can be neglected and a unique coordinate system (e.g. time independent direction cosines $\{l, m\}$) can be used to relate the image coordinates with the sky intensity pattern for a long tracking run. However, it is not possible to define such a coordinate system when either the field of view is large or the tracking period is long.

Our aim here is not to correct for this effect but rather to estimate its impact on the correlation of visibilities at two different times during a tracking run: suppose we measure visibilities within a small cell in the u–v plane (the size of the cell will be discussed in a later section) centered around a baseline $\{u, v\}$ at $t = 0$. At a later time $t = t'$ another baseline might enter this cell. From the discussion in the previous subsection and Chapter 2, (e.g. Figure 3.1) the two visibilities are expected to correlate strongly with each other (even if the values of w differ significantly for these two sets this statement is generally true). However, visibilities measured at two different times do not correspond to the same intensity pattern. Our aim here is to estimate the level of de-correlation caused by the distortion of intensity pattern during a tracking run. We construct a time-dependent coordinate system which allows us to analyse this distortion of intensity pattern. We assess the impact of this effect when a region is tracked using the MWA primary beam. In particular, we consider this effect on the visibilities produced by the EoR HI signal.

We start by recalling the definition of direction cosines for a point on the sky whose coordinates, declination and hour angle $\{\delta, h\}$, are: written as (Christiansen & Hogbom (1969)):

$$l = \sin(h)\cos(\delta) \tag{3.8}$$

$$m = \cos(\delta)\cos(h)\sin(\phi) - \sin(\delta)\cos(\phi) \tag{3.9}$$

$$n = \cos(\delta)\cos(h)\cos(\phi) + \sin(\delta)\sin(\phi) \tag{3.10}$$

It can be shown that $n = \sqrt{1 - l^2 - m^2}$. The phase center is always defined as $l = 0$, $m = 0$, $n = 1$; for the coordinates defined above it is: $h = 0$ and $\delta = \phi$.

As a phase center is tracked owing to the rotation of the Earth, δ remains fixed but the

hour angle changes. For a wide field of view, this can result in distortion of the intensity pattern of the sky. To take into account this effect, we can define a time-dependent coordinate system:

$$l(\delta h) = \sin(h + \delta h)\cos(\delta) - \sin(h_0 + \delta h)\cos(\delta_0) \tag{3.11}$$

Here h_0 and δ_0 define the phase center for $\delta h = 0$; δh defines the flow of time. m can be similarly defined and n can be computed from l and m. This definition gives a time dependent coordinate system where the coordinates are always defined with respect to the phase center. It is easy to verify that for small field of view and for small tracking times, which corresponds to cases when higher order terms in h, δh and δ can be dropped, l is independent of time which means that the distance of a point from the phase center is left invariant under tracking. In such cases, the intensity pattern on the sky corresponds to the unique intensity pattern defined by sky coordinates δ and h and remains unchanged as the phase center is tracked.

However, when this approximation breaks down, l becomes a function of time and it is impossible to define a unique relation between direction cosines and sky coordinates. This means that any quantities defined with respect sky coordinate (e.g. intensity pattern) become time dependent. The visibility for the HI signal is given by:

$$\begin{aligned} V_\nu(\mathbf{u}_\nu, w_\nu, \delta h) &= \bar{I}_\nu \int \frac{d^3k}{(2\pi)^3}\delta_{\rm HI}(\vec{k})e^{ir_\nu k_\parallel}\int A_\nu(l,m) \\ &\times \exp\Bigg[-2\pi i\Bigg\{\left(u_\nu - \frac{k_{\perp 1}r_\nu}{2\pi}\right)l + \left(v_\nu - \frac{k_{\perp 2}r_\nu}{2\pi}\right)m \\ &-\frac{w_\nu}{2}(l^2+m^2)\Bigg\}\Bigg]\sin\delta d\delta dh \end{aligned} \tag{3.12}$$

The direction cosines l and m are now functions of time. The angular integral is carried out over δ and h. Unlike the earlier case (fixed grid) this is not a product of two one-dimensional integrals. The correlation of the visibilities $V_\nu(\mathbf{u}_\nu, w_\nu, \delta h)$ can be computed using the same methods as outlined in the previous sections.

In Figure 3.2 we show the results when the effect of the time dependent coordinate system ('moving grid') is included. The initial phase center ($\delta h = 0$) is chosen to be $h = 0$ and $\delta = \phi$. The results are shown for two different values of δh and a range of w values. We only show the auto-correlation function for a given value of δh. But the results shown in

Figure 3.2 can be used to assess the cross-correlation of visibilities measured at two different times. For our case the value of this cross-correlation lies between the auto-correlations of visibilities measured at the same time. The moving grid doesn't introduce another scale in the problem and the results in this case are not very different from the case for a fixed grid. In both cases the dominant correlations occur for $\mathbf{u} - \mathbf{u}' < 1.5$.

Figures 3.1 and 3.2 are based on MWA primary beam. However, it is possible to glean generic information applicable for other primary beams from them. First, the decorrelation length $|\mathbf{u}-\mathbf{u}'|$ scales as the inverse of the primary beam (e.g. Paul & Sethi et al. (2014)). So for a smaller beam, the decorrelation seen in the Figures as a function of $|\mathbf{u} - \mathbf{u}'|$ would be shallower. The impact of the w-term for a different primary beam can be partially gauged from Eq. (3.6), which is valid for large values of w. In this limit, the primary beam tends to $1/\sqrt{w}$, irrespective of the primary beam of the telescope. It is difficult to analytically estimate the impact of the w-term when this limit does not hold. But it can be shown that the impact of w-term diminishes for a smaller primary beam, e.g. a Gaussian beam for which the primary beam tends to $(1/\theta_0^2 + \pi w_\nu)^{-1/2}$ for non-zero w (e.g. Paul & Sethi et al. (2014)). As noted above, the distortion of intensity pattern during a tracking run is a wide field effect. For a smaller primary beam, the level of decorrelation seen in Figure 3.2 would be smaller but it is difficult to analytically estimate it.

3.1.2 Weights for cross-correlation

Eq. (3.12) can be used to compute the counterpart of Eq. (2.16) which takes into account the impact of non-zero w-term and the distortion of intensity pattern. We compute this expression for the visibility correlation in delay space numerically. In this formulation, the measured visibility is a function of five parameters: $\tau, \mathbf{u}, w, t$. Here, as noted above, $\mathbf{u}$ and w are the values of these variables at a fixed frequency which we choose to be $\nu_0 = 154\,\mathrm{MHz}$.

We define the weight on a given cross-correlation as:

$$\mathcal{W}(\mathbf{u}, w, t; \mathbf{u}', w', t') = \frac{\langle V_\tau(\mathbf{u}, w, t) V_\tau^*(\mathbf{u}', w', t')\rangle}{\langle V_\tau(\mathbf{u}, 0, t) V_\tau^*(\mathbf{u}', 0, t')\rangle} \tag{3.13}$$

The weights are defined with respect to the HI cross-correlation computed in Eq. (2.16) for $\mathbf{u} = \mathbf{u}'$, $w = w' = 0$, $t = t'$ and $\tau = \tau'$. We only consider the case $\tau' = \tau$ for the computation of weights.

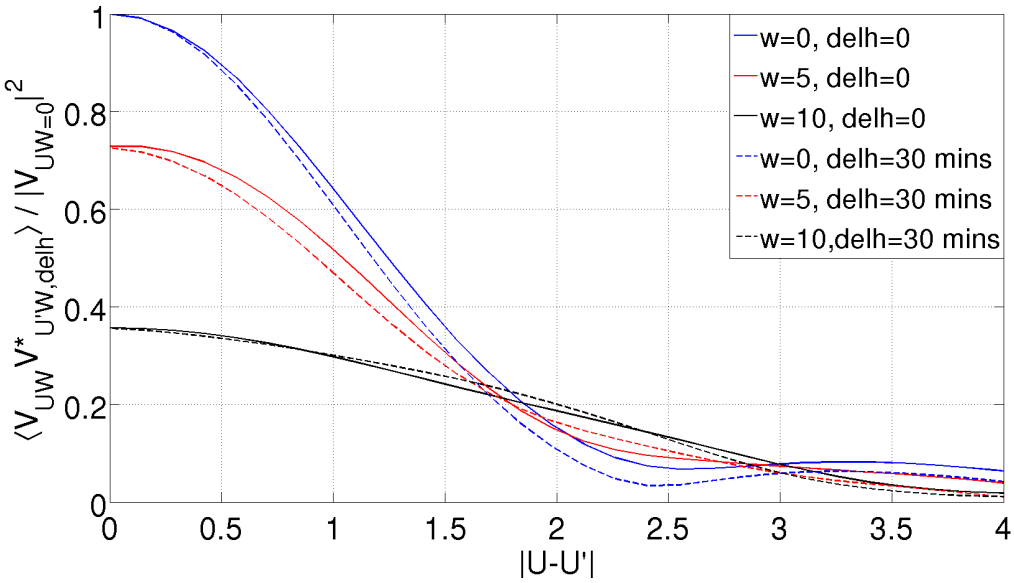

Figure 3.2: The HI signal is plotted as a function $|\mathbf{u} - \mathbf{u}'|$ for different values of w and δh. The initial phase center is chosen to be $h = 0$ and $\delta = \phi$.

Using Eq. (3.13) allows one to recover the HI power spectrum for a fixed wave number k from visibility cross-correlations.

3.2 Analysis of MWA data

To minimize the effect of Galactic synchrotron emission, the MWA EoR community has chosen three fields on the sky away from the Galactic plane. These fields have been named as EoR0, EoR1 and EoR2 and are shown in Figure 3.3. In this chapter we present 3 hours of tracking analysis of the EoR1 field centered at RA = 4h, Dec = $-27°$. In this and the next section, we discuss in detail our method of MWA data analysis and power spectrum estimation from the data.

We summarize below the major ingredients of the method and then describe each of the step in detail in subsequent sections:

1. For initial processing of the data we use CASA (Common Astronomical Software Applications). CASA (McMullin et al. (2007)) is used to calibrate raw visibility measurements. This is followed by the creation of a model sky image from clean components.

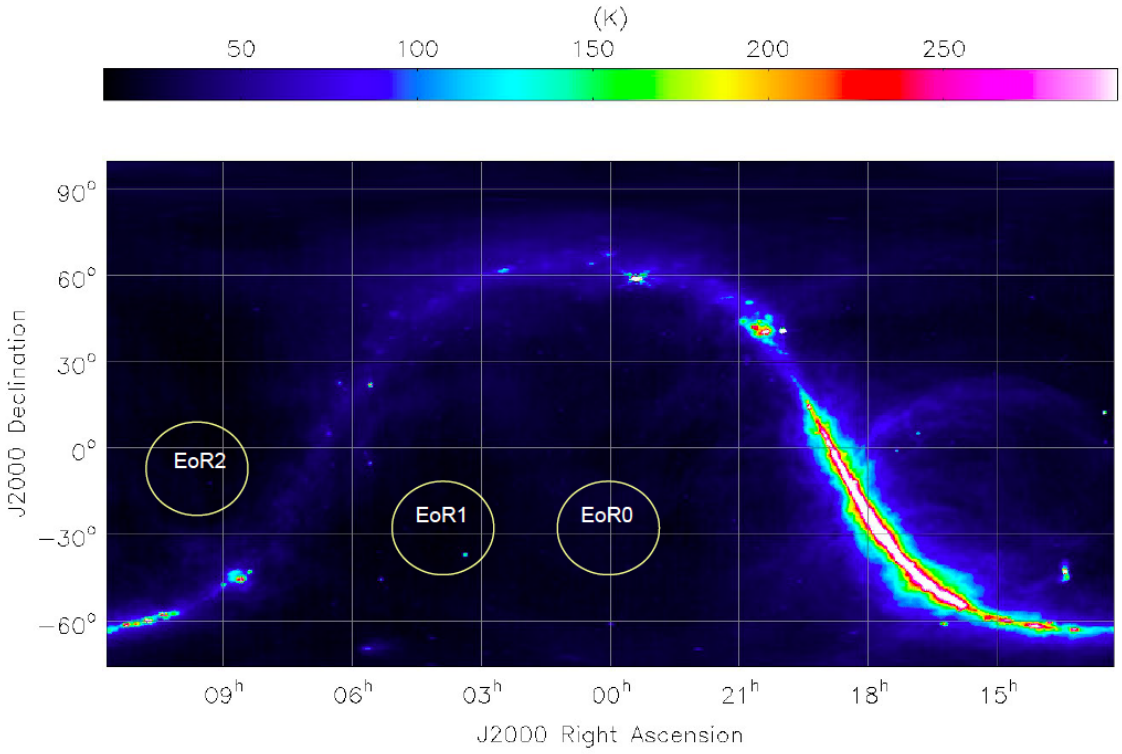

Figure 3.3: EoR fields are shown on the Galactic map at 408 MHz (Haslam et al (1982)). Three fields, away from the galactic plane, have been identified for the MWA reionization study. These are EoR0, EoR1 & EoR2 respectively as shown in circles. In this work we focus on the EoR1 field centered at RA = 4h, Dec = $-27°$.

This model is then substracted in the visibility domain to obtain residual visibilities. We use both the calibrated and residual visibilities for computing the power spectrum.

2. Each visibility is then Fourier transformed in frequency space (Eq. (3.14)). This process is needed for isolation of foregrounds in the $k_\perp$–$k_\parallel$ plane. We note the our method utilizes both the substraction of foregrounds and their isolation. But it does not employ an external point source catalog.

3. The procedure outlined above yields complex visibilities as a function of five variables: $V_\tau(u, v, w, t)$. For computing the power spectrum we cross-correlate these visibilities for $t' \neq t$ to remove the noise bias. To weigh each cross-correlation we assume that there exist regions in $k_\perp$–$k_\parallel$ plane which are dominated by only noise and the HI signal; we attempt to justify this assumption using simulations. This allows us to compute a weight for each cross-correlation based on the expected HI signal. For computing these weights we take into account the impact of w-term and the distortion of intensity pattern in a tracking scan. The relevant method is elaborated in detail in sections 3.1, 3.1.1, and 3.1.2 and summarized in section 3.3.

4. In section 3.3.1, we describe the power spectrum estimator, taking into account weights given by the expected HI signal, in 3-, 2- and 1-dimension. We also discuss our method to compute the errors on the estimated power spectrum.

3.2.1 CASA processing

MWA data were collected at 2-minute intervals with a time resolution of 0.5 seconds and frequency resolution of 40 kHz. The central frequency of these observations is 154.24 MHz. For preprocessing we have used the Cotter pipeline (Offringa et al. (2015)) to average to 10 seconds of integration; we have not performed any averaging over the frequency channels. Cotter also uses the in-built AOFlagger to flag and remove radio frequency interference. The edge channels of each coarse band are flagged with Cotter due to aliasing effects. After this preprocessing the Cotter pipeline delivers the data in the CASA readable 'Measurement set (ms)' format for further processing.

Once the 'ms' files are produced for each 2-minute data set, we process each of these

2-minute data in CASA to produce an image. The Hydra A source is used to calculate the bandpass solutions which are applied to the uncalibrated data. We next construct a sky model from these data so that we could subtract it to obtain the residual visibility. After the bandpass calibration the first round of 'clean' is applied on each 2-minute data set. The multi-scale multi-frequency synthesis algorithm (Rau & Cornwell (2011)) has been used for imaging. We have created images of size 3072 x 3072 pixels with 1 arc-minute cell size using the Cotton-Schwab CLEAN (Schwab (1984)) with uniform weighting scheme. After the first round of clean we have performed self calibration (both phase and amplitude+phase) and apply the clean loop until the RMS value of the residual image converges. The threshold limits for the clean steps were chosen to be 5 sigma. The W-projection algorithm (Cornwell et al. (2008)) was also used to correct for the errors arising due to non-coplanarity of baselines. Once we obtain the best model of the sky for each 2 minute observation, the model visibilities are then subtracted from the calibrated data using the UVSUB algorithm in CASA to obtain the residual data. This process is followed for both XX & YY polarizations separately.

A flow chart of the data pipeline is shown in Figure 3.4. In Fig. 3.5 and 3.6 we present a sample image of 2 minute deconvolution.

As noted above we process the data for only 2 minutes to ensure the primary beam doesn't substantially change during the run. For a 2-minute scan we obtain an RMS of nearly 40 mJy/beam.

The residual visibility $V_\nu(u_\nu, v_\nu, w_\nu, t)$ is a function of five variables. We compute the discrete Fourier transform of the residual visibilities in the frequency space weighted by the Blackman-Nuttall (Nuttall (1981)) window $W_{\rm BN}$ to suppress leakage into the EoR window (Thyagarajan et al. (2013, 2016)):

$$V_\tau(u, v, w, t) = \sum \Delta \exp(i2\pi\nu\tau) V_\nu(u_\nu, v_\nu, w_\nu, t) W_{\rm BN} \tag{3.14}$$

Notice that in Eq. (3.14) the frequency dependence of the baseline vector $\mathbf{b}_\nu = \{u_\nu, v_\nu, w_\nu\}$ is integrated over. Therefore, the labels $\{u, v, w\}$ on the LHS of Eq. (3.14) need further explanation. As noted above (the discussion following Eq. (2.13)) they can be chosen to denote a given baseline vector at a fixed frequency, ν_0. We choose this frequency to be the central frequency of the band $\nu_0 = 154\,\mathrm{MHz}$. Parsons et al. (2012a,b) provide detail implications of the frequency dependence of the baseline vector. Here $\Delta = 40\,\mathrm{kHz}$ and

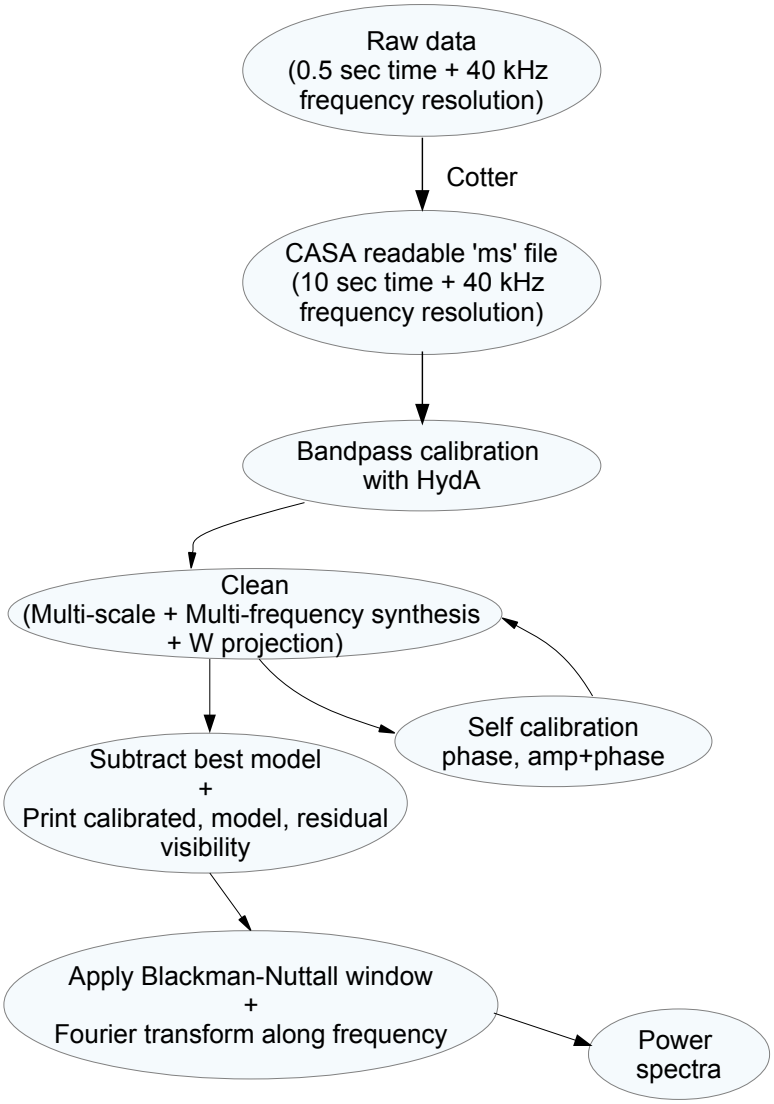

Figure 3.4: A schematic of the power spectra pipeline is shown.

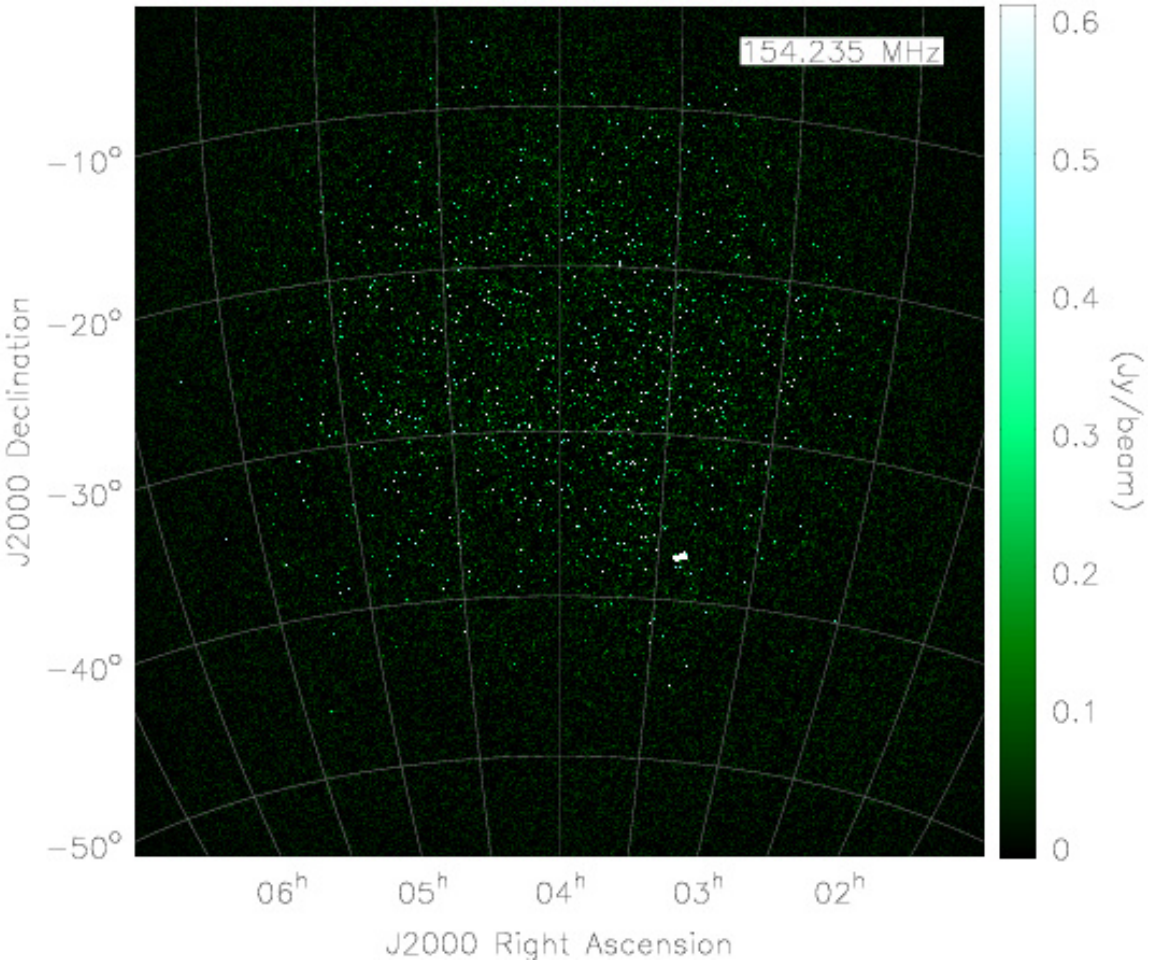

Figure 3.5: The image of EoR1 field at 154.24 MHz.

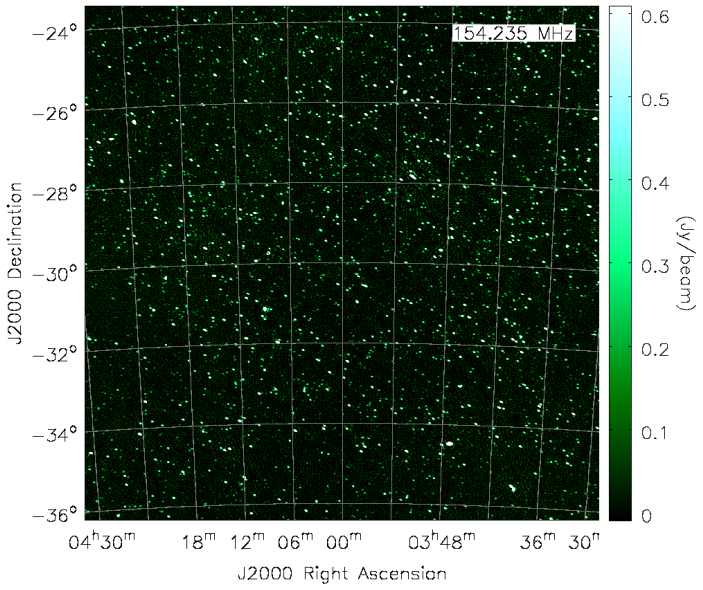

(a)

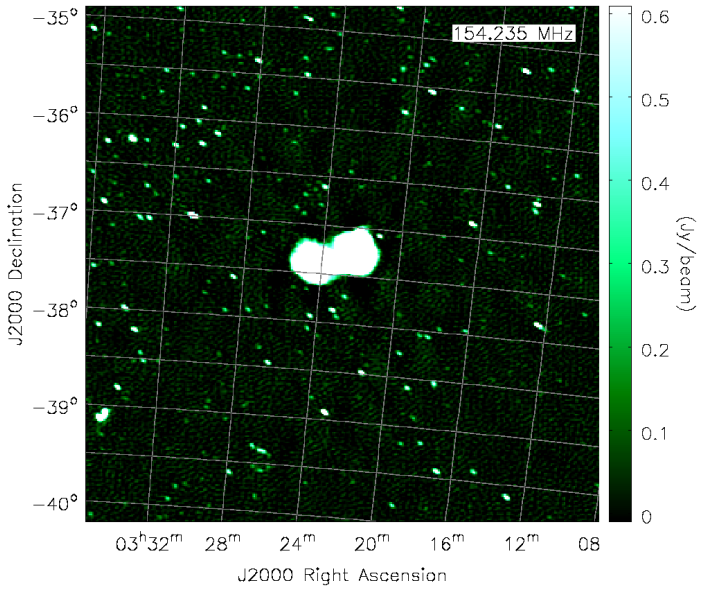

(b)

Figure 3.6: The top and bottom panels display two regions from the image in Fig. (3.5). The bottom panel zooms the region containing the Fornax A.

256 channels are used for our study, which correspond to total bandwidth 10.24 MHz in the frequency range 149.09 MHz to 159.34 MHz.

3.3 Power spectrum

The visibilities (Eq. 3.14) are cross-correlated with weights determined from the HI signal (section 3.1.2) to estimate the power spectrum. For each pair of parameters, e.g. $\{u, u'\}$, the weights are generally different. It is computationally prohibitive to deal with weights for all cross-correlations. We make several simplifying assumptions to make the problem tractable based on the properties of the HI signal. In sections 2.1, 3.1, and 3.1.1 we discuss in detail the HI signal and how it is affected by the inclusion of the w-term and the additional complication arising from distortion of the field of view as a region is tracked for MWA.

We summarize the main results of these sections as applied to the data:

1. In section 2.1 the HI signal and its correlations are discussed in detail. Eq. (2.17) shows that correlations in sky plane are nearly independent of correlations along the line of sight. This allows us to compute weights for correlations in the plane of the sky independent of the third axis. Eq. (2.17) allows us to derive a relation between the measured correlation and the inferred HI power spectrum (Eq. 2.19). Eq. (2.19) defines the scale of cross-correlation weights. The weight function $\mathcal{W}(u, v, w, t; u', v', w', t')$ is unity when $\mathbf{u} = \mathbf{u}'$, $w = w' = 0$ and $t \simeq t'$. Eq. (2.19) refers to this case.

2. In section 3.1, the impact of w-term on the HI signal is computed. Eq. (3.6) and Figure 3.1 capture the effect of non-zero w on HI correlations. The w-term diminishes the signal by shrinking the effective primary beam and increase the correlation length scale $|\mathbf{u} - \mathbf{u}'|$. We use the analytic expression based on Eq. (3.6) for computing weights for $w > 30$.

3. In section 3.1.1, we attempt to assess the impact of time-dependent distortion of intensity pattern in a tracking run for MWA. Figure 3.2 shows the combined effect of moving grid and w-term. The distortion of intensity pattern generally acts to enhance decorrelation but is found to be not significant and doesn't alter the main features of

the signal. For our computation, we only update the weights after every 10 minutes to account for this effect.

3.3.1 Power spectrum estimator

As shown above each correlation receives a different weight depending on the values of $\{u, v, w, t\}$ of the baselines being correlated. As noted above, we define the weights $\mathcal{W}$ such that they approach unity when $u = u'$, $v = v'$, $w = w' = 0$ and $t \simeq t'$ such that the effect of the moving grid is not important ($t \neq t'$ for all correlations to remove noise bias).

The HI power spectrum is a function of $k = \sqrt{\mathbf{k}_\perp^2 + k_\parallel^2}$; Eq. (2.18) gives the relation between the Fourier components of the HI signal and $\{\mathbf{u}, \tau\}$. All cross correlations for which the wave vector lies in some range k and $k + dk$ can be used to construct the unbiased HI signal: $1/N \sum V_\tau(u, v, w, t) V_{\tau'}(u', v', w', t')/\mathcal{W}$; here N is the number of all pairs for which k lies in the range specified above. However, this estimator, though unbiased for the HI signal, could be dominated by small values of weights $\mathcal{W}$, which doesn't make it the lowest noise (or optimal) estimator.

As the observed signal is dominated by noise, we consider an optimal estimator for our study:

$$\begin{aligned}\hat{P}_\tau(u, v) = & \frac{1}{\sum_{u',v',w,w',t,t'} \mathcal{W}^2(u, v, w, t, u', v', w', t')} \\ & \times \sum_{u',v',w,w',t,t'} \Big\{ V_\tau(u, v, w, t) V_\tau(u', v', w', t') \\ & \times \mathcal{W}(u, v, w, t, u', v', w', t') \Big\} \end{aligned} \tag{3.15}$$

To avoid noise bias, $t \neq t'$ for all cross-correlation. For a given $\{u, v, \tau\}$, Eq. (3.15) allows us to compute the power spectrum by optimally weighing over all the cross correlations. However, as Figures 3.1 and 3.2 show the correlations fall substantially for $\mathbf{u} - \mathbf{u}' \geq 1.5$ (see also Paul & Sethi et al. (2014) and references therein). This motivates us to pixelize the **u**-plane and consider only those visibility pairs for which the correlations are significant. We consider cells of different sizes and present results here for $\Delta u = \Delta v = 0.5$. The number of visibility measurements in a cell vary depending on the (u,v) values. The shortest baselines have higher population as expected for MWA. For 3 hours of analysis and $u, v < 50$, the

number of visibilities in a cell lie in the range $\sim$ 1000–3500 where each visibility has a time resolution of $\Delta t = 10$ sec. All the cross-correlation within a cell are computed using Eq. (3.15).

For averaging over different cells, each cell is assigned an average weight corresponding to the RMS of the power spectrum for a cell, σ_p. These weights are then used for optimally averaging the power spectrum (Eq. (3.15)) over other cells (For details see section 3.3.2). Note that this procedure allows us to separate large correlations of the HI signal, the ones for which $\mathcal{W}$ is close to unity, from the ones which are expected to be incoherent because $\mathcal{W}$ is small.

The schematic of the two processes—the computation of power spectrum in 3- and 2-dimensions—is displayed in figure (3.7): the top panel delineates the process of computing cross-correlations within each cell and the bottom panel depicts how azimuthal average for a fixed baseline length $\sqrt{u^2+v^2}$ is computed. For MWA data, $k_\parallel \gg \mathbf{k}_\perp$, which means the value of k is dominated by the value of $k_\parallel$. This suggests the following method for computing the 1-dimensional power spectrum, which we adopt: all the cells for a given τ are optimally averaged using the method described above. This procedure yields a complex number. In the Figures that display 2- and 1-d power spectra we plot the absolute value of the estimated power spectrum.

The error on power spectrum in 1-dimension is computed by first estimating the RMS for each cell, σ_p. σ_p are then used as weights for optimal averaging over all the cells for a fixed τ. The resultant RMS after averaging over the cells approaches $\sigma_{\rm fin} \simeq (1/\sum \sigma_p^2)^{-1/2}$ if the power spectrum across cells is uncorrelated. This holds for noise but, as noted above, is an approximation for the HI signal. We expect this assumption to be valid in our case as the observed signal is dominated by noise (for detailed explanation see section 3.3.2).

3.3.2 Power spectrum estimation

As discussed in Section 3.3.1, the power spectrum from the data is computed in two stages. First the power spectrum and its RMS is computed for a single pixel in which the HI signal is expected to be near coherent and then an average is obtained across pixels assuming the HI signal to be incoherent for different pixels (Figure 3.7).

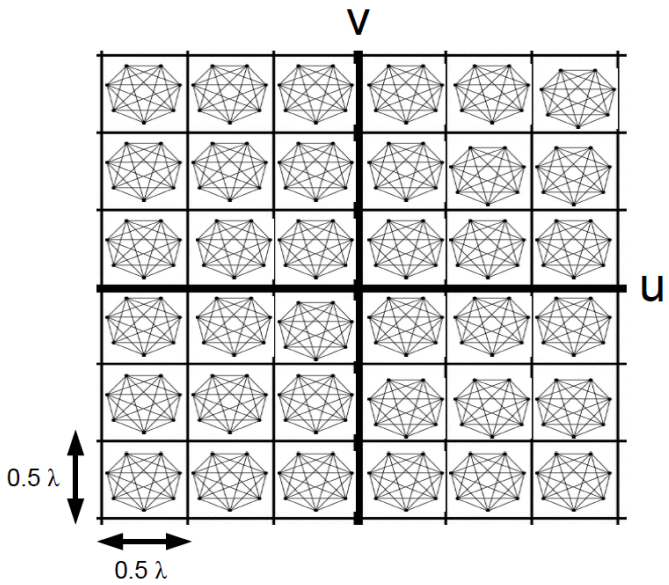

(a)

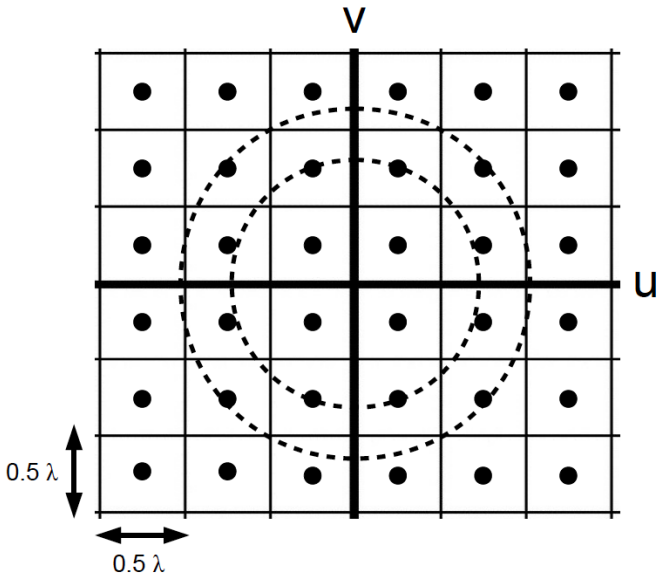

(b)

Figure 3.7: (a)This shows the population of visibilities within different uv bins for each τ. The small dots denote visibilities due to individual baselines. These are cross-correlated with each other within a given uv bin. (b) The black dots within a bin are the power value at each bin. An optimal azimuthal average, based on weights of each pixel, is done to collapse the uv axes into a single axis of baseline length.

As noted in the text, the HI signal can be recovered from a visibility cross-correlation by inverse weighing with $\mathcal{W}$. We denote such a cross correlation: $\hat{S} \equiv VV/\mathcal{W}$; $\hat{S}$ is generally a complex number. For optimal averaging to get the lowest noise estimator, one needs to sum over these cross-correlations by inverse weighing with the square of the RMS of each cross-correlation σ_i. For pure noise, $\sigma_i \propto 1/\mathcal{W}$ and one can obtain Eq. (3.15). Notice that this estimator is invariant under an overall scaling of σ_i. The error on power spectrum for each pixel σ_p is: $\sigma_p^2 = \langle \hat{S}^2 \rangle - \langle \hat{S} \rangle^2$, where the average is obtained optimally from the data for all the cross-correlations. It can be shown that if each cross-correlation is assumed to be uncorrelated, as would be the case for pure noise, $\sigma_p \simeq (1/\sum \sigma_i^2)^{-1/2}$. Notice that if the RMS for all the cross-correlations is the same, as would be the case if all measurements are equally weighted, then this expression reduces to $\sigma_p = \sigma_i/\sqrt{N_c}$, where N_c is the number of all the cross-correlations within a pixel.

This procedure yields an estimate of the power spectrum (Eq. (3.15)) and its error σ_p for each pixel.

For averaging over pixels, we repeat the procedure described above by taking the estimated power spectrum for a pixel as the signal and σ_p as the weights. This allows us to estimate 2- and 1-dimensional power spectrum and its RMS. For pure noise, the final error on the power spectrum is expected to approach: $\sigma_{\rm fin} = \sigma_p/\sqrt{N}$, where N is the number of pixels used for obtaining the average.

We briefly discuss some shortfalls of such a procedure. First, we do not construct the covariance matrix of the power spectrum estimator. We only estimate its diagonal terms, σ_p^2 and $\sigma_{\rm fin}^2$. This means that we are not able to assess the extent of cross-correlation between two neighbouring bins in Figure 3.10. Such cross-correlation might contain important information about systematic errors, foreground leakage, and HI signal and noise cross correlation.

Second, we do not include the HI signal in our estimation procedure. This is justified for the present work as the observed signal is clearly dominated by noise and foreground residuals (Figure 3.10). We briefly assess the impact of the HI signal for computing the error on the power spectrum.

We assume the following estimator for computing the power spectrum for a pixel and

consider the contribution of only the HI signal:

$$\hat{S} = \frac{1}{N_c} \sum_{ij} \frac{V_i V_j}{\mathcal{W}_{ij}} \tag{3.16}$$

As noted above, this estimator allows us to recover the HI signal. The subscripts ij correspond to a pair for visibilities and the sum is carried over all the cross-correlations. After further computation, we obtain the error on the signal:

$$\Delta\hat{S}^2 = \frac{\hat{S}^2}{N_c^2} \sum_{kl} \sum_{ij} \left[\frac{\mathcal{W}_{ik}\mathcal{W}_{jl} + \mathcal{W}_{il}\mathcal{W}_{jk}}{\mathcal{W}_{ij}\mathcal{W}_{kl}} \right] \tag{3.17}$$

If all the weights are unity this reduces to the usual cosmic variance expression: $\Delta\hat{S} = \sqrt{2}\hat{S}$. Even though this term is negligible for our purposes, this would need to be included for longer integration times.

3.4 Results

In Figures 3.8 and 3.9, the power spectra computed from 3 hours of data are shown in the $k_\perp$–$k_\parallel$ plane. The power spectra for both XX and YY polarization are shown for calibrated and residual visibilities. We first discuss discernible features in the power spectra:

1. In Fourier space the foreground contributions occupy a wedge shaped region (also called 'foreground wedge') owing to the smooth spectral characteristics of foreground sources (Datta et al. (2010); Vedantham et al. (2012); Parsons et al. (2012b); Liu et al. (2014); Dillon et al. (2014); Thyagarajan et al. (2013, 2015a)). The region beyond the foreground wedge is expected to be free from the foreground contamination and dominated by thermal noise and expected HI signal. This foreground isolation approach is particularly useful for the MWA as it has low angular resolution. The strongest HI signals lie in the shortest baselines (low $k_\perp$ values) and it decreases rapidly with increasing $k_\perp$ values.

   Figures 3.8 and 3.9 display the dirty (calibrated with no foreground subtraction) and the residual (clean components subtracted) power spectra, respectively. They bear out the assumption that foregrounds have smooth spectral characteristics as they are seen to form the 'foreground wedge', this separation is in good agreement with

the expectation from foreground simulations (Figure 3.11). The first few $k_{\parallel}$ modes exhibit maximum foreground contributions, the $k_{\parallel} = 0$ mode being the strongest. The amplitude at this mode is roughly 10^{14}–10^{15} mk^2 (Mpc/h)^3 which is in good agreement with the results of other MWA EoR pipelines (Jacobs et al. (2016)). A clear decrement in power in the 'foreground wedge' is visible in residual power spectra as compared to the dirty one.

2. As described in the previous section, MWA has missing channels on either side of coarse bands of width 1.28 MHz. This leads to a periodicity of missing data across the frequency axis in visibility, the effect of which is reflected in the Fourier-transformed power spectra as the horizontal bright lines at fixed $k_{\parallel}$.

Figure 3.10 shows the 1-dimensional power spectra; the 1-dimensional power spectrum is obtained from regions that exclude the foreground wedge and bright coarse bands in Figures 3.8 and 3.9. For computing the 1-d power spectrum, the foreground wedge and the bright coarse horizontal bands of the 2-d power spectrum (Figure **??**) are rejected. More specifically, the channels corresponding to $k_{\parallel} \leq 0.14hMpc^{-1}$ and $k_{\perp} > 0.1hMpc^{-1}$ are not considered. For each coarse band, the central brightest channel along with two channels on either side are excluded. The remaining contiguous regions are used in estimation of the 1-d power spectrum. For instance, for a given $k_{\parallel}$ that meets the criterion outlined above, all the cells that correspond to $k_{\perp} < 0.1hMpc^{-1}$ are used for the computation of 1-d power spectrum. The error on the binned power spectra are computed using a scheme outlined in Appendix 3.3.2.

The 2-d power spectra obtained from data (Figure **??**) can be compared with Figure 3.11 that shows the expected power spectrum based on simulations of foregrounds and noise. In particular, this comparison allows us to assess the structure of coarse channels and the foreground wedge. It also indicates the range of scales of the 2-d power spectrum. However, Figure 3.11 is based on a single realization of noise and a model of foregrounds based on random distribution of point sources, and therefore a more detailed comparison between the data and simulations is not possible. We shall return to this detailed comparison in future work.

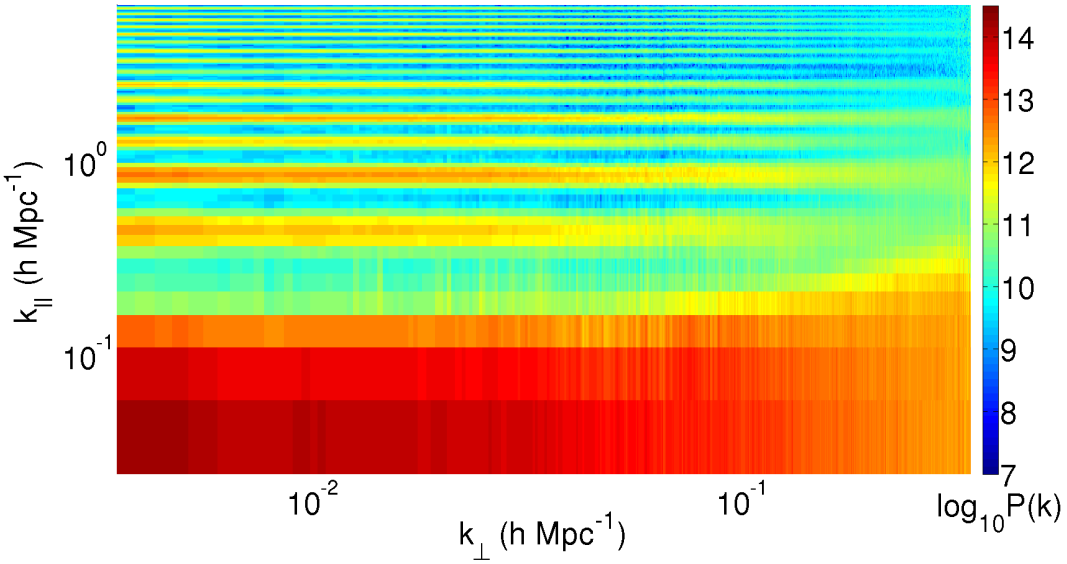

(a) dirty XX

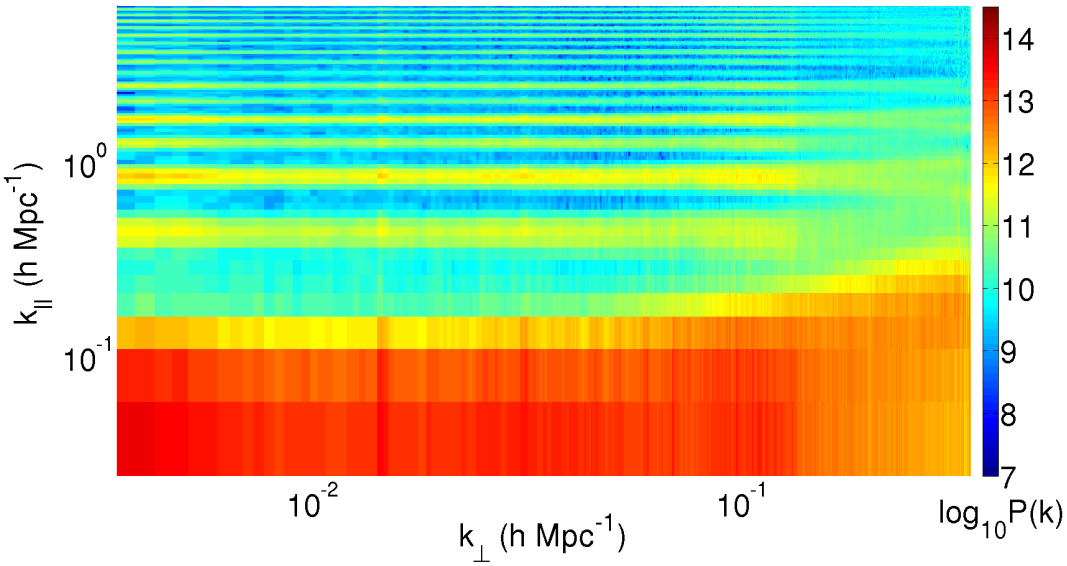

(b) residual XX

Figure 3.8: Two-dimensional power spectra for 3 hrs of data on the EoR1 field for XX polarization. The power is plotted as $log_{10}P$ where P is in units mK^2(Mpc/h)^3.

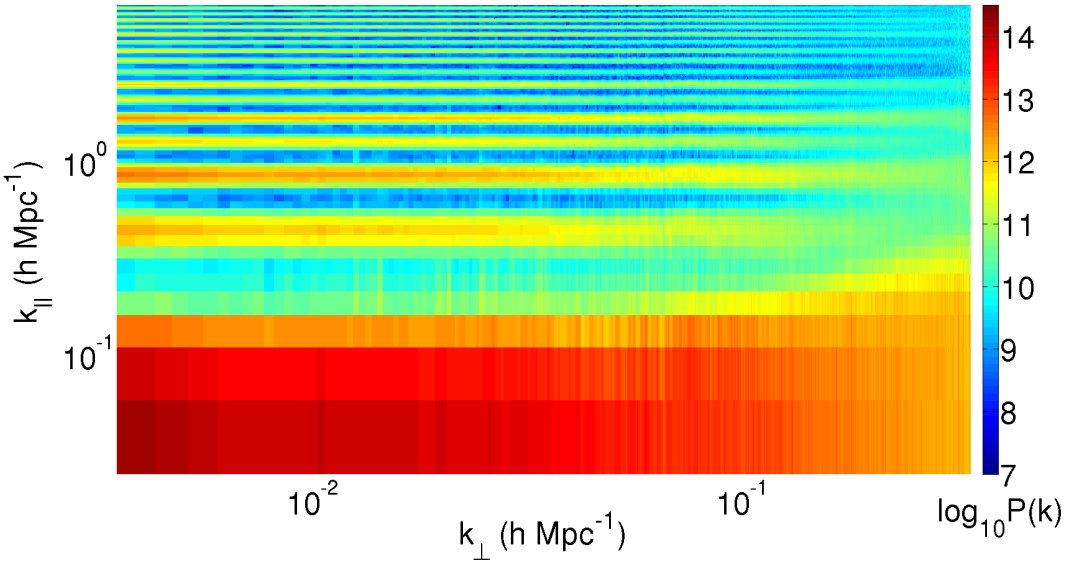

(a) residual XX

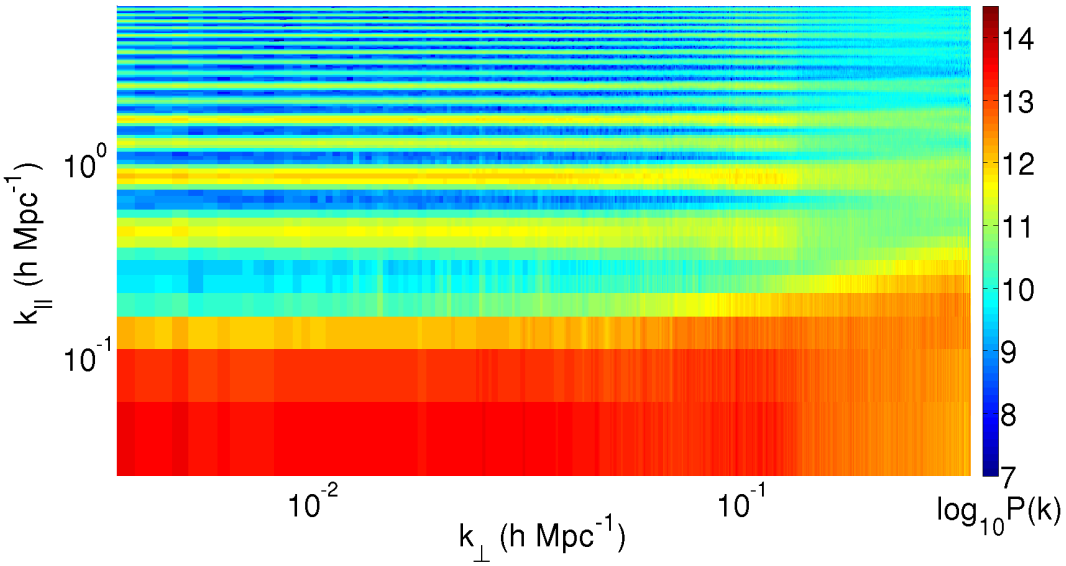

(b) residual YY

Figure 3.9: Two-dimensional power spectra for 3 hrs of data on the EoR1 field for YY polarization. The power is plotted as $log_{10}P$ where P is in units mK^2(Mpc/h)^3.

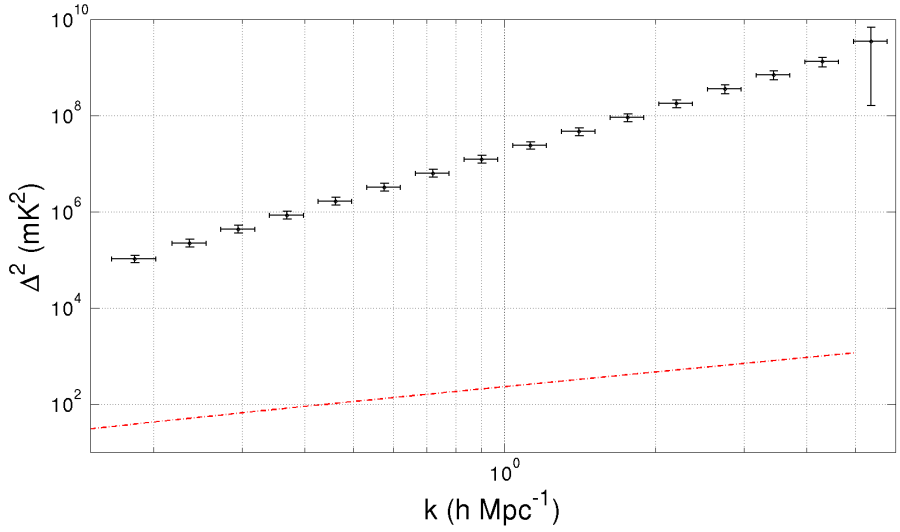

(a) XX

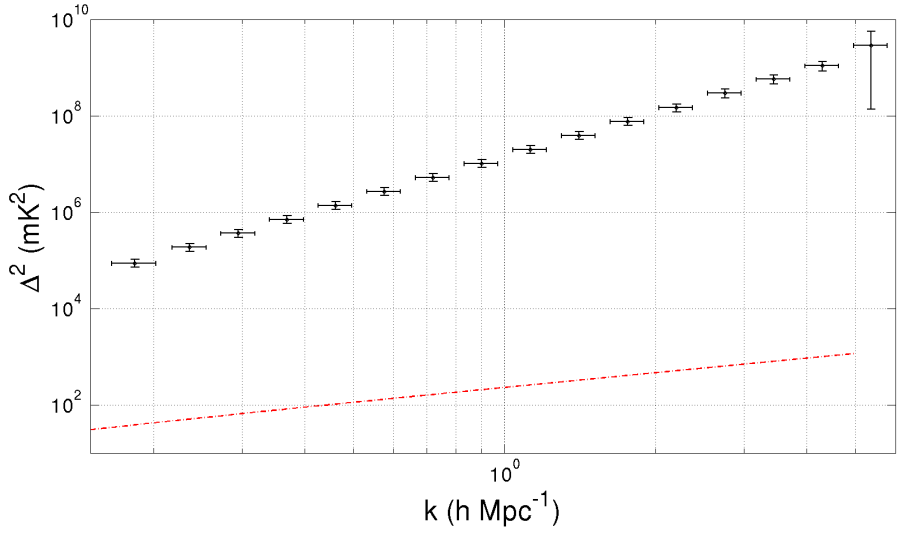

(b) YY

Figure 3.10: One dimensional power spectra ($\Delta^2 = k^3P(k)/(2\pi^2)$ in units $(\mathrm{mK})^2$) for the XX (Left panel) and YY (Right panel) polarization are shown along with the errors for each band. The dot-dashed (red) curves show the expected HI signal (Furlanetto et al. (2006)).

3.5 Thermal noise

Thermal noise is independent of the baseline and depends on three parameters: system temperature, integration time and the channel width. The RMS of thermal noise associated with a visibility measurement for channel width $\Delta\nu$ and integration time Δt is:

$$\sigma(\nu) = \frac{T_{\rm sys}}{K\sqrt{\Delta\nu\Delta t}} \tag{3.18}$$

Here $T_{\rm sys}$ and K denote the system temperature and antenna gain respectively. For MWA, $K = A_{\rm eff}/(2k_B)$ with $A_{\rm eff} = 21.5\,{\rm m}^2$ for MWA at $\nu = 150\,{\rm MHz}$ (Tingay et al. (2013)). In our analysis we choose $\Delta\nu = 40$ kHz, $\Delta t = 10$ seconds are very small compared to the frequency and time coherence of the signal (Paul & Sethi et al. (2014)). The system temperature has two components: sky temperature (dominant source of noise at low frequency) and receiver temperature. We consider $T_{\rm sys} = 250K$ for a single polarization which is consistent with the reported system temperature at 154.24 MHz for the MWA pointing we consider in this work.

It is fair to assume that the thermal noise for a radio interferometer follows a gaussian statistics with zero mean. In our simulation (Fig. 3.11), we follow the same pipeline used for analysing the real data to estimate the thermal noise power. We use the baseline distribution from the observation with $u_{\rm max} = v_{\rm max} = 250$. For every (u,v) point the noise is drawn from a gaussian distribution with zero mean and the RMS given by Eq. (3.18).

3.6 Conclusions

In this chapter, we propose a new method to extract the HI power spectrum from MWA visibility data in delay space. The proposed method is applicable when a region is tracked using imaging radio interferometers.

One of the crucial factors in power spectrum estimation is how the w-term is dealt within the pipeline. Our findings are that the w-term causes an effective shrinking of primary beam which in turn causes de-correlation of HI signal. We carefully model the HI signal by taking the w-term into account, the weights calculated are then applied to cross-correlate the measured visibilities. Moreover, the cross-correlation approach is particularly useful to

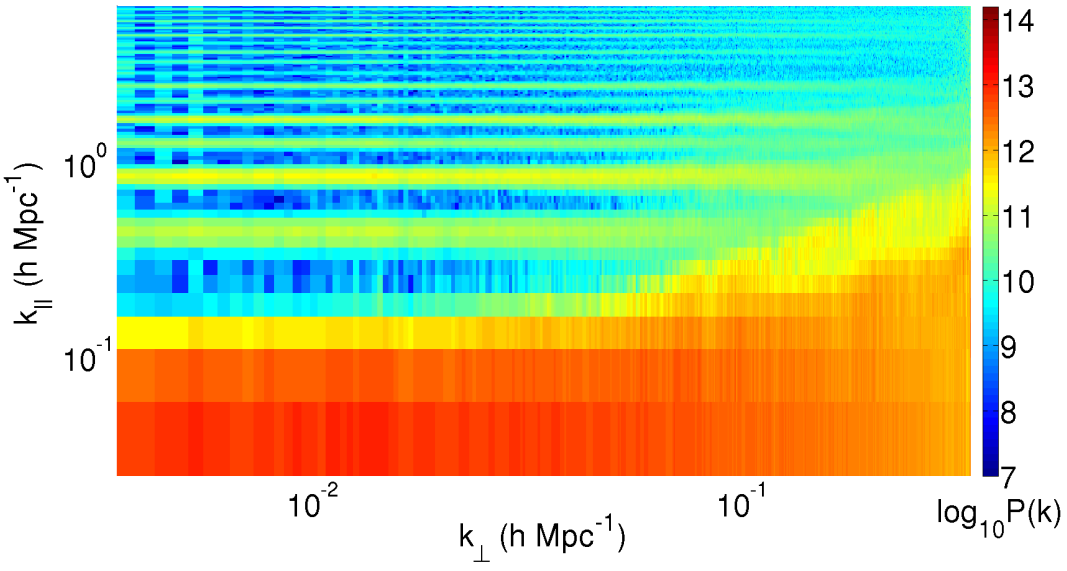

Figure 3.11: The results of the simulation of noise and foregrounds are shown. The power spectrum pipeline developed to analyse the data is also applied to simulated foregrounds and noise for a three hour observational run for a single polarization.

minimize various systematics in the system. We also model and account for the impact of changing intensity pattern in a tracking run. We find this effect to be sub-dominant to the w-term correction.

We analyse three hours of MWA data from the EoR1 field, one of the field identified by the MWA community for EoR science. We present the the results for 3 hours of analysis of EoR1 field. CASA has been used for calibration and to create foreground model using the clean components. Both the dirty (calibrated with no foreground subtraction) & residual (foreground model subtracted) power spectrum in delay space are presented. Our results (Figures 3.8, 3.9 and 3.10) are in good agreement with the thermal noise/foreground simulations and the results of other MWA EoR pipelines (Jacobs et al. (2016)).

In the future we plan to use this pipeline for longer data duration. Our results strongly suggest that we have managed to supress the impact of most systematics for the three-hour run. If more data is used for the same field and similar tracking parameters we expect further reduction of noise. We also hope to apply the method proposed here for longer runs

on a single tracking run. The decorrection caused by of w-term and the changing intensity pattern would be more dominant in this case. This will allow us to test the efficacy of our method for more extreme cases and might indicate the best possible way of detecting the HI signal from EoR.

Chapter 4

Drift Scan method

The statistical detection of the EoR signal requires a stable instrument and a large amount of data to reduce the thermal noise, in addition to measuring and subtracting the foregrounds. The traditional tracking mode of observation may not be useful for this purpose as it leads to a time dependent primary beam as the pointing center is moved. In the drift scan technique the pointing centre is fixed at a particular point on the sky and the observation is carried out for a variable sky pattern. The main advantage of this technique is the stability of the system.

In this chapter we describe a methodology based on drift scans that exploits the correlation between visibilities measured at different times to estimate the EoR signal. In particular, our aim is to infer the efficacy of such a method for a wide field-of-view instrument such as MWA.

In the next section we delineate the basic formalism. In section 4.2, we apply the method to the system parameters of MWA. In section 4.3, we compute the noise on the estimator of the EoR proposed in this chapter and compare the drift scan results with the expected noise in the tracking case. In Section 4.4, we discuss briefly how our method might potentially allow foregrounds represented by bright point sources to be separated from the EoR signal.

4.1 Visibility Correlation in Drift scan

We begin with the visibility due to HI signal measured by a baseline $\mathbf{u}(u,v)$, as given by Eq. (2.9):

$$V_\nu(\mathbf{u}) = \bar{I}_\nu \int \frac{d^3k}{(2\pi)^3}\delta_{\rm HI}(\mathbf{k})e^{ir_\nu k_\parallel} a\left(\mathbf{u} - \frac{\mathbf{k}_\perp r_\nu}{2\pi}\right) \tag{4.1}$$

If the first visibility measurement is obtained at $t = 0$, then, using Eq. (4.1), the visibility measured at a later time t, for a drift scan, can be written as:

$$\begin{aligned} V_\nu(\mathbf{u},t) &= \bar{I}_\nu \int \frac{d^3k}{(2\pi)^3}\delta_{\rm HI}(\mathbf{k}) \int d^2\theta A(\vec{\theta}) \exp\left[ir_\nu\left(k_\parallel + \mathbf{k}_\perp.(\vec{\theta} - \Delta\vec{\theta}(t))\right)\right] \exp(-2\pi i \mathbf{u}.\vec{\theta}) \\ &= \bar{I}_\nu \int \frac{d^3k}{(2\pi)^3}\delta_{\rm HI}(\mathbf{k})e^{ir_\nu k_\parallel} \int d^2\theta A(\vec{\theta}) \exp\left[-2\pi i\left(\mathbf{u} - \frac{\mathbf{k}_\perp r_\nu}{2\pi}\right).\vec{\theta}\right] \exp[-ir_\nu \mathbf{k}_\perp.\Delta\vec{\theta}(t)] \end{aligned} \tag{4.2}$$

Here $\Delta\vec{\theta}(t)$ is the angular shift of the intensity pattern in the time period t. Eq. (4.2) follows from Eqs (2.5)–(2.7) for a changing intensity pattern. In a drift scan, the phase center and the primary beam remain fixed and the only change in the visibility occurs owing to the changing intensity pattern of the sky with respect to the phase center.

Our aim is to calculate the correlation between the visibilities measured at two different times (separated by t), by two baselines $\mathbf{u}$ and $\mathbf{u}'$, and at frequencies ν and ν'. We note that the frequency coverage is far smaller than the central frequency: $|\nu' - \nu| << \nu$. This allows us to write: $|r'_\nu - r_\nu| \equiv \Delta r_\nu = r'_\nu|\nu' - \nu|$; here $r'_\nu \equiv |dr_\nu/d\nu|$.

Using Eqs. (4.1) and (4.2), we can write the visibility correlation function as:

$$\begin{aligned} \langle V_\nu(\mathbf{u}) V^*_{\nu'}(\mathbf{u}',t)\rangle &= \bar{I_\nu}^2 \int \frac{d^3k}{(2\pi)^3} P_{\rm HI}(k) e^{ik_\parallel \Delta r_\nu} a\left(\mathbf{u} - \frac{\mathbf{k}_\perp r_\nu}{2\pi}\right) \int d^2\theta A(\vec{\theta}) \\ &\quad \times \exp\left[-2\pi i\left(\mathbf{u}' - \frac{\mathbf{k}_\perp r_\nu}{2\pi}\right).\vec{\theta}\right] \exp[-ir_\nu \mathbf{k}_\perp.\Delta\vec{\theta}] \end{aligned} \tag{4.3}$$

In the usual case of tracking a fixed region, the ensemble average $\langle \ldots \rangle$ (LHS of Eq. (1.12)) to compute the power spectrum is done by averaging over all modes $\mathbf{k}$ for a given $|\mathbf{k}|$. The drift scan strategy enables another possible method to compute the power spectrum for modes in the plane of the sky $\mathbf{k}_\perp$: averaging over time for a given fixed time difference, Δt, for

visibility measurements. We discuss this issue in detail in section (4.3). For a statistically homogeneous signal, e.g. the EoR, these two methods yield the same estimate of the power spectrum. However, when the assumption of statistical homogeneity breaks down, e.g. for sparsely distributed point sources, the two methods result in different outcomes. We explicitly make use of this difference in our discussion of point sources in a section 4.4.

4.2 Drift scan visibility correlation: MWA

We assume the MWA primary beam to compute the visibility correlations (Eq. (4.3)); MWA primary beam can be expressed as:

$$A(l,m) = \frac{\sin(\pi L_x l)}{\pi L_x l}\frac{\sin(\pi L_y m)}{\pi L_y m} \tag{4.4}$$

Here L_x and L_y are sides of an aperture of an MWA tile in units of wavelength with $L_x \approx L_y \approx 2$ and (l,m) are coordinates defined on the sky.

We note that for a dipole array such as MWA, Eq. (4.4) is valid for only a phase center at the zenith. If the phase center is changed (e.g. for tracking a region), the projected area of the tile decreases which results in an dilation of primary beam depending on the angular position of the phase center. We neglect this change in the chapter and throughout present results for the primary beam given by Eq. (4.4). This assumption alters the signal, the computation of the signal-to-noise and also the impact of the w-term, but doesn't change our main results. We discuss the implications of this assumption in section 4.6.

The knowledge of HI power spectrum (Eq. (1.12)) and the primary beam (Eq. (4.4)) allows us to compute the evolution of visibility correlations. A detailed formulation of the sky coordinate system for analysing drift scans from any arbitrary location of an observatory is discussed in section 4.5. We first discuss the fiducial case of a zenith drift scan for an observatory located at the the latitude ϕ. The visibility correlation function for this case is

derived in section 4.5 and is given by equation (4.22):

$$\begin{aligned}\langle V_\nu(\mathbf{u})V^*_{\nu'}(\mathbf{u}',t)\rangle &= \bar{I_\nu}^2 \int \frac{d^3k}{(2\pi)^3} P_{\rm HI}(k) e^{ik_\parallel \Delta r_\nu} \exp\left(-ir_{\nu'}k_{\perp 1}\cos\phi dH\right) \\ & a\left[\left(u-\frac{r_\nu k_{\perp 1}}{2\pi}\right), \left(v-\frac{r_\nu k_{\perp 2}}{2\pi}\right)\right] \\ & a\left[\left(u'-\frac{r_\nu}{2\pi}(k_{\perp 1}+k_{\perp 2}\sin\phi dH)\right), \left(v'-\frac{r_\nu}{2\pi}(k_{\perp 2}-k_{\perp 1}\sin\phi dH)\right)\right] \end{aligned} \tag{4.5}$$

Here dH is the change in hour angle corresponding to time difference t; u and v are the components of the baseline vector: $\mathbf{u}= u\hat{u}+v\hat{v}$.

Many generic results follow from Eq. (4.5) and they are common to both tracking and drift scan cases, so we first consider $dH = 0$: (a) the contribution in each visibility correlation from different modes is significant when $k_\perp = 2\pi\mathbf{u}/r_\nu \pm 1/(\theta_0 r_\nu)$, where θ_0 is the angular extent of the primary beam. In other words, unless the two baselines being correlated satisfy this condition the visibilities get decorrelated. For MWA primary beam, this implies $\mathbf{u}-\mathbf{u}' \gtrsim 0.5$, (b) If the two visibilities being correlated are separated by a non-zero frequency difference $|\nu'-\nu|$, the signal strength is reduced. We later show that the frequency difference for which the signal drops to half its value: $|\nu'-\nu| \simeq 0.5\,$MHz. We note here that we assume each visibility measurement to have zero channel width $\Delta\nu = 0$. This is justified because the channel width of MWA $\Delta\nu \simeq$ 40kHz which is much smaller than the decorrelation width, or $\Delta\nu \ll |\nu'-\nu|$ (Figure 4.8).

The principle aim here is to analyse the visibility decorrelation in time domain for a drifting sky. We show the behaviour of visibility correlation function as a function of time difference for zenith drift assuming the observatory location to be at three different latitudes: 0° (equator), ±30°, ±90° (pole). The central frequency is chosen to be at $\nu = 129$ MHz corresponding to redshift $z = 10$ and $|\nu'-\nu| = 0.0$ MHz. (figure 4.8). The results are shown for a single baseline vector $\mathbf{u}$=(50, 50) in Figures 4.1–4.3. The envelope of the visibility correlation function shown in the Figures is obtained by multiplying Eq. (4.22) by $\exp(-i2\pi u\cos\phi dH)$ and taking the real part of the resulting expression. This procedure is akin to correcting for the 'shift in the phase center'.

It is clear that at the equator the visibilities measured by the same pair of antennas are correlated for the longest period of time. With increasing latitude of the observer the

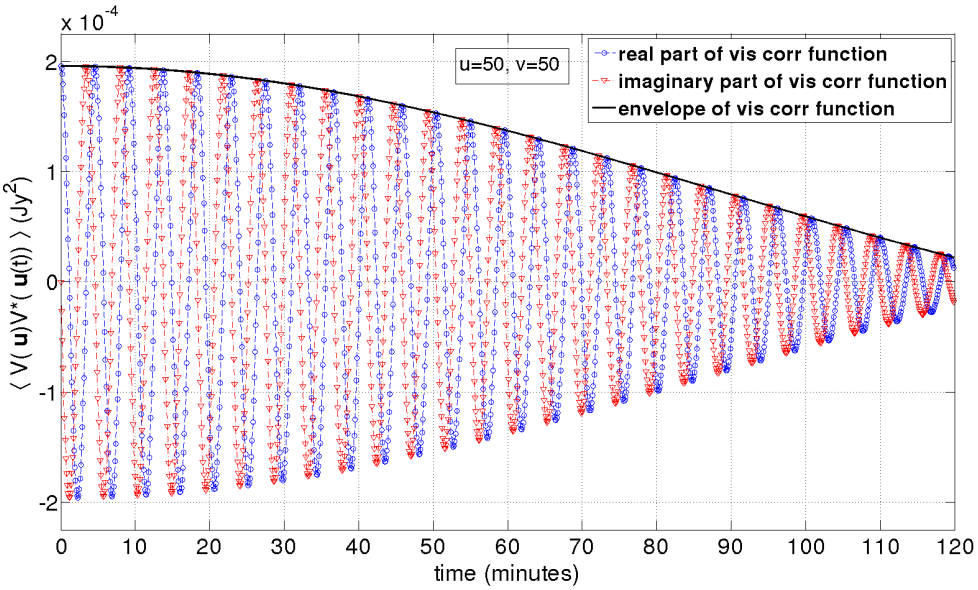

Figure 4.1: Visibility Correlation function as a function of time for zenith drift from equator (latitude=0). Blue and red curves correspond to the real and imaginary part of the visibility correlation function respectively. Black curve denotes the envelope of the Visibility correlation function. In the figure (and all the subsequent figures that display the visibility correlation) the visibility correlation corresponds to the HI signal from EoR computed using the power spectrum of Furlanetto et al. (2006). The central frequency is assumed to be $\nu = 129$ MHz.

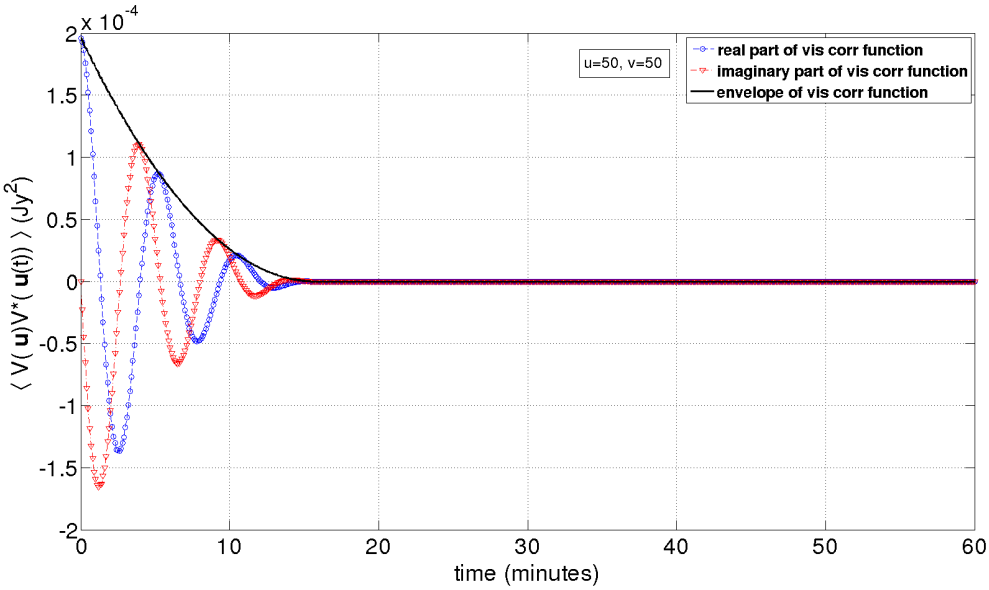

Figure 4.2: Visibility Correlation function as a function of time for zenith drift from a location with latitude $\pm 30°$

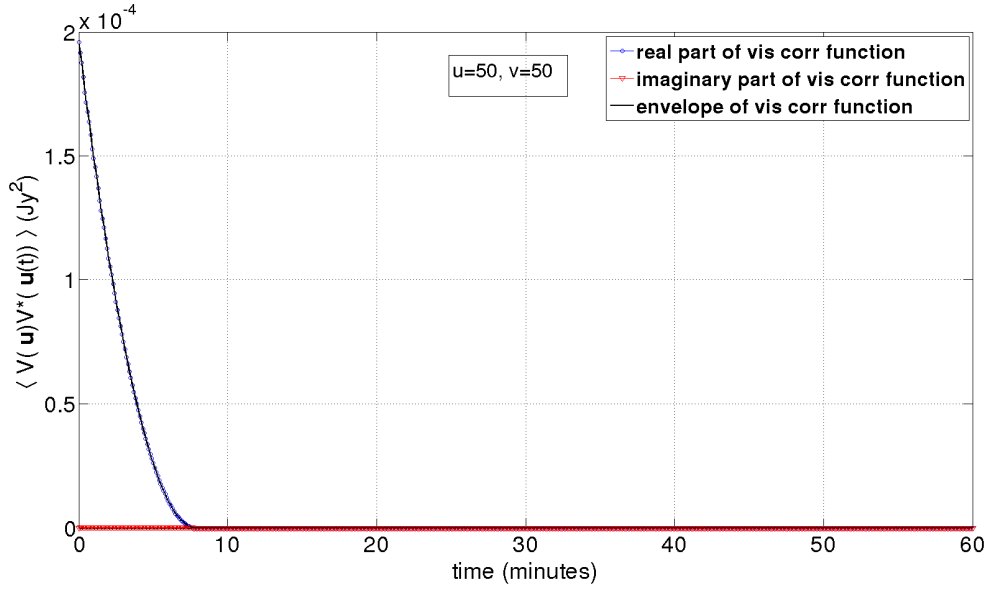

Figure 4.3: Visibility Correlation function as a function of time for zenith drift from the pole (latitude=$\pm 90°$)

correlation time scale decreases and it is minimum for an observer at the pole (latitude 90 degree). During a drift scan, the baselines and primary beam remains fixed and the sources move in and out of the primary beam. As we show in section 4.5, the motion of sources during a scan is a combination of translation and rotation depending on the observer location and the field being observed. At the equator, the drift corresponds to pure translation along east-west axis. From any other location there also exists a rotational component in the zenith drift. The decorrelation time scale is shorter when the rotational component is present. This behaviour can be understood from Eq. (4.5). Unless $\phi = 0$, a baseline u gets contribution from from not just $k_{\perp 1}$ but also $k_{\perp 2}$, the mode perpendicular to u in the tracking case. A similar inference holds for v. This results in decorrelation time scale much shorter than the transit time of the primary beam: $\Delta h \simeq 1/(\sin(\phi)U\theta_0)$, θ_0 is the approximate angular extent of the primary beam. For pure translation, the decorrelation time scale depends only on the transit time of the primary beam.

Of the three fiducial cases we have studied (Figures 4.1-4.3), Figure 4.2 is directly relevant for the location of MWA. It is worthwhile to ask whether we could exploit the long time correlation of the equatorial scan using MWA by scanning an equatorial region. In section 4.5, we show that if the phase center is shifted to the equatorial position (along the local meridian) then with respect to the new phase center the drift is pure translation and the decorrelation due to the rotation can be avoided for this phase center. For a detailed discussion see the section 4.5 and Figures (4.13, 4.14).

For an observatory at latitude ϕ the visibility correlation function with respect to the new phase center can be written as (Eq. (4.25)):

$$\begin{aligned}\langle V_\nu(\mathbf{u})V^*_{\nu'}(\mathbf{u},t)\rangle &= \bar{I_\nu}^2 \int \frac{d^3k}{(2\pi)^3} P_{\rm HI}(k) e^{ik_\parallel \Delta r_\nu} \exp\left(-ir_{\nu'}k_{\perp 1}\cos(\theta+\phi)dH\right) \\ & a\left[\left(u-\frac{r_\nu k_{\perp 1}}{2\pi}\right),\left(v-\frac{r_\nu k_{\perp 2}}{2\pi}\right)\right] \\ & a\left[\left(u-\frac{r_\nu}{2\pi}(k_{\perp 1}+k_{\perp 2}\sin(\theta+\phi)dH)\right),\right. \\ & \left.\left(v-\frac{r_\nu}{2\pi}(k_{\perp 2}-k_{\perp 1}\sin(\theta+\phi)dH)\right)\right]\end{aligned} \tag{4.6}$$

Here θ is the angular distance of the new phase center from zenith for an observatory at

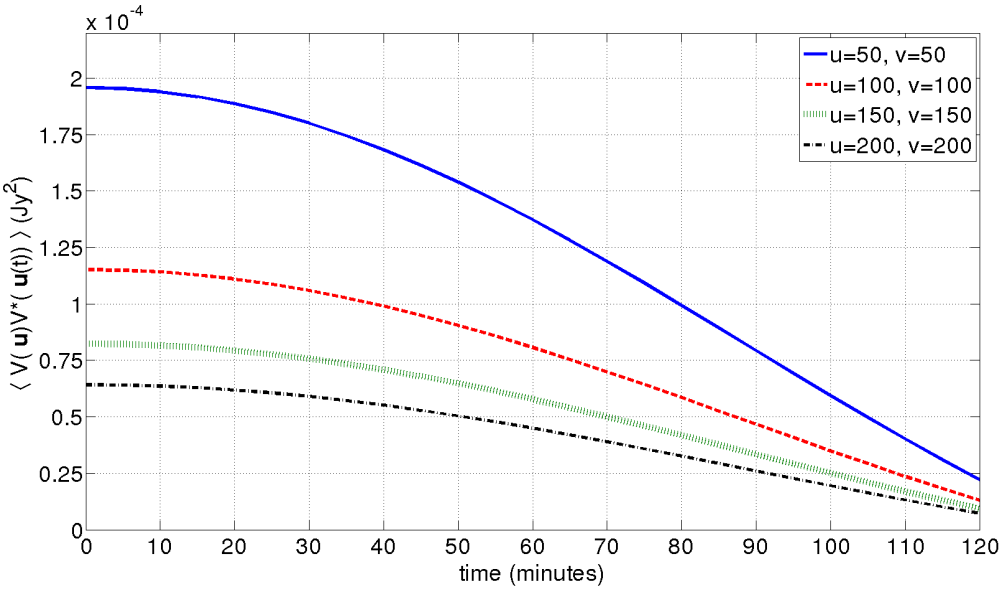

Figure 4.4: Envelope of Visibility Correlation function as a function of time in drift scan mode for four different baselines. The phase center is at zenith for an observer at the equator.

latitude ϕ. To shift the phase center to the equator the rotation angle is $\theta = -\phi$. For this phase center, the time dependence of the visibility correlation follows the behaviour seen in Figure 1 or formally Eq. (4.22) with $\phi = 0$ yields the same result as Eq. (4.25) with $\phi = -\theta$. In other words, the two cases—an observatory located at the equator performing a zenith drift scan and an observatory located at some other latitude scanning a region at the equator–are equivalent.

In Figure (4.4), the time evolution of the visibility correlation function is shown for four different baselines for the equatorial scan.

For observing frequency $\nu = 129$ MHz and $\nu' = \nu$ the visibility correlation is $\simeq 10^{-4}\mathrm{Jy}^2$ for baselines $|\mathbf{u}| \leq 200$. The signal strength decreases with increasing baseline length. Figure (4.4) also shows that the decorrelation time scale depends only the size of the primary beam for an equatorial scan.

4.2.1 Correcting for Rotation

In figures (4.2) and (4.3) one sees that the rotation of sources in the sky plane during the drift scan reduces the time scale of decorrelation of visibility correlation function for a given baseline.

In a drift scan, the phase center remains fixed and therefore there is no change in the values of $\{u, v, w\}$. In other words, the set of baselines during the scan remains the same.

In the foregoing (Eq. (4.5) and the discussion following it) we have shown that the visibilities become uncorrelated when $\mathbf{u} - \mathbf{u}' \gtrsim 0.5$ for the MWA primary beam. In the drift scan case, this condition holds if both the visibilities are obtained at the same time. However, Eq. (4.5) can be used to show that this conclusion doesn't hold for visibilities computed at different times. In particular, we show that $V(\mathbf{u}, t)$ and $V(\mathbf{u}', t')$ can become correlated for $\mathbf{u} \neq \mathbf{u}'$ and $t \neq t'$, if the two baselines are related by a special relation. We derive this relation and illustrate this re-correlation with an example.

Two baselines $\mathbf{u} = (u, v)$ and $\mathbf{u}' = (u', v')$ can be related as:

$$u' = u + av + \varepsilon$$
$$v' = v - au + \varepsilon$$

Here a and ϵ correspond to rotation and translation respectively. These parameters can be solved to give:

$$a = \frac{\Delta u - \Delta v}{u + v}$$
$$\varepsilon = \frac{u\Delta u + v\Delta v}{u + v}$$

Here $\mathbf{\Delta u} = \mathbf{u} - \mathbf{u}'$.

It can be shown that for two baselines with $\varepsilon \geq 0.5$ the signal gets uncorrelated and cannot be re-correlated at any other time. This also means that two baselines with different lengths $(u^2 + v^2)^{1/2}$ remain uncorrelated during the drift scan. However, many baselines in an experiment such as MWA have nearly the same lengths and are related to each other by a near pure rotation denoted by the parameter a. We can show that such baselines correlate with each other during the drift scan if $a = \sin(\phi) dH$. In other words, if a visibility is measured at a time $t = 0$ for a baseline $\mathbf{u}$, then this measurement will correlate with another

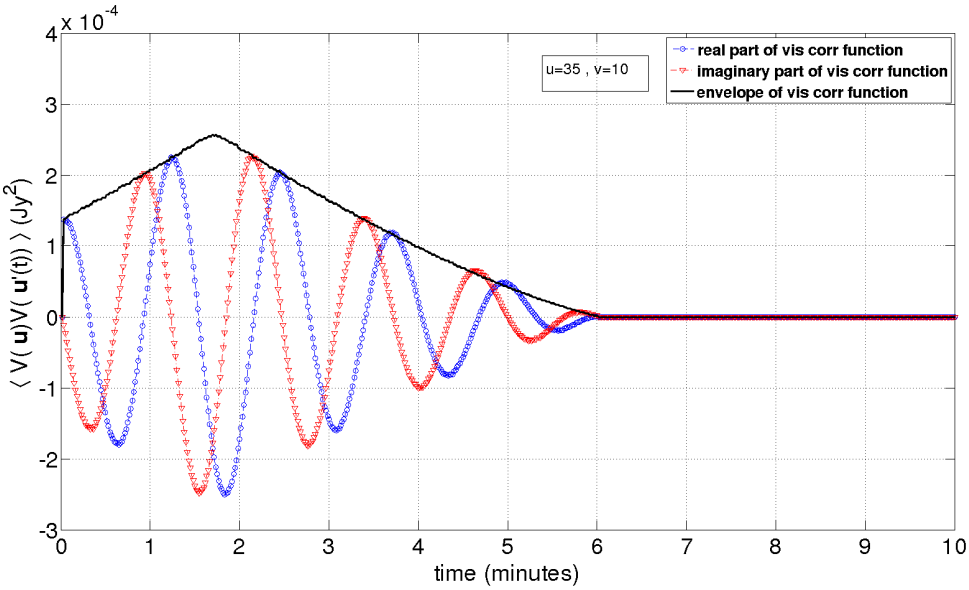

Figure 4.5: Visibility correlation function as a function of time for visibilities with different baselines. The drift scan correspond to a zenith scan for a latitude of 30°

measurement for a baseline $\mathbf{u}'$ at a time corresponding to dH if the two baselines are related by a near pure rotation with the corresponding rotation parameter $a = \sin(\phi)dH$. We note that this correlation can occur just once during a long scan and the time scale over which the baselines remain correlated corresponds to the decorrelation time for a given $|\mathbf{u}|$.

We illustrate this re-correlation for a baseline $\mathbf{u} = (35, 10)$. The other baseline $\mathbf{u}' = (34.8, 10.7)$ corresponds to parameters $a = -0.02$, $\varepsilon = 0$. The visibility correlation function is shown as a function of time in Figure 4.5.

In Figure 4.6 we show the time scale over which the visibility correlation falls to half its value for $\Delta t = 0$ (e.g. Figure 4.2); this time scale is seen to fall as roughly the inverse of the baseline length, in agreement with the discussion in the previous sub-section.

The re-correlation of baselines allows us to partially recover the loss of signal due to decorrelation. However, the set of baselines is fixed for a drift scan strategy and therefore the range of baselines that correlate at different times must be present in the initial set. For the MWA, we estimate that for a zenith scan at the latitude of the telescope there are nearly 120 such pairs which satisfy $\varepsilon \leq 0.5$ and $a \leq 0.3$ for $|\mathbf{u}| \simeq 20$–70. (as noted below,

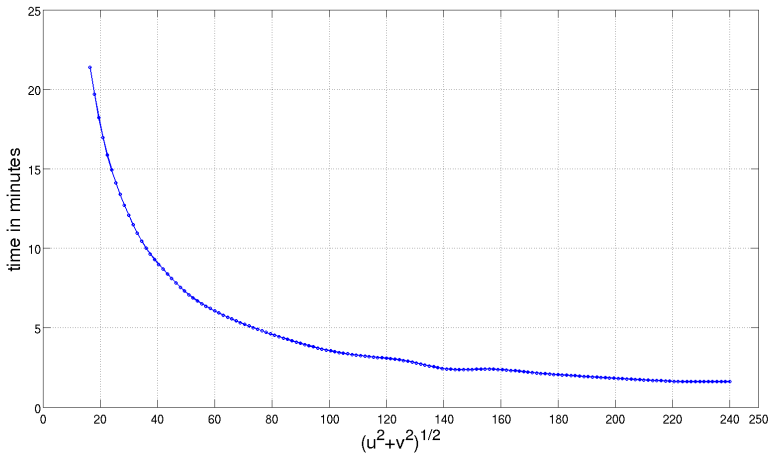

Figure 4.6: The Figure displays the time difference Δt at which the visibility correlation falls to half its value, as a function of baseline, for an overhead scan at the location of MWA ($\phi = -26.7$).

the total number of baselines in a zenith snapshot observation for MWA is 2735 in the range $|\mathbf{u}| \simeq 20$–230.) These baselines will retain at least half the signal and would correlate within a correlation time scale of less than two hours.

4.3 Error on visibility correlation

The error on visibility correlation is:

$$\sigma^2(u) = \langle V_\nu(\mathbf{u}) V_\nu(\mathbf{u}) V_{\nu'}(\mathbf{u}', t) V_{\nu'}(\mathbf{u}', t) \rangle - \langle V_\nu(\mathbf{u}) V_{\nu'}(\mathbf{u}', t) \rangle^2 \tag{4.7}$$

Here $U \equiv |\mathbf{u}|$ and the averages are taken over many different variables: the noise is uncorrelated for different frequencies, baselines, and times. However, the signal could be correlated in all the three domains. We average over all the pairs in the three domains and finally over all the pairs for baselines in the range U and $U + \Delta U$ to compute an estimate for a wider bin ΔU. The measured visibilities and their correlations receive contributions from detector noise, the HI signal, and the foregrounds. When only visibilities at two times (or frequencies/baselines) are correlated, as we assume here, the $\langle VV \rangle$ doesn't receive any contribution from detector noise and therefore constitutes an unbiased estimator of the signal. In this

case, only the first term in the equation above contributes to the error estimate; denoting the sky noise as N_ν, we get:

$$\sigma^2(U) = \frac{1}{N_{\rm tot}} \langle N_\nu(\mathbf{u}) N_\nu^*(\mathbf{u}) \rangle^2 \tag{4.8}$$

Here $N_{\rm tot}$ are all the baseline pairs in the range U and $U + \Delta U$ in the three-dimensional cube and the time domain.

The average noise autocorrelation for each independent correlation of visibilities is:

$$\langle N_\nu(\mathbf{u}) N_\nu^*(\mathbf{u}) \rangle = \left[\frac{T_{\rm sys}}{K\sqrt{\Delta\nu \Delta t}} \right]^2 \tag{4.9}$$

where $T_{\rm sys}$ is the system temperature, $\Delta\nu$ is the channel width, K is the antenna gain and Δt is the integration time. Here Δt and $\Delta\nu$ could be arbitrarily small; in particular we require the bandwidth and integration time to be much smaller than the frequency and time coherence of the signal (Figure 4.1–4.3 and 4.6). $N_{\rm tot}$ is determined from the correlation times scale in time and frequency domains and its computation is discussed below. We cross-correlate all visibility pairs for a given time difference and frequency difference for the equatorial scan case where we assume $\mathbf{u} = \mathbf{u}'$; we also include the impact of re-correlating baselines (section 4.2.1) in the overhead scan case (Figure 4.2).

For a given total observing time T and integration time Δt, there exists $n = T/\Delta t$ visibility measurements. Among these, the number of possible independent correlations between visibilities $i\Delta t$ time apart (where i=1,2,....,n) is $(n - i)$ as explained in figure 4.7. Thus, average noise correlation for a given baseline vector $\mathbf{u}$ with visibilities separated by times $i\Delta t$ is:

$$\sigma_i(\mathbf{u}) = \langle N_\nu(\mathbf{u}) N_\nu^*(\mathbf{u}(i\Delta t)) \rangle = \frac{1}{(n-i)} \left[\frac{T_{sys}}{K\sqrt{\Delta\nu \Delta t}} \right]^2, \tag{4.10}$$

for any frequency channel.

Figure 4.4 shows that the signal $\sqrt{\langle V_\nu(\mathbf{u}) V_{\nu'}^*(\mathbf{u}', t) \rangle}$ decorrelates with increasing time difference between the visibilities. This means that not all pairs contribute equally to the signal-to-noise of the measurement. To obtain an estimator that gives suitable weight to all the pairs we define:

$$w_i(\mathbf{u}) = \frac{\langle V_\nu(\mathbf{u}) V_\nu^*(\mathbf{u}(t=0)) \rangle}{\langle V_\nu(\mathbf{u}) V_\nu^*(\mathbf{u}(t=i\Delta t)) \rangle} \tag{4.11}$$

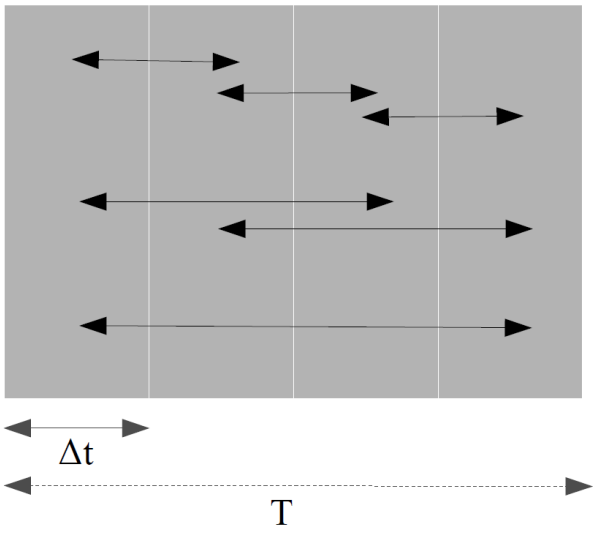

Distance between the visibilities	*No of correlations*
Δt	3
2Δt	2
3Δt	1

Figure 4.7: Illustration showing the number of possible correlations for total observing time T and integration time Δt with $T/\Delta t = 4$, or four visibility measurements. The number of correlations between visibilities with time difference Δt is four, for time difference $2\Delta t$ the number is three and so on.

This allows us to write the following optimal estimator for computing the noise on the visibility measurement:

$$\frac{1}{(\sigma_U^2)^2} = \sum_{i=1}^{n} \frac{1}{(\sigma_i^2 w_i)^2} \tag{4.12}$$

We neglect the effect of partial coherence of baselines at the initial time; this assumption slightly underestimates the sensitivity and is further discussed in the next subsection. We do not include sampling variance in our error estimates.

The foregoing discussion is valid for visibility measurements for a given frequency. The HI signal is correlated across frequency space (Figure 4.8). The figure shows the behaviour of the HI signal as a function of $|\nu' - \nu|$ for different baselines. The bottom panel of the figure displays the frequency difference at which the signal falls to half of the of the maximum ($|\nu' - \nu| = 0$) for different times. We treat the correlation across the frequency space using the same method described above for the time correlation.

In Figure 4.9, we show the expected noise on the visibility correlation for many different cases. For all the cases, we assume the following parameters for the MWA: observing frequency $\nu = 129$ MHz, system temperature $T_{\rm sys} = 440$ K, and the effective area of each tile

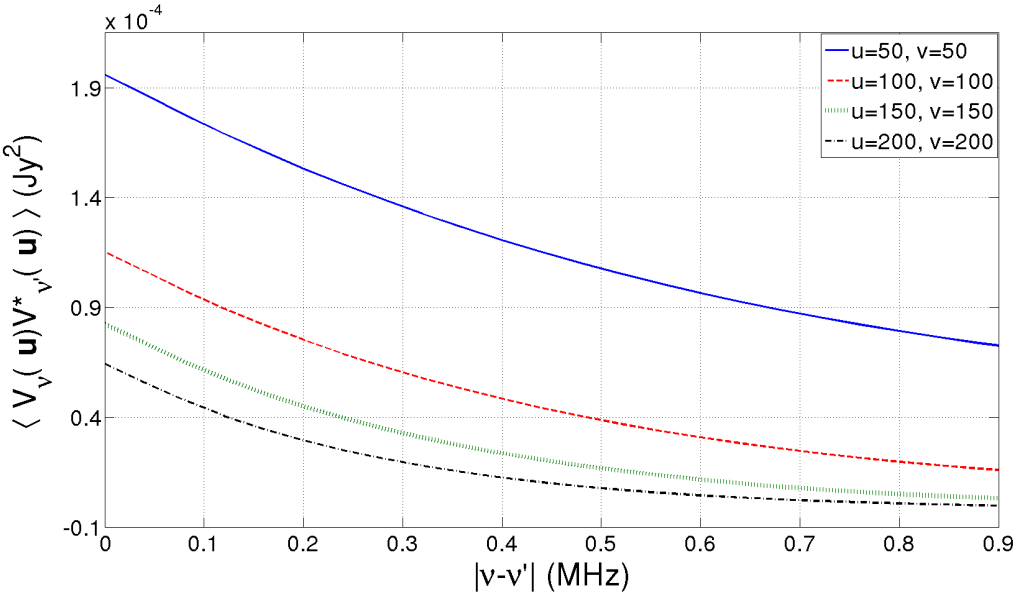

(a)

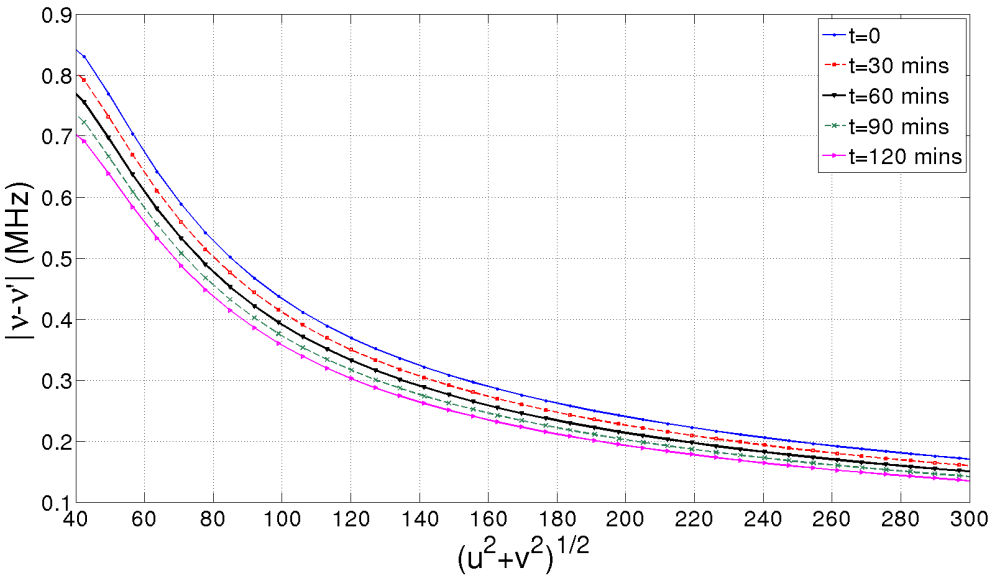

(b)

Figure 4.8: The top figure shows the decorrelation of visibility correlation of the HI signal as a function of frequency separation (see the caption of Figure 4.1 and the discussion in section 4.2 for details). The bottom figure denotes the bandwidth for a given **u** at which the signal drops to half of its maximum at different times

$A_{\rm eff} = 16m^2$.

Case-I: We consider a continuous equatorial drift scan of a duration of 2 and 4 hours. One way to repeat the scan for the same phase center is to shift the phase center to the same position after the end of the scan; this results in the change of UV coverage. We consider the simpler case when the UV coverage and the phase center remain the same for subsequent scans. This corresponds to the same region of sky being observed on different days. In Figure 4.9 we show the results for 900 hours of integration in this mode.

As the signal strength is greater for shorter baselines (figure 4.4), we consider only baselines in the range $\mathbf{u} = 20$–230. We take bins of size $\mathbf{u} \simeq 10$ and show the noise correlation for this range of baselines in Figure 4.9. MWA has 2735 baselines in this range for a snap-shot observation. Using the information, the RMS noise for this mode is $\sigma \simeq 16$ (mJy)^2 and $\sigma \simeq 21$ (mJy)^2 for 2 and 4 hours scan, respectively. We note that since the visibility correlation function drops significantly after roughly 1 hour (Figure 4.1), the noise is expected to increase for longer drift scans.

Case-II: Here we consider an overhead drift scan at the location of MWA. The correlation time scale is shorter for such scans as compared to the equatorial scan (Figure 4.2). In Figure 4.6 we show the time scale over which the correlation falls by half as a function of the baseline length.

As noted above many baselines get re-correlated as the time progresses (Figure 4.5). Over 5–10% of all the baselines in the range $|\mathbf{u}| = 20$–100 get re-correlated with $\epsilon \leq 0.5$ in less than two hours. We include these baselines in the noise computation. As compared to Case I, the noise is higher in this case as the correlation time is shorter.

Case-III: For comparison with the drift scan cases, we also compute the error in the visibility correlation for the tracking case. We consider two cases: 2 and 6 hours continuous tracking of a region across the zenith ($\pm$1h and $\pm$3h) at the location of MWA ($\phi = -26.7$). The results are shown Figure 9. We discuss the results in detail in the next subsection.

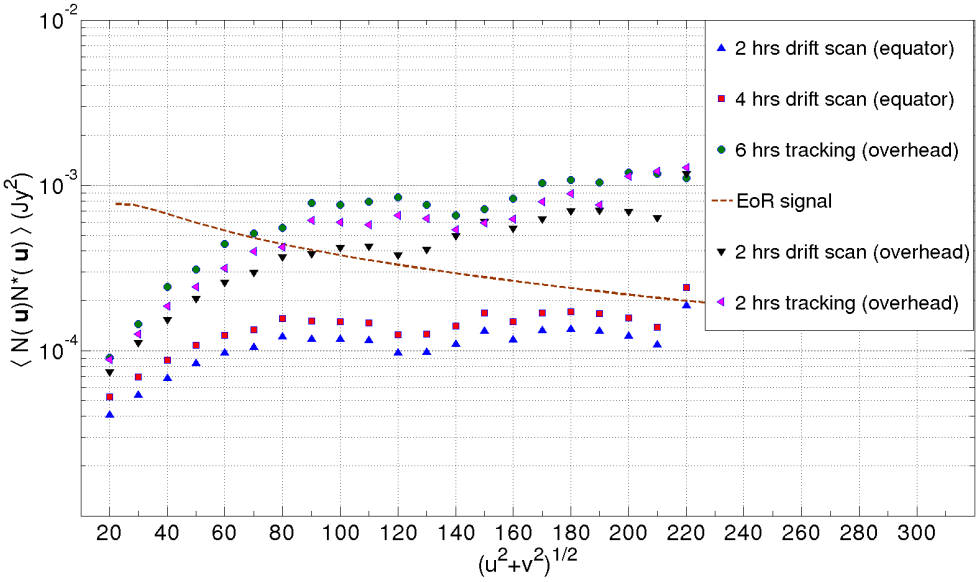

Figure 4.9: Error on visibility correlation as a function of baseline length: blue (triangle) and red (square) points refer to 2 and 4 hours equatorial drift scans, respectively. Black (inverted triangle) points refer to 2 hours zenith drift scan at the location of MWA. The green (circle) and pink (rotated triangle) points show the expected error for 2 and 6 hour tracking runs (for ± 3 and ± 1 hour continuous overhead tracking at MWA location). In all the cases the total integration is 900 hours. The EoR signal is designated by the dashed brown line.

4.3.1 Drift vs tracking mode

In any interferometric experiment to determine the EoR signal, the RMS noise on the visibility correlation is bounded by:

$$\sigma_{\rm min} = \left(\frac{1}{N_b}\right)^{1/2} \left(\frac{T_{\rm sys}K}{\sqrt{\Delta\nu T}}\right)^2 \tag{4.13}$$

$$\sigma_{\rm max} = \left(\frac{\Delta t}{N_b T}\right)^{1/2} \left(\frac{T_{\rm sys}K}{\sqrt{\Delta\nu \Delta t}}\right)^2. \tag{4.14}$$

Here T is the total time of integration and Δt is the integration time for a single visibility measurement. For the sake of the discussion, $\Delta\nu$, the channel width is assumed to be fixed. $N_b = n(n-1)/2$ is the total number of baselines for any measurement with n antenna elements. $\sigma_{\rm min}$ gives the RMS noise if all the visibilities are coherently added and $\sigma_{\rm max}$ corresponds to the case when the visibility correlations are incoherently added. For the 128-tile MWA, the RMS lies between these two extremes for both the tracking mode and drift scans. As noted above, we neglect partially coherent baselines for computing the sensitivity for drift scans; this assumption is consistent with Eq (4.13).

The process of decoherence occurs differently for the tracking and the drift scan mode. For drift scans, it is decorrelation of the EoR signal at different times, as described in detail in the previous sections. In the tracking case, the process of tracking a given region rotates the visibility vector $\mathbf{u}$; the correlation between visibility measurements at different values of $\mathbf{u}$ decreases; from Eq. (4.3), we can show that the decorrelation scale $\Delta\mathbf{u} \simeq \theta_0^{-1} \simeq 0.5$ has very weak dependence on the value of $\mathbf{u}$. For our computation we take the pixel size: $\{\Delta u, \Delta v\} = \{0.5, 0.5\}$. The frequency decorrelation for the tracking case is taken from figure 4.8.

The results for two and six hour tracking runs (zenith at the location of MWA) are shown for 900 hours of integration in figure 4.9. We note here that we do not present the results for equatorial tracking run, as the sensitivity in this case shows only a marginal improvement over the zenith tracking runs shown in Figure 4.9. As the figure shows, the drift scan generally gives lower noise on the visibility correlation for up to 4 hours of drift scans.

This result can be understood as follows. As an extreme case, one could drift for a very short duration each day, such that there is no decorrelation and continue similar observations

on the same field such that all the visibility measurements are coherently added. In this case, the RMS for the drift case would approach $\sigma_{\rm min}$ which is not possible to achieve in the tracking case because the process of tracking would always decorrelate the signal. The relevant question is: what is the time scale for drift scans such that this advantage of lower noise is not lost. We show that even for four-hour drift scans this advantage holds. In the drift scan case, the decorrelation time scale is $\simeq$ 1hour. In the tracking cases, different baseline decorrelate in the process of tracking a region of the sky but some baselines revisit the same pixel in this process. For instance, for a six hour tracking run shown in Figure 4.9, the average integration time of a pixel in the range: $|\mathbf{u}| = 20$–30 is roughly 15 minutes with the total number of uncorrelated pixels $\simeq 4700$.

It should be underlined that, apart from other assumptions delineated in the previous sub-section, the lower noise in the drift scan is also based on the assumption that the system temperature doesn't change over the scan. Also an additional disadvantage in the drift scan case is that there are smaller number of visibility measurements available at any given time for imaging as compared to the tracking case where the UV coverage is better.

4.4 Statistical homogeneity of EoR signal and foreground extraction

Unlike the tracking case, the drift scans explicitly exploit the statistical homogeneity of the EoR signal: cross correlation of the signal at different times only depends on the time difference. More precisely, the power spectrum of the EoR signal for any phase center is drawn from a random density field with the same average power spectrum. This assumption may or may not hold for foregrounds. For instance, if faint point sources are distributed homogeneously across the sky with the same flux distribution, they will also closely correspond to a statistically homogeneous field in two dimensions. However, most other foregrounds, e.g. bright point sources or galactic foregrounds, will explicitly break the statistical homogeneity of the sky and therefore would be potentially distinguishable from the EoR signal.

We illustrate this concept with point source distribution on the sky. For a point source

distribution with fluxes $\{F_i\}$, the visibility can be written as:

$$V(\mathbf{u}) = \sum_j \exp(2\pi i \mathbf{u}.\theta_\mathbf{j}(t)) F_j A(\theta_\mathbf{j}(t)) \tag{4.15}$$

Here $\theta_\mathbf{i}(t)$ correspond to the time varying position of point sources on the sky with respect to the fixed phase center. $A(\theta_\mathbf{i}(t))$ gives the primary beam in the same coordinate system. The visibility correlation separated by time Δt is:

$$\langle V(\mathbf{u},t)V^*(\mathbf{u},t+\Delta t)\rangle = \langle \sum_k \sum_j \exp(2\pi i \mathbf{u}.(\theta_\mathbf{j} - \theta_\mathbf{k})) F_j F_k A(\theta_\mathbf{j}(t)) A(\theta_\mathbf{k}(t+\Delta t))\rangle \tag{4.16}$$

Here the averaging process $\langle \cdots \rangle$ is over all the pairs for a given Δt during the drift scan. This averaging procedure leads to substantially different results for the EoR signal and the foregrounds: the EoR signal is statistically homogeneous and therefore any cross-correlation depends only on Δt. For each Δt the EoR signal gives a realization of the density field with a given fixed power spectrum (Eq. (4.3)). However, the foregrounds might not share this property and might show explicit dependence not just the time difference but the time period of the scan. This gives at least two different methods of extracting foregrounds: (a) correlation pairs of a given Δt can be used to fit the time variation expected of foregrounds. While the EoR signal will show fluctuations about a given mean, the foregrounds will show more secular time variation which can potentially be subtracted, (b) direct comparison of the averaged correlation function should also reveal the difference between the two cases. We demonstrate the procedure with method (b) here.

For MWA primary beam, we consider three different source counts: 10, 30 and 50 sources. At the beginning of the drift scan the sources are randomly distributed within $\pm 15°$ from the center of the primary beam with hour angle between -3 to +3 hours. The fluxes are drawn from uniform distribution with values between 0 and 1 Jy. The visibility correlation function for all these cases for $\mathbf{u}$=(50,50) are shown in figure 4.10.

As predicted in the foregoing, figure 4.10 shows that the visibility correlation function for point sources is substantially different as compared to the HI signal owing to statistical inhomogeneity of the point source distribution. This can be used to subtract the contribution of bright point sources from the measured visibility itself.

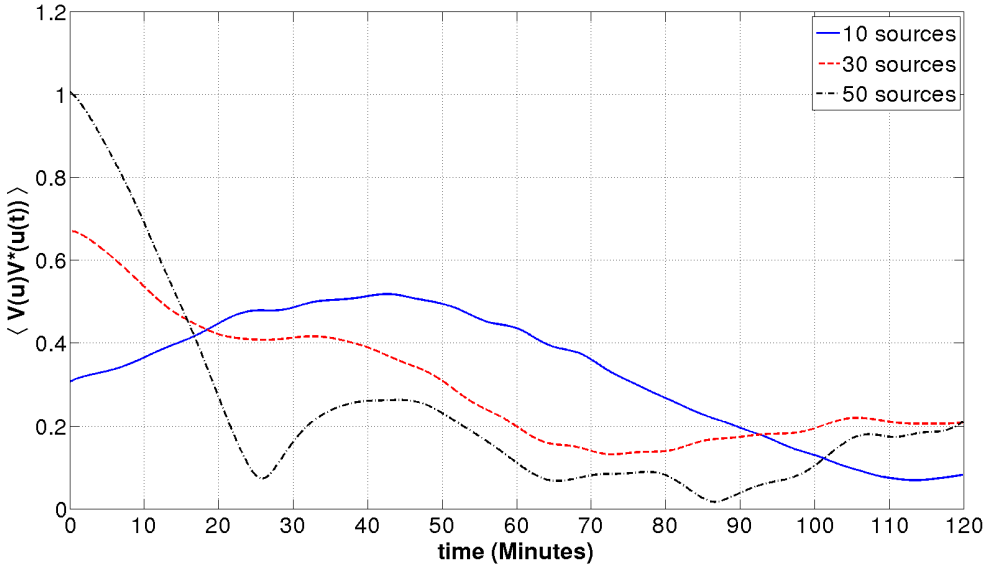

Figure 4.10: Envelope of the Visibility correlation function (normalized arbitrarily) as a function of time difference for three different cases described in the text.

4.5 Coordinate system for drift scans

The position vector in the sky $\vec{\theta}$ can be expressed in terms of two direction cosines l and m. These direction cosines are defined with respect to a local coordinate system when phase center is at zenith as explained in figure 4.11 (e.g. Christiansen & Hogbom (1969)):

$$\begin{aligned} l &= \cos\delta \sin H \\ m &= \cos\delta \cos H \sin\phi - \sin\delta \cos\phi \\ n &= \cos\delta \cos H \cos\phi + \sin\delta \sin\phi \end{aligned} \tag{4.17}$$

Here δ and H are the declination and hour angle of any source; and ϕ is the latitude of the place of observation.

Using this coordinate system the second integral in visibility expression Eq. (4.2) takes the form:

$$\int dldmA(l,m) \exp\left[-2\pi i \left\{\left(u - \frac{k_{\perp 1} r_\nu}{2\pi}\right) l + \left(v - \frac{k_{\perp 2} r_\nu}{2\pi}\right) m\right\}\right] \exp\left[-i r_\nu \left(k_{\perp 1}\Delta l + k_{\perp 2}\Delta m\right)\right] \tag{4.18}$$

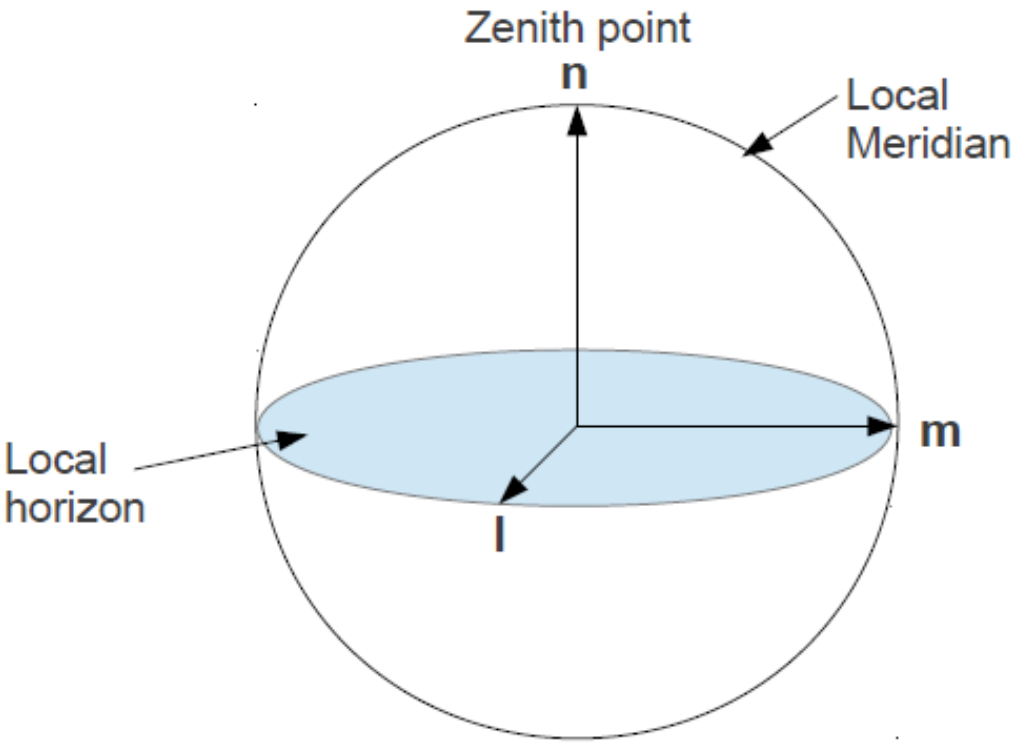

Figure 4.11: l,m,n coordinates defined for a phase center at zenith

Here Δl and Δm are the change in l and m with time or hour angle as in sky drift only hour angle changes with time for a fixed declination. $k_{\perp 1}$ and $k_{\perp 2}$ are the two components of $\mathbf{k}_\perp$ along l and m on the sky plane. Using Eq. (4.17) and the condition $l^2+m^2+n^2=1$ we can expand in the first order to compute the changes in relevant quantities:

$$\Delta l = (m\sin\phi + n\cos\phi)dH; \qquad \Delta m = -(l\sin\phi)dH. \tag{4.19}$$

Here dH is the change in hour angle in time interval t. We can further simplify the expression by using $n \simeq 1$. The two approximation used above are: $1/2(l^2+m^2) \ll 1$ and $dh \ll 1$. Both these approximations are valid for the MWA primary beam (Eq. (4.4)) and for a few hours of correlation time. Thus the second integral (Eq. 4.17) becomes:

$$\exp\left(-ir_\nu k_{\perp 1}\cos\phi dH\right)\int dldmA(l,m)\exp\left[-2\pi i\left\{\left(u-\frac{r_\nu}{2\pi}(k_{\perp 1}+k_{\perp 2}\sin\phi dH)\right)l + \left(v-\frac{r_\nu}{2\pi}(k_{\perp 2}-k_{\perp 1}\sin\phi dH)\right)m\right\}\right]$$

It can be expressed in terms of the Fourier transform of the primary beam:

$$\exp\left(-ir_\nu k_{\perp 1}\cos\phi dH\right)a\left[\left(u-\frac{r_\nu}{2\pi}(k_{\perp 1}+k_{\perp 2}\sin\phi dH)\right),\left(v-\frac{r_\nu}{2\pi}(k_{\perp 2}-k_{\perp 1}\sin\phi dH)\right)\right] \tag{4.20}$$

With this the visibility measured at a later time t becomes:

$$\begin{aligned} V_\nu(\mathbf{u},t) &= \bar{I}_\nu\int\frac{d^3k}{(2\pi)^3}\delta_{\rm HI}(\mathbf{k})e^{ir_\nu k_\parallel}\exp\left(-ir_\nu k_{\perp 1}\cos\phi dH\right) \\ &\quad a\left[\left(u-\frac{r_\nu}{2\pi}(k_{\perp 1}+k_{\perp 2}\sin\phi dH)\right),\left(v-\frac{r_\nu}{2\pi}(k_{\perp 2}-k_{\perp 1}\sin\phi dH)\right)\right] \end{aligned} \tag{4.21}$$

Correlating this with the visibility measured at t=0 (equation 4.1) gives:

$$\begin{aligned} \langle V_\nu(\mathbf{u})V^*_{\nu'}(\mathbf{u}',t)\rangle &= \bar{I_\nu}^2\int\frac{d^3k}{(2\pi)^3}P_{\rm HI}(k)e^{ik_\parallel\Delta r_\nu}\exp\left(-ir_{\nu'}k_{\perp 1}\cos\phi dH\right) \\ &\quad a\left[\left(u-\frac{r_\nu k_{\perp 1}}{2\pi}\right),\left(v-\frac{r_\nu k_{\perp 2}}{2\pi}\right)\right] \\ &\quad a\left[\left(u'-\frac{r_\nu}{2\pi}(k_{\perp 1}+k_{\perp 2}\sin\phi dH)\right),\left(v'-\frac{r_\nu}{2\pi}(k_{\perp 2}-k_{\perp 1}\sin\phi dH)\right)\right] \end{aligned} \tag{4.22}$$

Eq. (4.22) and the discussion in this section allows us to interpret Figure 4.1–4.3. If $\phi = 0$, or the observatory is located at the equator, then the trajectory of sources around the phase

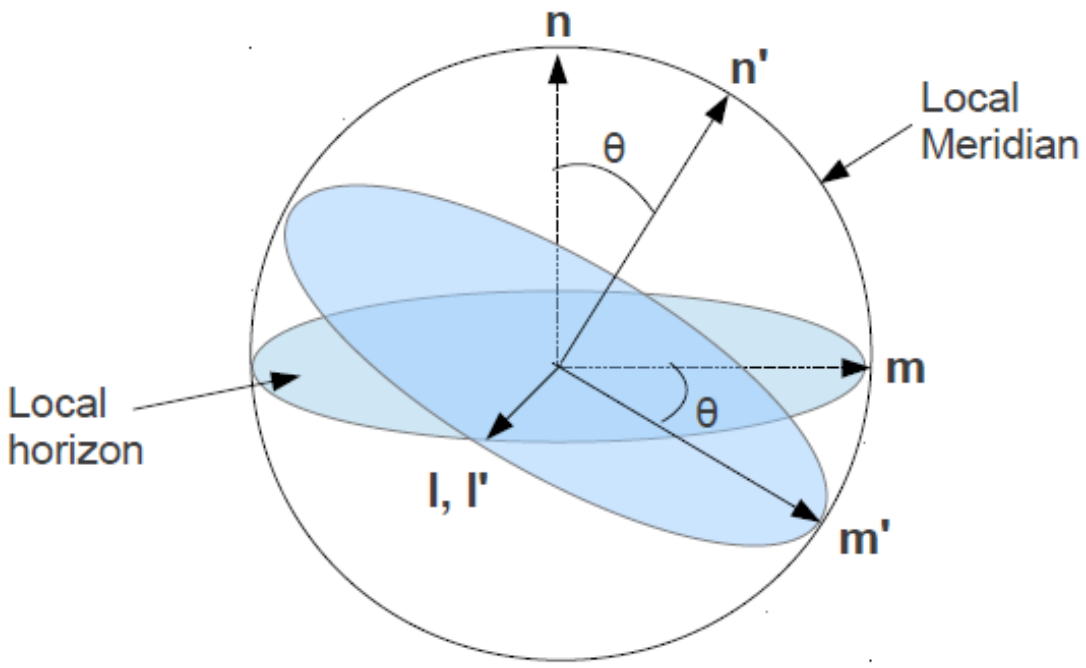

Figure 4.12: Illustration of new lmn coordinate system

center in a drift scan is pure translation; for any non-zero ϕ the motion is a combination of rotation and translation (Eq. (4.19). For pure translation, one obtains Figure 4.1, or the decorrelation time scale is determined solely by the extent of the primary beam. The decorrelation time scale is shorter for any non-zero ϕ (Figure 4.2, 4.3, and 4.6) and depends on the baseline, as already noted in section 4.2.

MWA is not located at the equator but we show below that, even for an observatory not located at the equator, if the phase center is shifted to an equatorial position one can remove the rotation of sources in the coordinate system constructed for the new phase center. For simplicity we construct a coordinate system around the local meridian but our conclusions remain valid for any phase center along the equator.

For a phase center that lies on the local meridian with angular separation θ from the zenith at the observatory (Figure 4.12), the new set of coordinate system is obtained by a single rotation θ of the m and n axes about l as shown in the figure 4.12. Thus the new

coordinates can be expressed as:

$$\begin{pmatrix} l' \\ m' \\ n' \end{pmatrix} = \begin{pmatrix} 1 & 0 & 0 \\ 0 & \cos\theta & \sin\theta \\ 0 & -\sin\theta & \cos\theta \end{pmatrix} \begin{pmatrix} l \\ m \\ n \end{pmatrix} \tag{4.23}$$

Substituting l,m,n values from equation (4.17) we get:

$$\begin{aligned} l' &= \cos\delta \sin H \\ m' &= \cos\delta \cos H \sin(\theta+\phi) - \sin\delta \cos(\theta+\phi) \\ n' &= \cos\delta \cos H \cos(\theta+\phi) + \sin\delta \sin(\theta+\phi) \end{aligned} \tag{4.24}$$

We illustrate the difference between the two coordinate systems with a set of point sources with given initial positions (hour angle and declination) and compute source trajectories in both lmn and l'm'n' coordinates. The unprimed coordinates are for a zenith scan at the location of the observatory. The primed coordinates are for a phase center which is at equatorial position at the meridian. In this case, for on observer situated at latitude ϕ, the angle of rotation $\theta = -\phi$. For instance for an observer at latitude $\phi = 30°$N, rotation angle is $\theta = -30°$.

Ten sources are chosen randomly within declination $\pm 10°$ of the center of the primary beam and all with initial hour angle -2h. The sources are allowed to drift past the primary beam for a total drift duration of 4 hours. The trajectories are shown figures 4.13 and 4.14. A contour plot of the primary beam is also included in each figure.

Using the new primed coordinate system instead of the previous one with phase center at zenith at the observatory, one obtains the expression for the visibility correlation function as:

$$\begin{aligned} \langle V_\nu(\mathbf{u}) V^*_{\nu'}(\mathbf{u}', t)\rangle &= \bar{I_\nu}^2 \int \frac{d^3k}{(2\pi)^3} P_{\rm HI}(k) e^{ik_\parallel \Delta r_\nu} \exp\left(-i r_{\nu'} k_{\perp 1} \cos(\theta+\phi) dH\right) \\ & \quad a\left[\left(u - \frac{r_\nu k_{\perp 1}}{2\pi}\right), \left(v - \frac{r_\nu k_{\perp 2}}{2\pi}\right)\right] \\ & \quad a\left[\left(u' - \frac{r_\nu}{2\pi}(k_{\perp 1} + k_{\perp 2}\sin(\theta+\phi) dH)\right), \right. \\ & \quad \left.\left(v' - \frac{r_\nu}{2\pi}(k_{\perp 2} - k_{\perp 1}\sin(\theta+\phi) dH)\right)\right] \end{aligned} \tag{4.25}$$

Eqs (4.25) and (4.22) are the main results of this work.

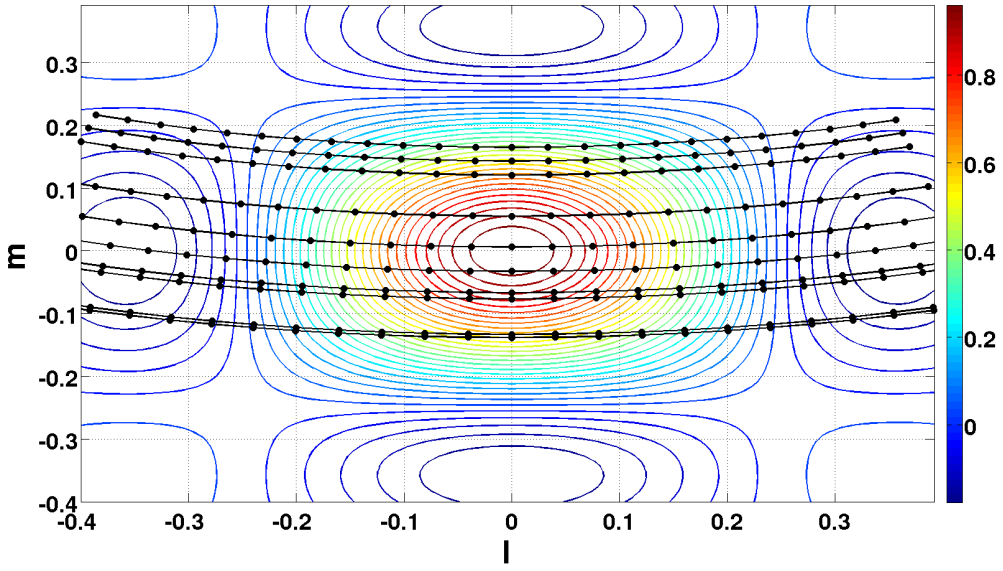

Figure 4.13: source trajectories in lmn coordinate system (phase center at zenith) for an observer at latitude $-30°$

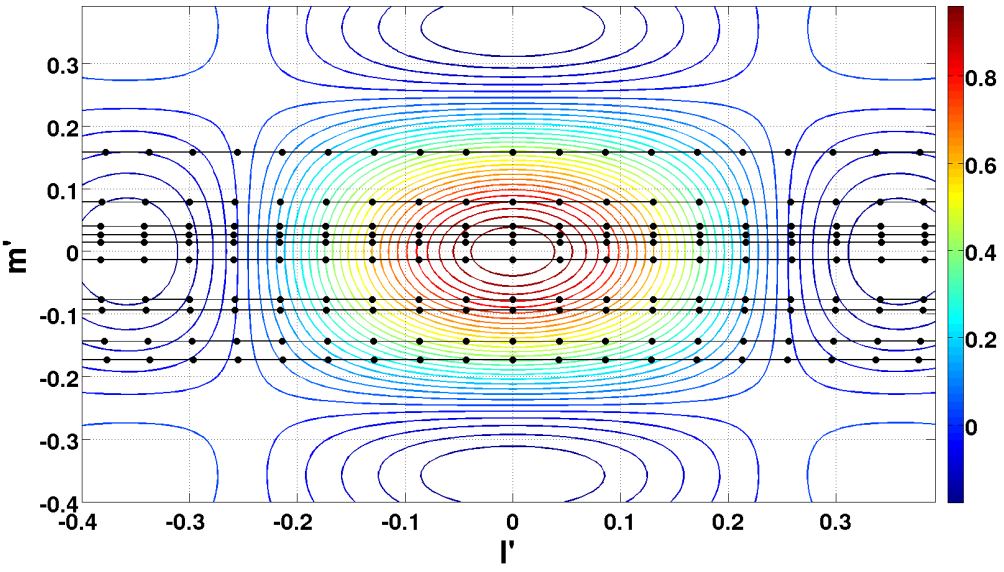

Figure 4.14: source trajectories in l'm'n' coordinate system (phase center shifted to equator) for the same observer as in Figure 4.13

4.6 w-term and other assumptions

We have neglected the w-term in our formalism. In this section, we attempt to assess the possible impact of this term. The inclusion of w-term changes the visibility expression to:

$$V_\nu(\mathbf{u}) = \int A(\vec{\theta}) I_\nu(\vec{\theta}) e^{-i2\pi(ul+vm+w(1-n))} d\Omega \tag{4.26}$$

Here $n = (1 - l^2 - m^2)^{1/2}$. The solid angle $d\Omega = dldm/(1-n)$. For MWA primary beam we can use the flat sky approximation $1/2(l^2 + m^2) \ll 1$ (Figure 4.13 and 4.14). As noted above this approximation might break down when regions close to horizon are tracked. However, it remains a good approximation for zenith drift scan. We also make the simplifying assumption that the primary beam is a Gaussian: $A(l,m) = \exp(-(l^2+m^2)/\theta_0^2)$; this allows us to make analytic estimates.

From Eq. (4.25), including the w term, the visibility at any time t can be written as (we assume $\theta = 0$, or a zenith scan):

$$\begin{aligned} V_\nu(u,v,w;t) &= \bar{I}_\nu \int \frac{d^3k}{(2\pi)^3} \delta_{\rm HI}(\mathbf{k}) e^{ir_\nu k_\parallel} \exp\left(-ir_\nu k_{\perp 1} \cos\phi dH\right) \\ &\times \int dldm A(l,m) \exp\Big[-2\pi i \Big\{ \Big(u - \frac{r_\nu}{2\pi}(k_{\perp 1} + k_{\perp 2}\sin\phi dH)\Big) l \\ &+ \Big(v - \frac{r_\nu}{2\pi}(k_{\perp 2} - k_{\perp 1}\sin\phi dH)\Big) m - \frac{1}{2} w (l^2+m^2) \Big\}\Big] \end{aligned}$$

For a Gaussian primary beam, the integral over angles can be computed analytically by extending the integration limits from $-\infty$ to ∞ which is permissible as the primary beam has a narrow support. This gives us:

$$\begin{aligned} V_\nu(u,v,w;t) &= \bar{I}_\nu \int \frac{d^3k}{(2\pi)^3} \delta_{\rm HI}(\mathbf{k}) e^{ir_\nu k_\parallel} \exp\left(-ir_\nu k_{\perp 1} \cos\phi dH\right) \\ &\times \left(\frac{\pi}{q}\right) \exp\left(-a_1^2/(4q)\right) \exp\left(-a_2^2/(4q)\right) \end{aligned} \tag{4.27}$$

Here, for an zenith scan, $a_1 = [u - \frac{r_\nu}{2\pi}(k_{\perp 1} + k_{\perp 2}\sin\phi dH)]$ and $a_2 = [v - \frac{r_\nu}{2\pi}(k_{\perp 2} - k_{\perp 1}\sin\phi dH]$ and $q = (\frac{1}{\theta_0^2} - iw\pi)$. Eq. (4.27) shows that the main impact of the w-term is to make the primary beam term complex. The w-term results in the information being distributed differently between the real and imaginary part of the visibility. If we consider just the real part of the visibility, the primary beam appears to shrink by a factor: $1/(1+\pi^2 w^2 \theta_0^4)$, which

is indicative of the well-known result that the presence of w-term decreases the angular area that can be imaged.

The visibility correlation is computed to be:

$$\begin{aligned}\langle V_\nu(u,v,w)V^*_{\nu'}(u',v',w';t)\rangle &= \bar{I_\nu}^2 \int \frac{d^3k}{(2\pi)^3} P_{\rm HI}(k) e^{ik_\parallel \Delta r_\nu} \exp\left(-ir_{\nu'}k_{\perp 1}\cos(\phi)dH\right) \\ &\times \left(\frac{\pi}{p}\right)\left(\frac{\pi}{p'}\right)\exp\left(-\frac{a_1^2}{4p}\right)\exp\left(-\frac{a_2^2}{4p}\right) \\ &\times \exp\left(-\frac{a_3^2}{4p'}\right)\exp\left(-\frac{a_4^2}{4p'}\right) \qquad (4.28)\end{aligned}$$

Here $a_3 = [u' - \frac{r_\nu}{2\pi}k_{\perp 1}]$, $a_4 = [v' - \frac{r_\nu}{2\pi}k_{\perp 2}]$, $p = (1/\theta_0^2 + \theta_0^2 w^2\pi^2)$, $p' = (1/\theta_0^2 + \theta_0^2 w'^2\pi^2)$. For $w, w' = 0$, Eq. (4.28) reduces to Eq. (4.5) for a Gaussian beam. One of the important conclusions of Eq. (4.28) is that the inclusion of w-term doesn't alter the nature of coherence of visibilities over time. The main impact of the w-term is to effectively shrink the size of primary beam from θ_0^2 to $1/p$. It can be shown that the visibility correlation scales as the primary beam (e.g. Eqs (11)–(13) of Bharadwaj & Sethi (2001)), and therefore, for non-zero w, the correlation of raw visibilities results in a decrease in the signal. We note that for near coplanar array such as MWA, this effect is negligible for zenith drift scans.

An important application of Eq. (4.28) occurs in computing the sensitivity of the detection of the HI signal in the tracking mode ($dH = 0$ for the tracking case). As described in section 4.3.1, we assume all the visibilities in a narrow range of baselines to be coherent. However, these visibilities are computed at different times while tracking a region and therefore correspond to different values of w. Eq. (4.28) allows us to compute the loss of this correlation.

The impact of w-term can be tackled using well-known algorithms based on facet imaging or w-projection (for details see e.g. Cornwell et al. (2008)). In other words, if raw visibilities are correlated then we expect a small loss of signal. However, if the raw visibilities are first treated by facet imaging then the impact of w-term can be reduced for either drift scans and tracking. We hope to return to this issue in future work.

Throughout this work we assume the primary beam to be given by Eq. (4.4). As noted above, this assumption is only valid for a phase center fixed to the zenith at the location of MWA. If the phase center is moved to a point on the sky that makes an angle δ with the zenith then the projected area in that direction scales as $\cos\delta$ and the primary beam scales

as $1/cos\delta$. As noted above the HI signal scales as the primary beam. The antenna gain K (Eq. (4.9)) scales as the effective area of the telescope or as the inverse of the primary beam. As the error on the HI visibility correlation scales as the square of the antenna gain (Eq. (4.9)), the signal-to-noise for the detection of the HI signal degrades as $\propto \cos\delta$. For instance, an equatorial drift scan would result in a loss of a factor of roughly 1.2 in signal-to-noise as compared to the zenith scan. This loss of sensitivity is severer for the tracking case if regions far away from the zenith are tracked. We note that our conclusions based on the cases considered in this chapter are not altered by this loss.

4.7 Conclusions

The main goal of this work is to investigate the potential of the drift scan technique in estimating the EoR signal. Drift scans introduce a new dimension to the issue: the correlation between visibilities in time domain. Here we present a formalism which uses this correlation to determine the EoR signal.

The important results are as follows:

- The visibilities measured at different times by the same pair of antennas in a drift scan are correlated for up to 1 hour for equatorial scans (Figure 4.1). The decorrelation time scale depends on the choice of phase center. It is maximum for an equatorial zenith drift or for equatorial phase center. For such scans, the decorrelation time scale is independent of the baseline length. For other scans the decorrelation times scale is shorter and depends on the baseline vector (Figure 4.2–4.3). However, a fraction of these baselines correlate with other baselines at a different time (Figure 4.5).

- We compute the expected error on the visibility correlation for drift scans and compare with the expected noise in the tracking case (Figure 4.9). Our results show that the noise is comparable in the two cases and the drift scan might lead to a superior signal-to-noise for equatorial scans.

- The drift scan technique also opens another avenue for the extraction and subtraction of foregrounds: the EoR signal is statistically homogeneous while the foregrounds

might not share this property. We investigate the potential of this possibility using a set of bright point sources (figure 4.10).

Our results suggest that drift scans might provide a viable, and potentially superior, method for extracting the EoR signal. In this chapter, we present mainly analytic results to make our case. In the future, we hope to return to this issue with numerical simulations and direct application of our method to the MWA data.

Chapter 5

Summary and Conclusions

The detection of the redshifted HI from the Epoch of Reionization is an outstanding aim of modern observational Cosmology. Although low frequency radio interferometers provide a window to measure HI power spectrum, the apparent straightforward methods are restricted due to various issues. First, the predicted signal is extremely weak (~ 10 mK) in the presence of strong foregrounds (Synchrotron emission from our galaxy, extragalactic radio sources) which are 3 to 4 orders of magnitude higher than the expected signal. Second, to reduce the thermal noise and reach the required sensitivity, data of very long duration is needed to be carefully analysed. This requires a stable instrument with preferably constant system parameters.

Statistical detection of the HI signal has been a major science goal for present day and upcoming radio interferometers like MWA, LOFAR, PAPER, HERA, GMRT, SKA. With all these worldwide efforts going on, it is extremely important to work on various methodologies to extract the HI power spectrum from observational data and study possible ways to minimize the foreground effects. In this thesis work we have primarily investigated two methods, one is based on the 'delay spectrum' approach for tracking observations and the other focuses on the 'Drift scan' methodology.

The use of radio interferometers to estimate the underlying power spectra has been successfully employed for CMB data analysis (Hobson et al. (1995)). This method has also been suggested as a possible probe of the intensity correlations of the redshifted HI line,

including from the EoR (Bharadwaj & Sethi (2001); Datta et al. (2007); Bharadwaj & Ali (2005)). In chapter 2, we review the relation between the radio interferometric variables and EoR observables. We show that the HI power spectrum $P_{\rm HI}(k)$ can be estimated from the correlation of observed 'visibilities' which are the primary data measurements of an interferometer. The 'visibility correlation' function (Eq. 2.10) effectively captures the fluctuation in HI signal in terms of $P_{\rm HI}(k)$. We have particularly considered an approach based on the 'delay space' technique. In Eq. 2.18 the linear relationships between the observable parameters $(\mathbf{u}_\nu, \tau)$ and Fourier space components of power spectrum are shown. Eq. 2.18 also describes the k modes which can be accessed by the interferometer, and such estimates can be obtained from the baseline distribution and frequency range of observation of the instrument. The shortest and longest baselines probe the smallest and largest value of $k_\perp$; the limits on $k_\parallel$ are obtained from the bandwidth and frequency resolution information. In 'delay space' approach, the foregrounds can be in principle separated from the HI signal owing to their fundamental difference in spectral behaviour. Foregrounds tend to have a smooth spectral characteristics, whereas the HI signal decorrelates fast with frequency. This opens up a window in Fourier space to study the HI power spectrum as the foregrounds are isolated in a 'wedge' shaped region (Fig. 2.5). The region beyond the foreground wedge ('EoR window') can be assumed to be free from any foreground contamination, and only consisting of HI signal and thermal noise.

'Delay spectrum' approach is a special variant among the visibility based power spectrum estimators. In this approach the observed interfometric data—visibilities for each antenna pair as a function of frequency—is Fourier transformed along the frequency axis. The Fourier conjugate variable effectively captures signal delay between antenna pairs, which allows one to isolate foregrounds. In the context 3d HI power spectrum this variable can be related to cosmological distance along line of sight. This strategy has been applied for redundant drift scan observations. In chapter 3, we propose a unique method 'Delay Spectrum with Imaging Arrays (DSIA)' to construct the 'delay spectrum' for non redundant imaging arrays. In this work we have taken into account two effects of a wide beam for a tracking observation. In particular our aim is to assess how these effect alter the correlation of visibilities produced by the HI signal. The impact of w-term is discussed in section 3.1. Here we show that

the inclusion of w-term tends to reduce the signal but also increases its correlation length $|u - u'|$. The former effect dominates in our case. We also present several analytic results, using our approach, which are known in the literature, e.g the primary beam scales as $1/\sqrt{w}$ for large w. We also take into account another wide field effect: the distortion of intensity pattern in a tracking run. This effect is known in the literature and can be illustrated with point sources (e.g. Perley 1999, chapter 19). During a tracking run point sources change their position with respect to the phase center and the sources further away form the phase center move faster. Their nonuniform stretching distorts the intensity pattern. In this work, we construct a coordinate system which is time dependent and it allows us to compute the correlation of visibilities produced by the HI signal at two different times. These wide field effects are used to weigh the measured visibilities as the HI signal normalization is defined for $w = 0$, and $t = t'$ (equal time correlation) (Eq. 2.19). The corresponding weights are defined in Eq. 3.13 for non-zero w and $t \neq t'$. The aim of applying these weights is to link the measured visibilities correlations with the 3D HI power spectrum.

We apply this method to 3-hours of tracking observations with MWA from EoR1 field. We present both 2d $(k_\perp, k_\parallel)$ and 1d (k) power spectrum from this analysis. This is the first demonstration in literature on how the 'delay spectrum' approach can be implemented for imaging arrays. The power spectra for both XX and YY polarizations are shown for calibrated and residual visibilities in Figures 3.8 and 3.9. Our analysis clearly demonstrates the isolation of the foregrounds in a wedge shaped region and the existence of the 'EoR window'. MWA has low angular resolution, so foreground isolation is particularly useful for MWA like instruments. We also observe improvement of sensitivity in the 'EoR window' with increasing duration of data. Maximum foreground contamination occurs for low $k_\parallel$ values. $k_\parallel = 0$ is the most foreground affected mode, power level of this mode being $10^{14} - 10^{15}\mathrm{mk}^2(\mathrm{Mpc/h})^3$. The outcomes of the method are in good match with other power spectrum pipelines within MWA EoR collaboration. We also compare our results with a full foreground + thermal noise only simulation in Fig. 3.11. Jacobs et al. (2016) have done a detailed comparison between other pipelines and find that the 1d power spectra vary by up to an order of magnitude depending on the pipeline. Our results–the power spectrum magnitude in the foreground wedge and EoR window and the 1d power spectrum–are within

this range.

As noted above the HI signal from EoR is extremely weak with added complications of strong foregrounds. This means the statistical detection would require careful analysis of long stretches of ($\sim$ hundreds of hours) data with modern radio interferometers. This requires great instrument stability with large volume data to reduce the thermal noise, in addition to the complexity of measuring and subtracting the foregrounds. The standard technique of tracking a region on sky requires constant change in the pointing center and primary beam. This might not be favourable for any EoR experiments. An alternative method is 'drift scan' where the pointing center is fixed to a particular point on the sky (preferably zenith) and observation is carried out with variable sky pattern. The main advantage of this method is the invariant shape of primary beam. We have investigated the prospects of Drift scan strategy as a viable approach for EoR experiments. We show that drift scan introduces a new dimension to the problem as the visibilities might remain correlated for a considerable amount of time, which can be used as an advantage for power spectrum estimation. We calculate the 'visibility correlation' function as a function of time for HI signal. We find that the HI signal remains correlated for a long duration (upto 1 hr) depending on the pointing center of the instrument. The correlation time scale is maximum for equitorial scans. The decorrelation time scale is dependent on the choice of the phase center. For equitorial zenith drift scans, the decorrelation time scale is independent of the baseline length. For other cases the timescale also depends on the baseline vector. This strong correlation in time may be used as an additional feature while calculating the power spectrum. We have computed the error on 'visibility correlation' function for drift scans and compared with the expected noise of tracking case, which suggest that detection of HI may be possible with $\sim$ 900 hours of observation using MWA in Drift scan mode with comparable or better sensitivity than the tracking case with added advantage of stability of the system. Drift scan also provides possible extraction and subtraction strategy of foregrounds as HI signal is statistically homogeneous and foregrounds do not share this property.

Based on our efforts, there are multiple possible future avenues of research that can be pursued to detect the cosmological 21cm signal with modern and upcoming radio interfer-

ometers (MWA, LOFAR, HERA, SKA). We now discuss possible extensions of this thesis work and future plans related to this research.

Continuation of 'delay spectrum' methodology: We have successfully developed the 'delay spectrum' methodology for tracking interferometric observation and applied it on 3 hrs of MWA data in this thesis work. However, theoretical predictions suggest the detection of EoR might be possible with hundreds of hours of observation with present day radio interferometers. This project can be carried out as continuation of 'delay spectrum' estimation from longer tracking observation. Based on the existing attempts and as a continuation of this work we would analyse larger datasets with this methodology. We would like to begin with analyzing 50 hours of data from MWA. This would involve working on building more sophisticated algorithms and pipelines as analysing large datasets comes with the cost of increasing computing power. Being generic, our method can be applied to data from other interferometers like LOFAR, PAPER data, etc. In the near future we also plan to analyse identical datasets for more apt comparison with other power spectrum pipelines in literature.

Drift scan pipeline: As mentioned earlier, the challenging part in EoR study is the detectability. The traditional method of tracking a region on the sky results in a changing primary beam along with changing system parameters in the process of tracking. This could lead to many artrifacts in the resulting power spectra. An alternate method of observation is the drift scan. The most distinct advantage of this technique is the stability of the system. We have shown (Paul & Sethi et al. (2014)) that drift scans might provide a viable, and potentially superior, method for extracting the EoR signal. As a continuation of this effort we are currently working on building a pipeline to analyse the 'Drift scan' data for widefield instruments like MWA. The pipeline developed for the drift scan will be applied first to simulated observation including various components like bright point sources, diffuse sources, thermal noise and model EoR signal. This will be extended by applying it to real observations by MWA. The cross comparison between simulations and real observation will provide greater insight into the problem and will allow us to infer the prospects of the drift scan for the present and future EoR experiments.

Beyond Power spectrum, Three point correlation / Bispectrum studies: The ob-

served large scale structure today is believed to have originated from primordial density fluctuations which were initially Gaussian. In the process of gravitational instability to form objects, early star formation and the formation and expansion of the HII bubbles, various non-Gaussian effects are expected to arise (Furlanetto et al. (2006)). In this thesis, we have only focussed on power spectrum or two-point correlation studies. For CMB studies the power spectrum depicts an excellent description of statistical properties of the Universe as the related conditions were highly Gaussian. However given the nature of the reionization process, the HI signal from EoR is expected to be non-Gaussian in nature. The Gaussian approximation holds only for scales where $P_{\rm HI} \propto P_{\delta\delta}$ (Cooray (2005)). The evolution of the HI signal developes skewness as a function of redshift (Harker et al. (2009)). The lowest order statistics for the quantification of these non-gaussian features is three point correlation function, and its Fourier transform, the bispectrum. The three point correlation can provide important information on the evolution of large scale structure. These studies so far are restricted to low redshift case (z<1) as they are based on galaxy surveys which are limited to low redshifts only. It may be possible to measure the three point correlation function during reionization epoch from radio interferometric observations. The bispectrum or the non-gaussianity is parametrized by a dimensionless parameter $f_{\rm NL}$. Recent CMB anisotropy bispectrum measurements put very stringent constraints on primordial non-Gaussianity: $f_{\rm NL} = 2.7 \pm 5.8$ (P. A. R. Ade et al. (2013)). The HI signal from the EoR can in principle also put further constraints on this parameter.

The 21 cm Cosmology holds highly promising prospects in modern observational Cosmology. In past few years enormous efforts have been put towards detection of HI from the reionization epoch, both on instrumental and data analysis fronts. This endeavour is similar to CMB research in many ways except the bigger observational challenges at lower radio frequencies. Presently operational interferometers like MWA, LOFAR, PAPER are expected to detect the statistical fluctuation of HI with hundreds hours of observation. Among the upcoming instruments HERA is a second generation radio interferometer which combines the expertise and lessons learned from MWA and PAPER. The primary science goal of HERA is statistical detection of HI signal and it has the ability to image large scale structures during

and post reionization. It is expected to be operational in next few years. In the next decade the SKA would be operational, which is expected to give a huge leap in sensitivity; SKA also has the ability of imaging during reionization. The EoR research is likely to remain an important frontier of cosmology in the near future. The richness of information that is likely to emerge from this venture on the evolution of the Universe makes this apparent long journey a worthwhile endeavour.

List of Publications

- *"Delay spectrum with Imaging Arrays: Extracting the HI power spectrum from the Epoch of Reionization"*: **Paul, Sourabh**; Sethi, Shiv K.; Morales, Miguel F.; Dwarakanath, K. S.; Subrahmanyan, Ravi; Udaya Shankar, N.; Bernardi, Gianni; Bowman, Judd D.; Briggs, Frank; Cappallo, Roger J.;Corey, Brian E.; Emrich, David; Gaensler, Bryan M.; Goeke, Robert F.; Greenhill, Lincoln J.; Hazelton, Bryna J.; Hewitt, Jacqueline N.; Johnston-Hollitt, Melanie; Kaplan, David L.; Kasper, Justin C.;Kratzenberg, Eric; Lonsdale, Colin J.; Lynch, Mervyn J.; McWhirter, S. Russell; Mitchell, Daniel A.; Morgan, Edward H.; Oberoi, Divya; Ord, Stephen M.; Prabu, Thiagaraj; Rogers, Alan E. E.; Roshi, Anish A.; Srivani, K. S.; Tingay, Steven J.; Wayth, Randall B.; Waterson, Mark; Webster, Rachel L.; Whitney, Alan R.; Williams, Andrew J.; Williams, Christopher L., 2016, submitted in ApJ.

- *"Study of the Redshifted HI from the Epoch of Reionization with Drift scan"*: **Paul, Sourabh**; Sethi, Shiv K.; Subrahmanyan, Ravi; Udaya Shankar, N.; Dwarakanath, K. S.; Deshpande, Avinash A.; Bernardi, Gianni; Bowman, Judd D.; Briggs, Frank; Cappallo, Roger J.;Corey, Brian E.; Emrich, David; Gaensler, Bryan M.; Goeke, Robert F.; Greenhill, Lincoln J.; Hazelton, Bryna J.; Hewitt, Jacqueline N.; Johnston-Hollitt, Melanie; Kaplan, David L.; Kasper, Justin C.;Kratzenberg, Eric; Lonsdale, Colin J.; Lynch, Mervyn J.; McWhirter, S. Russell; Mitchell, Daniel A.; Morales, Miguel F.; Morgan, Edward H.; Oberoi, Divya; Ord, Stephen M.; Prabu, Thiagaraj;Rogers, Alan E. E.; Roshi, Anish A.; Srivani, K. S.; Tingay, Steven J.; Wayth, Randall B.; Waterson, Mark; Webster, Rachel L.; Whitney, Alan R.; Williams, Andrew J.; Williams, Christopher L., 2014, ApJ, 793, 28.

Other Collaborative Publications

- *"The Murchison Widefield Array 21 cm Power Spectrum Analysis Methodology"*: Jacobs, Daniel C.; Hazelton, B. J.; Trott, C. M.; Dillon, Joshua S.; Pindor, B.; Sullivan, I. S.; Pober, J. C.; Barry, N.; Beardsley, A. P.; Bernardi, G.; Bowman, Judd D.;

Briggs, F.; Cappallo, R. J.; Carroll, P.;Corey, B. E.; de Oliveira-Costa, A.; Emrich, D.; Ewall-Wice, A.; Feng, L.; Gaensler, B. M.; Goeke, R.; Greenhill, L. J.; Hewitt, J. N.; Hurley-Walker, N.; Johnston-Hollitt, M.; Kaplan, D. L.; Kasper, J. C.;Kim, H. S.; Kratzenberg, E.; Lenc, E.; Line, J.; Loeb, A.; Lonsdale, C. J.; Lynch, M. J.; McKinley, B.; McWhirter, S. R.; Mitchell, D. A.; Morales, M. F.; Morgan, E.; Neben, A. R.; Thyagarajan, N.;Oberoi, D.; Offringa, A. R.; Ord, S. M.; **Paul, S.**; Prabu, T.; Procopio, P.; Riding, J.; Rogers, A. E. E.; Roshi, A.; Udaya Shankar, N.; Sethi, Shiv K.; Srivani, K. S.; Subrahmanyan, R.; Tegmark, M.;Tingay, S. J.; Waterson, M.; Wayth, R. B.; Webster, R. L.; Whitney, A. R.; Williams, A.; Williams, C. L.; Wu, C.; Wyithe, J. S. B., 2016, Accepted for publication in ApJ.

- *"The Importance of Wide-field Foreground Removal for 21 cm Cosmology: A Demonstration With Early MWA Epoch of Reionization Observations"*: Pober, J. C.; Hazelton, B. J.; Beardsley, A. P.; Barry, N. A.; Martinot, Z. E.; Sullivan, I. S.; Morales, M. F.; Bell, M. E.; Bernardi, G.; Bhat, N. D. R.; Bowman, J. D.; Briggs, F.; Cappallo, R. J.; Carroll, P.;Corey, B. E.; de Oliveira-Costa, A.; Deshpande, A. A.; Dillon, Joshua. S.; Emrich, D.; Ewall-Wice, A. M.; Feng, L.; Goeke, R.; Greenhill, L. J.; Hewitt, J. N.; Hindson, L.; Hurley-Walker, N.;Jacobs, D. C.; Johnston-Hollitt, M.; Kaplan, D. L.; Kasper, J. C.; Kim, Han-Seek; Kittiwisit, P.; Kratzenberg, E.; Kudryavtseva, N.; Lenc, E.; Line, J.; Loeb, A.; Lonsdale, C. J.; Lynch, M. J.; McKinley, B.;McWhirter, S. R.; Mitchell, D. A.; Morgan, E.; Neben, A. R.; Oberoi, D.; Offringa, A. R.; Ord, S. M.; **Paul, Sourabh**; Pindor, B.; Prabu, T.; Procopio, P.; Riding, J.; Rogers, A. E. E.; Roshi, A.;Sethi, Shiv K.; Udaya Shankar, N.; Srivani, K. S.; Subrahmanyan, R.; Tegmark, M.; Thyagarajan, Nithyanandan; Tingay, S. J.; Trott, C. M.; Waterson, M.; Wayth, R. B.; Webster, R. L.; Whitney, A. R.;Williams, A.; Williams, C. L.; Wyithe, J. S. B.,2016, ApJ, 819, 8.

- *"CHIPS: The Cosmological HI Power Spectrum Estimator"*: Trott, C. M.; Pindor, B.; Procopio, P.; Wayth, R. B.; Mitchell, D. A.; McKinley, B.; Tingay, S. J.; Barry, N.; Beardsley, A. P.; Bernardi, G.; Bowman, Judd D.; Briggs, F.; Cappallo, R. J.; Carroll, P.;de Oliveira-Costa, A.; Dillon, Joshua S.; Ewall-Wice, A.; Feng, L.; Greenhill, L. J.;

Hazelton, B. J.; Hewitt, J. N.; Hurley-Walker, N.; Johnston-Hollitt, M.; Jacobs, Daniel C.; Kaplan, D. L.; Kim, H. S.;Lenc, E.; Line, J.; Loeb, A.; Lonsdale, C. J.; Morales, M. F.; Morgan, E.; Neben, A. R.; Thyagarajan, Nithyanandan; Oberoi, D.; Offringa, A. R.; Ord, S. M.; **Paul, S.**; Pober, J. C.; Prabu, T.; Riding, J.; Udaya Shankar, N.; Sethi, Shiv K.; Srivani, K. S.; Subrahmanyan, R.; Sullivan, I. S.; Tegmark, M.; Webster, R. L.; Williams, A.; Williams, C. L.; Wu, C.; Wyithe, J. S. B., 2016, ApJ, 818, 139.

- *"Parametrising Epoch of Reionization foregrounds: A deep survey of low-frequency point-source spectra with the MWA"*: Offringa, A. R.; Trott, C. M.; Hurley-Walker, N.; Johnston-Hollitt, M.; McKinley, B.; Barry, N.; Beardsley, A. P.; Bowman, J. D.; Briggs, F.; Carroll, P.; Dillon, J. S.; Ewall-Wice, A.; Feng, L.;Gaensler, B. M.; Greenhill, L. J.; Hazelton, B. J.; Hewitt, J. N.; Jacobs, D. C.; Kim, H.-S.; Kittiwisit, P.; Lenc, E.; Line, J.; Loeb, A.; Mitchell, D. A.; Morales, M. F.; Neben, A. R.; **Paul, S.**; Pindor, B.;Pober, J. C.; Procopio, P.; Riding, J.; Sethi, S. K.; Shankar, N. U.; Subrahmanyan, R.; Sullivan, I. S.; Tegmark, M.; Thyagarajan, N.; Tingay, S. J.; Wayth, R. B.; Webster, R. L.; Wyithe, J. S. B., 2016, MNRAS, 458, 1057.

- *"Confirmation of Wide-Field Signatures in Redshifted 21 cm Power Spectra"*: Thyagarajan, Nithyanandan; Jacobs, Daniel C.; Bowman, Judd D.; Barry, N.; Beardsley, A. P.; Bernardi, G.; Briggs, F.; Cappallo, R. J.; Carroll, P.; Deshpande, A. A.; de Oliveira-Costa, A.;Dillon, Joshua S.; Ewall-Wice, A.; Feng, L.; Greenhill, L. J.; Hazelton, B. J.; Hernquist, L.; Hewitt, J. N.; Hurley-Walker, N.; Johnston-Hollitt, M.; Kaplan, D. L.; Kim, Han-Seek; Kittiwisit, P.; Lenc, E.;Line, J.; Loeb, A.; Lonsdale, C. J.; McKinley, B.; McWhirter, S. R.; Mitchell, D. A.; Morales, M. F.; Morgan, E.; Neben, A. R.; Oberoi, D.; Offringa, A. R.; Ord, S. M.; **Paul, Sourabh**; Pindor, B.; Pober, J. C.; Prabu, T.; Procopio, P.; Riding, J.; Udaya Shankar, N.; Sethi, Shiv K.; Srivani, K. S.; Subrahmanyan, R.; Sullivan, I. S.; Tegmark, M.; Tingay, S. J.; Trott, C. M.; Wayth, R. B.; Webster, R. L.;Williams, A.; Williams, C. L.; Wyithe, J. S. B., 2015, ApJL, 807, 2, L28.

- *"Empirical covariance modelling for 21 cm power spectrum estimation: A method*

demonstration and new limits from early Murchison Widefield Array 128-tile data": Dillon, Joshua S.; Neben, Abraham R.; Hewitt, Jacqueline N.; Tegmark, Max; Barry, N.; Beardsley, A. P.; Bowman, J. D.; Briggs, F.; Carroll, P.; de Oliveira-Costa, A.; Ewall-Wice, A.; Feng, L.; Greenhill, L. J.; Hazelton, B. J.; Hernquist, L.; Hurley-Walker, N.; Jacobs, D. C.; Kim, H. S.; Kittiwisit, P.; Lenc, E.; Line, J.; Loeb, A.; McKinley, B.; Mitchell, D. A.; Morales, M. F.; Offringa, A. R.; **Paul, S.**; Pindor, B.; Pober, J. C.; Procopio, P.; Riding, J.; Sethi, S.; Shankar, N. Udaya; Subrahmanyan, R.; Sullivan, I.; Thyagarajan, Nithyanandan; Tingay, S. J.; Trott, C.; Wayth, R. B.; Webster, R. L.;Wyithe, S.; Bernardi, G.; Cappallo, R. J.; Deshpande, A. A.; Johnston-Hollitt, M.; Kaplan, D. L.; Lonsdale, C. J.; McWhirter, S. R.; Morgan, E.; Oberoi, D.; Ord, S. M.; Prabu, T.; Srivani, K. S.;Williams, A.; Williams, C. L., 2015, Physical Review D, 91,12.

- *"Foregrounds in Wide-field Redshifted 21 cm Power Spectra"*: Thyagarajan, Nithyanandan; Jacobs, Daniel C.; Bowman, Judd D.; Barry, N.; Beardsley, A. P.; Bernardi, G.; Briggs, F.; Cappallo, R. J.; Carroll, P.; Corey, B. E.; de Oliveira-Costa, A.; Dillon, Joshua S.;Emrich, D.; Ewall-Wice, A.; Feng, L.; Goeke, R.; Greenhill, L. J.; Hazelton, B. J.; Hewitt, J. N.; Hurley-Walker, N.; Johnston-Hollitt, M.; Kaplan, D. L.; Kasper, J. C.; Kim, Han-Seek; Kittiwisit, P.;Kratzenberg, E.; Lenc, E.; Line, J.; Loeb, A.; Lonsdale, C. J.; Lynch, M. J.; McKinley, B.; McWhirter, S. R.; Mitchell, D. A.; Morales, M. F.; Morgan, E.; Neben, A. R.; Oberoi, D.; Offringa, A. R.;Ord, S. M.; **Paul, Sourabh**; Pindor, B.; Pober, J. C.; Prabu, T.; Procopio, P.; Riding, J.; Rogers, A. E. E.; Roshi, A.; Udaya Shankar, N.; Sethi, Shiv K.; Srivani, K. S.; Subrahmanyan, R.; Sullivan, I. S.;Tegmark, M.; Tingay, S. J.; Trott, C. M.; Waterson, M.; Wayth, R. B.; Webster, R. L.; Whitney, A. R.; Williams, A.; Williams, C. L.; Wu, C.; Wyithe, J. S. B., 2015, ApJ, 804, 14.

- *"First Limits on the 21 cm Power Spectrum during the Epoch of X-ray heating"*: Ewall-Wice, A.; Dillon, Joshua S.; Hewitt, J. N.; Loeb, A.; Mesinger, A.; Neben, A. R.; Offringa, A. R.; Tegmark, M.; Barry, N.; Beardsley, A. P.; Bernardi, G.; Bowman, Judd D.; Briggs, F.;Cappallo, R. J.; Carroll, P.; Corey, B. E.; de Oliveira-Costa, A.; Emrich,

D.; Feng, L.; Gaensler, B. M.; Goeke, R.; Greenhill, L. J.; Hazelton, B. J.; Hurley-Walker, N.; Johnston-Hollitt, M.;Jacobs, Daniel C.; Kaplan, D. L.; Kasper, J. C.; Kim, HS; Kratzenberg, E.; Lenc, E.; Line, J.; Lonsdale, C. J.; Lynch, M. J.; McKinley, B.; McWhirter, S. R.; Mitchell, D. A.; Morales, M. F.; Morgan, E.;Thyagarajan, Nithyanandan; Oberoi, D.; Ord, S. M.; **Paul, S.**; Pindor, B.; Pober, J. C.; Prabu, T.; Procopio, P.; Riding, J.; Rogers, A. E. E.; Roshi, A.; Shankar, N. Udaya; Sethi, Shiv K.; Srivani, K. S.;Subrahmanyan, R.; Sullivan, I. S.; Tingay, S. J.; Trott, C. M.; Waterson, M.; Wayth, R. B.; Webster, R. L.; Whitney, A. R.; Williams, A.; Williams, C. L.; Wu, C.; Wyithe, J. S. B., 2016, MNRAS, 877E.

- *"The Low-Frequency Environment of the Murchison Widefield Array: Radio-Frequency Interference Analysis and Mitigation"*: Offringa, A. R.; Wayth, R. B.; Hurley-Walker, N.; Kaplan, D. L.; Barry, N.; Beardsley, A. P.; Bell, M. E.; Bernardi, G.; Bowman, J. D.; Briggs, F.; Callingham, J. R.; Cappallo, R. J.; Carroll, P.;Deshpande, A. A.; Dillon, J. S.; Dwarakanath, K. S.; Ewall-Wice, A.; Feng, L.; For, B.-Q.; Gaensler, B. M.; Greenhill, L. J.; Hancock, P.; Hazelton, B. J.; Hewitt, J. N.; Hindson, L.; Jacobs, D. C.;Johnston-Hollitt, M.; Kapinska, A. D.; Kim, H.-S.; Kittiwisit, P.; Lenc, E.; Line, J.; Loeb, A.; Lonsdale, C. J.; McKinley, B.; McWhirter, S. R.; Mitchell, D. A.; Morales, M. F.; Morgan, E.; Morgan, J.; Neben, A. R.; Oberoi, D.; Ord, S. M.; **Paul, S.**; Pindor, B.; Pober, J. C.; Prabu, T.; Procopio, P.; Riding, J.; Udaya Shankar, N.; Sethi, S.; Srivani, K. S.; Staveley-Smith, L.; Subrahmanyan, R.;Sullivan, I. S.; Tegmark, M.; Thyagarajan, N.; Tingay, S. J.; Trott, C. M.; Webster, R. L.; Williams, A.; Williams, C. L.; Wu, C.; Wyithe, J. S.; Zheng, Q., 2015, PASA, 32, 13.

Bibliography

Adshead P., Furlanetto S., 2008, MNRAS, 384, 291

Ali, S. S., Bharadwaj, S., & Chengalur, J. N. 2008, MNRAS, 385, 2166

Ali, Z. S. et al., 2015, ApJ, 809, 61

Alvarez M. A., Komatsu E., Dore O., Shapiro P. R., 2006, ApJ, 647, 840

Barkana R. & Loeb A., 2001, Phys.Rep., 349, 125-238

Barkana R. & Loeb A, 2005, ApJ, 624, L65

Beardsley et al., 2013, MNRAS, 429, L5-L9

Becker, R. H., Fan, X., et al. 2001, AJ, 122, 2850

Bharadwaj S., Ali S. S., 2005, MNRAS, 356, 1519

Bharadwaj, S., Sethi, S. K., 2001, JApA, 22, 293-307

Bond, J. R. & Efstathiou, G., 1984, ApJL, 285, L45

Bowman, J. D., Morales, M. F., & Hewitt, J. N., Astrophysical Journal, Volume 638, Issue 1, pp. 20-26, 2006

Bowman, J. D. and Morales, M. F. and Hewitt, J. N., 2009, ApJ, 695, 183-199

Bowman, J. D., Cairns, I., Kaplan, D. L., et al. 2013, PASA, 30, 31

Bowman, J. D., Rogers, A. E. E., Hewitt, J. N., 2008, ApJ 676, 1âĂŞ9

Bromm, V., & Larson. R. B., 2004, ARA&A, 42, 79?118

Bromm V., Coppi P. S. & Larson R. B., 2002, ApJ, 564, 23

Chapman, E., et al. 2012, MNRAS, 423, 2518

Chapman, E., et al. 2013, MNRAS, 429, 165

Chippendale, A. P., Subrahmanyan, R. D., Ekers, R. D., 2005.,Effects of interference on the atnf cosmolgical reionization experiment at mileura. In: Proceedings of the XXIXth General Assembly of the International Union of Radio Science, Delhi, 23-29 October 2005.

Choudhury T. R. & Ferrara A., 2006, Physics of Cosmic Reionization. ArXiv Astrophysics eprints

Christiansen, W. N., Hogbom, J. A., Radiotelescopes (Cambridge University Press), 1969

Ciardi B. & Madau P., 2003, ApJ, 596, 1

Ciardi B. & Ferrara A., 2005, Space Science Reviews, 116, 625

Cooray A., 2005, MNRAS, 363, 1049?1056.

Cornwell, T. J., Golap, K., & Bhatnagar, S. 2008, IEEE Journal of Selected Topics in Signal Processing, 2, 647

Dalton et al., 1997, MNRAS, 289, 263

Datta, A., Bowman, J. D., & Carilli, C. L. 2010, ApJ, 724, 526

Datta K. K., Roy Choudhury T., Bharadwaj S., 2007, MNRAS, 378, 119

DeBoer, D. R. et al., 2016, arxiv: 1606.07473

Dillon, J., Liu, A., & Tegmark, M. 2013, Phys. Rev. D, 87, 43005

Dillon, J. S., Liu, A., Williams, C. L., et al. 2014, Phys. Rev. D, 89, 023002

Dillon, J. S. et al. 2015, Phys. Rev. D, 91, 123011

D.J. Fixsen, et al.,1996, ApJ, 473, 576

D. N. Spergel, et al., 2007, ApJS 170 377

Haslam, C. G. T., Stoffel, H., Salter, C. J., & Wilson, W. E. 1982, A&AS, 47, 1

Hu, W. & White, M., 1997, New Astronomy, 2, 323

Fan, X., Carilli, C.L., & Keating, B., 2006, ARA&A, 44, 415

Fan, X., Carilli, C.L., & Keating, B., 2006, ARA&A, 44, 415

Fan et al., 2006, ApJ, 132, 117

Field, G. B., 1958, Proc. IRE, 46, 240

Field G. B., 1959, ApJ, 129, 536

F. R. Schwab., 1984, AJ, 89:1076âĂŞ1081

Furlanetto, S. R., Oh, S. P., & Briggs, F. H. 2006, Phys.Rep., 433, 181-301

Furlanetto, S. R. & Lidz, A., 2007, ApJ, 660, 1030

Furlanetto, S. R., 2016, Understanding the Epoch of Cosmic Reionization: Challenges and Progress, 423, arxiv:1511.01131

G. B. Rybicki and A. P. Lightman. Radiative Processes in Astrophysics. June 1986.

Greenhill, L. J. & Bernardi, G., HI Epoch of Reionization Arrays in 11th Asian-Pacific Regional IAU Meeting 2011, NARIT Conference Series, 1, eds. S. Komonjinda, Y. Kovalev, and D. Ruffolo, (Bangkok, NARIT 2012)

Gunn & Peterson, 1965, ApJ, 142, 1633

Haiman, Z., & Knox, L. 1999, in ASP Conf. Ser. 181, Microwave Foregrounds, ed.

Harker, G. et al. 2009, MNRAS, 397, 1138

Haslam, C. G. T., Stoffel, H., Salter, C. J., & Wilson, W. E. 1982, A&AS, 47, 1

Hazelton, B. J., Morales, M. F., Sullivan, I. S., 2013, ApJ, 770, 156

Hazelton, B. J., et al. 2016, in prep

H. Mo, F. C. van den Bosch & S. White. Galaxy Formation and Evolution. 2010.

Hobson M. P., Lasenby A. N., Jones M., 1995, MNRAS, 275, 863

Hopkins, A. M., Afonso, J., Chan, B., et al. 2003, AJ, 125, 465

Jacobs, D. C., et al. 2016, submitted in ApJ

Jelic, V. et al., 2008, MNRAS, 389, 1319

J. R. Pritchard and A. Loeb, PRD, 82, 023006 (2010), arXiv:1005.4057

Kaiser N., 1987, MNRAS, 227, 1

Komatsu, E., et al. 2010, arxiv:1001.4538

Lamarre et al., 2003 New Astron Rev 47, 1017

Liu, A., Pritchard, J. R., Tegmark, M. and Loeb, A., 2013, Phys. Rev. D, 87, 043002

Liu, Adrian., Parsons, Aaron R., Trott, Cathryn M., 2014, Phys. Rev. D, 90, 023018

Liu, A. & Tegmark, M., 2011, Phys. Rev. D, 83, 103006

L. Page, G. Hinshaw, E. Komatsu, M. R. Nolta, D. N. Spergel, C. L. Bennett, C. Barnes, R. Bean, O. DorÂť e, J. Dunkley, M. Halpern, R. S. Hill, N. Jarosik, A. Kogut, M. Limon, S. S. Meyer, N. Odegard, H. V. Peiris, G. S. Tucker, L. Verde, J. L. Weiland, E. Wollack, and E. L. Wright. Three-Year Wilkinson Microwave Anisotropy Probe (WMAP) Observations: Polarization Analysis. ApJS, 170:335âĂŞ376, June 2007.

Lonsdale, C. J., Cappallo, R. J., Morales, M. F., et al. 2009, IEEE Proceedings, 97, 1497

Madau P., Meiksin A. & Rees M. J., 1997, ApJ, 475, 429

Mather et al. 1990, ApJ, 354, L37

Mao Y. et al., 2012, MNRAS, 422, 926

McMullin, J. P., Waters, B., Schiebel, D., Young, W., & Golap, K. 2007, Astronomical Data Analysis Software and Systems XVI (ASP Conf. Ser. 376), ed. R. A. Shaw, F. Hill, & D. J. Bell (San Francisco, CA: ASP), 127

McQuinn, M., Zahn, O., Zaldarriaga, M., Hernquist, L., & Furlanetto, S. R., 2006, ApJ, 653, 815

Mitchell, D. A., Greenhill, L. J., Wayth, R. B., Sault, R. J., Lonsdale, C. J., Cappallo, R. J., Morales, M. F., & Ord, S. M., 2008, IEEE Journal of Selected Topics in Signal Processing, 2, 707

Morales, M. F. & Hewitt, J. 2004, ApJ, 615,7

Morales, M. F., 2005, ApJ, 619, 678

Morales, M. F., & Wyithe, J. S. B. 2010, ARA&A, 48, 127

Morales, M. F., Hazelton, B., Sullivan, I., & Beardsley, A. 2012, ApJ, 752, 137

Nuttall, A. H., 1981, IEEE Transactions on Acoustics Speech and Signal Processing, 29, 84

Offringa, A. R. et al, 2015, PASA, 32, 8

Ord, S. M. et al. 2010, Publications of the Astronomical Society of the Pacific, 122, 1353

P. A. R. Ade et al. (Planck Collaboration), arXiv:1303.5084.

Paciga, G., et al. 2013, MNRAS, 433, 639

Parsons, A., Pober, J. et al., 2012a, ApJ, 753, 81

Parsons, A. R., Pober, J. C. et al., 2012, ApJ, 756, 165p

Parsons, A. R., et al. 2014, ApJ, 788, 106

Patra, N. et al., 2015, ApJ, 801, 138

Paul, S., Sethi, S. K. et al., 2014, ApJ, 793, 28

P. J. E. Peebles. Principles of Physical Cosmology. 1993

Peebles, P. J. E. & Yu, J. T., 1970, ApJ, 162, 815

Pen, U. L., Chang, T. C., Hirata, C. M., Peterson, J. B., Roy, J., Gupta, Y., Odegova, J., Sigurdson, K., 2009, MNRAS, 399, 181

Penzias, A. A., Wilson, R. W., ApJ, 1965, 142, 419

Perlmutter, S. et al., 1999, ApJ, 517, 565

Planck Collaboration and Ade, P. A. R. and Aghanim, N. and Arnaud, M. and Ashdown, M. and Aumont, J. and Baccigalupi, C. and Banday, A. J. and Barreiro, R. B. and Bartlett, J. G. and et al., 2015, arXiv:1502.01589

Planck Collaboration and Ade, R. and Aghanim, N. et al., 2016, arXiv:1605.03507v2

Planck Collaboration and Ade, P. A. R. and Aghanim, N. et al. 2013, Planck 2013 Results. XVI. Cosmological Parameters, arXiv:1303.5076

Pober, J. C., Parsons, A. R. et al., 2013, ApJ, 768L, 36

Presley, M.E., Liu, A., Parsons, A.R., 2015, ApJ, 809, 18

Rau, U. and Cornwell, T. J., 2011, Astronomy & Astrophysics, 532, A71

Riess, Adam G., et al, The Astronomical Journal, 1998, 116, 1009

Robertson, B. E., Ellis, R. S., Dunlop, J. S., McLure, R. J. & Stark, D. P., 2010, Nature, 468, 49-55

Santos M. J. et al, 2008, ApJ, 689, 1

Schmidt, M., 1963, Nature, 197, 1040

Sethi S. K., 2005, MNRAS, 363, 818

Shaw J. R. & Lewis A., 2008, PRD, 78(10):103512,

Singh, S., Subrahmanyan, R., Udaya Shankar, N., Raghunathan, A., 2015, ApJ, 815, 88

Smoot, G. F. et al, 1992, ApJL, 396, L1

Sullivan, I. S. et al. 2012, The Astrophysical Journal, 759, 17

Tabitha C. Voytek, Aravind Natarajan, JosÃĺ Miguel JÃąuregui GarcÃŋa, Jeffrey B. Peterson, and Omar LÃşpez-Cruz, 2014, The Astrophysical Journal Letters, 782, 1

Taylor, G. B., Carilli, C. L., & Perley, R. A. 1999, Synthesis Imaging in Radio Astronomy II, 180, Chapter 19

Thomas R. M. et al, 2009, MNRAS, 393, 32

Thomas L. Wilson, Kristen Rohlfs, Susanne Huttemeister, Tools of Radio Astronomy, Fifth Edition, 2009, Springer

Thompson, A. R., Moran, J. M. & Swenson, G. W. Jr. 1986, Interferometry and Synthesis in Radio Astronomy (New York: Wiley)

Thyagarajan, N., Udaya Shankar, N., Subrahmanyan, R., et al., 2013, ApJ, 776, 6

Thyagarajan, N. et al., 2015a, ApJ, 804, 14

Thyagarajan, N. et al., 2015b, The Astrophysical Journal Letters, 807, L28

Thyagarajan, N., Parsons, A., DeBoer, D., et al., 2016, ArXiv e-prints, arXiv:1603.08958

Tingay, S. J. et al., 2013, PASA, 30.

T. J. Cornwell, K. Golap, and S. Bhatnagar, 2008, IEEE Journal of Selected Topics in Signal Processing, 2:647âĂŞ657

Trott, C., Wayth, R., & Tingay, S. 2012, ApJ, 757, 101

Trott CM, 2014, arxiv: 1405.0357

Trott, C. M. et al., 2016, ApJ, 818, 139

Van Haarlem, M. P. et al. Astron. Astrophys. 556, A2 (2013)

Vedantham, H., Udaya Shankar, N., & Subrahmanyan, R. 2012, ApJ, 745, 176

Wouthuysen S. A., 1952, AJ, 57, 31

York, Donald G., 2000, The astronomical Journal, 120, 1579-1587

Zaldarriaga, M., & Seljak, U. 1997, Phys. Rev. D, 55, 1830

Zaldarriaga, M., Furlanetto, S. R., & Hernquist, L., 2004, ApJ, 608, 622

Zaroubi, Saleem, 2013, Astrophysics and Space Science Library, 396, arxiv: 1206.0267

Zheng, Q., Wu, X.-P., Hollitt, M. J., Gu, J.-H., Xu, H., 2016, arXiv:1602.06624v1